

**SINGLE ATOMS
COUPLED TO A NEAR-CONCENTRIC CAVITY**

NGUYEN CHI HUAN
(B.Eng.(Hons.),NUS)

**A THESIS SUBMITTED
FOR THE DEGREE OF DOCTOR OF PHILOSOPHY
CENTRE FOR QUANTUM TECHNOLOGIES
NATIONAL UNIVERSITY OF SINGAPORE**

2018

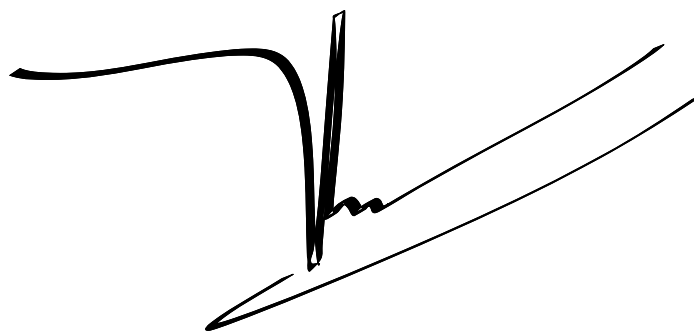
Supervisors:
Professor Christian Kurtsiefer

Examiners:
Assistant Professor Travis Nicholson, National University of Singapore
Associate Professor Jonathan Home, ETH Zurich
Professor Dieter Meschede, University of Bonn

DECLARATION

I hereby declare that this thesis is my original work and it has
been written by me in its entirety. I have duly
acknowledged all the sources of information which
have been used in the thesis.

This thesis has also not been submitted for any degree
in any university previously.

A stylized handwritten signature in black ink, featuring a prominent vertical stroke and a horizontal stroke extending to the left.

Nguyen Chi Huan

Single atoms coupled to a near-concentric cavity

by

Nguyen Chi Huan

Abstract

Strong interaction between single atoms and single photons in cavity quantum electrodynamics (cavity-QED) is well established with the use of optical resonators of high finesse and short cavity lengths. Despite their remarkable achievements to demonstrate many important proof-of-principle protocols in quantum information processing, stringent requirements of sophisticated mirror coatings can hinder scalability of such techniques for the realization of a large-scale quantum network.

In this thesis, we present an alternative approach to implement cavity-QED by coupling single rubidium atoms to an 11-mm-long near-concentric cavity which provides large electric field required for strong interaction via a strong focusing cavity mode. Operating the cavity at $1.7(1) \mu\text{m}$ shorter than the critical length, we observed a coupling strength of $g_0 = 2\pi \times 5.0(2) \text{ MHz}$, which exceeds the natural dipole decay rate by a factor of 1.9. Our approach is potential to achieve a strong coupling regime with relatively low finesse mirrors and may even help to make cavity-QED possible for atomic species like ions and Rydberg atoms, which are inherently challenging to place in cavities.

Thesis Supervisor: Christian Kurtsiefer

Title: Professor

Acknowledgments

I would first like to thank my thesis advisor Prof. Christian Kurtsiefer. Throughout the years, I have profoundly benefited by observing, learning, working, and receiving feedback and advice from him. He has provided guidance and assistance at key moments while also allowing me to work independently the majority of the time. More importantly, his unique taste for extracting the most essentials from complicate physics problems, his highest level of scientific integrity and intellectual rigor have taught me what it means to be a good physicist and a great teacher.

With a special mention to my brilliant teammates: Kadir Durak, Stanislav Straupe, Gleb Maslennikov, Nick Lewty, and Adrian Utama, with whom I have shared the pain and the joy of building up the near-concentric cavity experiment from scratch, and who are going to improve it to a new level. Without their talent and effort, there will not be the upcoming pages in this thesis.

Along the journey, I have received great help from other lab mates who have shortly participated in the project, nonetheless have contributed to many important results: Mathias Steiner, Brenda Chng, Do Thi Bich Hue, Nguyen Minh Nguyet, and Tan Ting You.

The strong sense of community and friendship in the quantum optics group has been an important part of my PhD. I would like to thank Janet Lim, Lee JianWei , Shen Lijiong, and Chow Chang Hoong for all the laughs and coffee talks.

From farther distance, the wholehearted love from my special buddy, Coco Van Nguyen, and my parents has been a great source of happiness through the entire journey.

Lists of Publications & Conferences

The main results of this thesis have been reported in the following articles:

- Durak, K., **Nguyen, C. H.**, Leong, V., Straupe, S., and Kurtsiefer, C. (2014). Diffraction-limited Fabry-Perot cavity in the near concentric regime. *New Journal of Physics*, 16(10):103002.
- **Nguyen, C. H.**, Utama, A. N., Lewty, N., Durak, K., Maslennikov, G., Straupe, S., Steiner, M., and Kurtsiefer, C. (2017). Single atoms coupled to a near-concentric cavity. *Physical Review A*, 96(3):031802.
- **Nguyen, C. H.**, Utama, A. N., Lewty, N., and Kurtsiefer, C. (2018). Operating a near-concentric cavity at the last stable resonance. arXiv:1806.03038

The results have also been presented at the following international conferences:

- **[Poster]** Strong Atom-Light Interaction in Near-Concentric Optical Resonators, EQEC 2015, Munich, Germany
- **[Talk]** Lineshape splitting with single atoms in concentric cavities, CLEO/Europe-EQEC17, Munich, Germany
- **[Poster]** Single atoms coupled to a near-concentric cavity, RQED 2017, Munich, Germany

Contents

1	Introduction	1
2	Theory	9
2.1	A spin and a spring: the Jaynes-Cummings model	9
2.2	Damped atom-cavity system	15
2.3	Coupling regimes	16
2.4	Cavity configuration and stability	18
3	Building a near-concentric cavity	23
3.1	Design of the cavity	23
3.1.1	Mirror design	24
3.1.2	Mechanical positioning of the mirrors	26
3.1.3	Cavity mount	27
3.2	Cavity construction	29
3.2.1	Assembly procedure	29
3.2.2	Alignment procedure	30
3.2.3	Post-alignment drift	33
3.3	Characterization of cavities	33
3.3.1	How near is near to concentric?	34
3.3.2	Cavity mode analysis	40
3.3.3	Cavity losses	43
3.4	Contamination of cavity mirrors	47
3.5	Upgrading the design	48

4	Taming a near-concentric cavity	51
4.1	Longitudinal stabilization	52
4.1.1	Optical setup	54
4.1.2	Locking circuit	57
4.2	Transverse stabilization	59
4.2.1	Transverse misalignment sensitivity	59
4.2.2	Transverse stabilization algorithm	59
5	Trapping single atoms in a near-concentric cavity	63
5.1	Magneto-optical traps	64
5.2	Intra-cavity dipole traps	69
5.3	Detection of single atoms	78
6	Determining the atom-cavity interaction	83
6.1	Methods of probing the atom-cavity interaction	84
6.2	Wide-range detuning of laser frequencies	86
6.2.1	Detuning by AOM	86
6.2.2	EOM sideband locking	88
6.3	Atom-light interaction setup	89
6.3.1	Optical setup	89
6.3.2	Measurement sequence	90
6.3.3	Experimental sequence of trapping and probing	93
6.4	Resonant probing	94
6.5	Normal mode splitting	96
7	Conclusion and outlook	103
7.1	Conclusion	103
7.2	Outlook	105
7.2.1	Rapid deterministic loading of single atoms	105
7.2.2	Deep optical dipole traps	106
7.2.3	Single atoms coupled to multiple cavity modes	106
7.2.4	Ion traps in near-concentric cavities	107

List of Figures

1-1	Mode volume and linewidth of optical cavities of different geometrical configurations. Near-concentric cavities minimize both the mode volume and linewidth for a given cavity finesse and mirrors' radius of curvature. Top insets show the mode profile at three important cavity regimes.	5
2-1	The Jaynes-Cummings ladder for resonant case $\Delta_{ac} = \omega_a - \omega_c = 0$. The energy level structure is a series of doublets representing normal-modes of the coupled atom-cavity system.	13
2-2	Spectroscopy of the Jaynes-Cummings ladder. Top: resonant frequencies ω_{\pm} of the uncoupled system (dash lines) and coupled system (solid lines) when the cavity frequency is fixed and the atomic frequency is tuned over the resonance. Colour indicates the relative amplitude of the atomic bare state $ e, 0\rangle$ (more red), and the cavity bare state $ g, 1\rangle$ (more blue). At $\Delta_{ac} = 0$, Bottom: cavity transmission spectra at different atom-cavity detuning of a weak probe beam such that only the first doublet is excited.	14
2-3	Coupling regimes of the atom-cavity system. Solid curves: normalized resonant frequencies; dashed curves: normalized decay rates. Colour indicates the relative amplitude of the atomic bare state $ e, 0\rangle$ (more red), and the cavity bare state $ g, 1\rangle$ (more blue). Zones (i),(ii) and (iii) correspond to the weak regime, the intermediate regime and the strong coupling regime respectively.	17
2-4	The stability diagram for two-mirror optical cavities. The grey area indicates the stable region.	20

2-5	Comparison of properties of a fundamental transverse mode for stable cavity configurations. The cavity is formed by a pair of mirrors with the radius of curvature of $R = 5$ mm and a finesse of 500. Top: beam size of the cavity mode at the mirrors (dashed line) and the cavity waist at the center (solid line). Middle: effective mode volume in the unit of λ^3 where $\lambda = 780$ nm. The mode volume is minimum at the near-planar and near-concentric regime and maximum at $l_{cav}/R = 3/2$. In the near-concentric region, the mode volume reduce more rapidly than the near-planar region. Bottom: the cavity loss (κ) inversely proportional to l_{cav}	22
3-1	Design of the near-concentric cavity mirrors. Left: Schematic drawing of the mirror. The spherical surface with HR coating at 780 nm acts as the cavity mirror. The input surface has an elliptical profile and employed as the mode-matching lens. Top right: Image of the cavity mirror in the shield. Bottom right: Image of the cavity mirror surface.	25
3-2	An overview of the near-concentric cavity mounting system.	27
3-3	Three-dimensional model of the near-concentric cavity system. (a) The completed assembly view with system dimensions in millimeters. (b) The exploded view: 1 Cavity holder. 2 Back plate. 3 Stacked piezo. 4 Front plate. 5 L-shaped block. 6 Ring piezo. 7 PEEK spacer. 8 Right cavity mirror in the shield. 9 Left cavity mirror in the shield. 10 Spherical opening. The yellow bars indicate the piezo electrodes. Arrows show the direction of assembling parts.	28
3-4	Image of an assembled near-concentric cavity.	29
3-5	Schematic of the cavity alignment setup. Two single-mode fiber couplers (FC) coupled to each other define a reference line for the optical axis of concentric cavity (CC). An auxiliary holder (AH) is placed on the left translation stage (TS1) with an external piezo system (EPS). The cavity mounting system is on the right translation stage (TS2). Rotational degrees of freedom are provided by tip-tilt mounts (TM). M: mirrors.	31

3-6	Cavity drifting after alignment. Each red dot indicates the drift of one cavity mirror with respect to the other after one attempt of cavity alignment.	33
3-7	Transverse mode frequencies in various geometrical configurations of optical cavities. The longitudinal mode spacing (or the free spectral range) is denoted as $\Delta\nu_{\text{fsr}}$. The transverse mode spacing is denoted as $\Delta\nu_{\text{tr}}$	38
3-8	Transverse mode frequency spacing at different cavity lengths that are resonant with a 780-nm laser. Solid line are theoretical fit based on Eq. 3.3.9. Error bars show the standard deviation of the measurement.	39
3-9	Cavity transmission spectra measured by detuning the cavity length. (a) $d = 597$ nm. The dashed line is the fit based on a summation of two Lorentzian functions, corresponding to two resonant peaks. (b) $d = 207$ nm. Transverse modes become degenerate and form a long tail extending out to the lower frequencies. (c) $d = -183$ nm. The cavity is in the unstable regime. The insets show the transverse mode profiles.	42
3-10	Tilting misalignment of spherical optical cavities. A tilt of one of the cavity mirrors about the optical axis (o.A.) by θ induces additional diffraction loss per round trip. The total diffraction loss is a function of stability parameter g , the mode beam waist on mirror w_m , and the radius of mirror aperture a	46
3-11	Assembly of the cavity system with the Attocube piezo scanner (AN-Sxyz100).	49
3-12	Image of an assembled cavity with the Attocube piezo scanner.	49
4-1	Schematic of the near-concentric cavity locking chain. The strategy is to have the near-concentric cavities indirectly locked to the 780-nm laser, indicated by the dashed arrow, via intermediate nodes: the 810-nm laser and the transfer cavity.	52

4-2	Optical locking scheme of transfer cavity and the 810-nm lock laser. Red and orange lines indicate beams from 780-nm laser and 810-nm lock laser, respectively. The 780-nm laser serves as the cooling laser for atom trapping. The frequency of the 780-nm laser is stabilized to a D2 transition of ^{87}Rb . The lock laser's sideband is stabilized to a resonance of the transfer cavity, which in turn is stabilized to the 780-nm laser. The frequency of the lock laser can be tuned by adjusting the sideband's frequency. All cavity locking schemes use the standard Pound-Drever-Hall technique with 20-MHz phase modulation. EOM: electro-optic phase modulator. PD: high-bandwidth photodetector. HWP: half-wave plate. QWP: quarter-wave plate. PBS: polarization beam splitter. SMF: single-mode fiber. IF: interference filter.	55
4-3	Optical locking scheme of the near-concentric cavity. Red and orange lines indicate the beams from 780 nm laser and 810 nm lock laser, respectively. The two laser beams are combined at a dichroic mirror (DM) and coupled to the fundamental modes of the cavity. The locking error signal is derived from the cavity transmission which is coupled to a single-mode fiber for the spatial mode filtering. PD: high-bandwidth photodetector. SMF: single-mode fibers. IF: interference filters. . . .	57
4-4	Schematic diagram of the electronic circuit to generate the error signal and to lock the cavity resonance using the PDH technique. A modulation signal at 20 MHz drives the EOM and operates as a local oscillator. The optical signal from the cavity reflection/transmission is amplified and demodulated at the mixer to generate the error signal. The control loop consists of Proportional-Integral feedback implemented with operational-amplifiers. The phase shifter (PS) adjusts the phase of the local oscillator (LO) to compensate for the phase offset. HV: high voltage amplifier.	58
4-5	Sensitivity of cavity transmission coupled to a single-mode fiber as a function of transverse displacements. The cavity mirror is displaced in x and y directions while the cavity length is stabilized.	60

4-6	Observation of drift of transverse cavity alignment. The cavity transmission coupled to a single-mode fiber as a function of transverse displacements is recorded at an interval of 30 minutes. The drift is directional and is attributed to the thermal expansion of the cavity structure.	60
4-7	Long-term stability of the near-concentric cavity at $d = 207$ nm. The cavity length is locked during the measurement. The slow drift of cavity transmission on the order of minutes is due to the transverse misalignment which is caused by temperature change. Vertical arrows indicate the activation of the stabilization algorithm. The cavity transmission recovers to the maximum value after the successful implementation of the algorithm.	61
5-2	Schematic experimental setup of trapping single atoms in the near-concentric cavity. A magneto-optical trap (MOT) of ^{87}Rb is prepared at the cavity focus. The two vertical MOT beams, indicated by red lines, form an angle of 20 degrees. Not shown is the horizontal cooling beam and the magnetic coils. The coil axis is orthogonal to the plane of the paper. The trap laser couples to the fundamental mode of the cavity to form an intra-cavity far-off-resonance dipole trap. Single atoms are probabilistically loaded into the trap and coupled to the cavity mode. The fluorescence light of the trapped single atoms collected into the resonant cavity mode is spectrally filtered and coupled to a single-mode fiber which is attached to an avalanche photodiode (APD).	68
5-3	Schematic of vacuum chamber for atom trapping experiments with near-concentric cavities.	69
5-4	^{87}Rb D1 and D2 transition with hyperfine levels. Shown are the transitions used for MOT cooling and MOT repump lasers.	70

5-5	(a) Energy level of atoms interacting with a red-detuned laser. The atomic energy is shifted according to the laser-intensity profile. The ground-state atoms are attracted to the maxima of the intensity, while the excited-state atoms are repelled from it. (b) Atoms from the MOT can be loaded to the dipole trap when their kinetic energy $k_B T$ is below the trap depth U_{dip}	75
5-6	Intra-cavity dipole potential of the near-concentric cavity. The cavity length is set at $1.7 \mu\text{m}$ away from the concentric point. The intra-cavity power is 11 mW. The wavelength was stretched by a factor of 100 in z direction to display individual trapping sites.	78
5-7	Typical trace of detection events during the atom loading process. The sudden increase of fluorescence indicates the entering of an atom into the dipole trap.	79
5-8	Samples of fluorescence of trapped atoms in the cavity mode. (a) The fluorescence of single atoms exhibits a clear telegraph signal characteristic. (b) Representative traces of short-lifetime atoms (blue) and two atoms (red).	81
5-9	Lifetime of single atoms in the dipole trap without cooling light for a duration τ . The solid line represents an exponential fit with a $1/e$ lifetime of 230(30) ms.	82
6-1	Modifications of the cavity field by a single atom observed via two different probing methods: (a) the cavity transmission spectrum and (b) the decay of the cavity field. In the strong coupling regime with $(g_0, \kappa, \gamma) = 2\pi \times (20, 11, 3)$ MHz (blue solid lines), evidence of the normal modes are a distinctive doublet of the spectrum and the ringing of the cavity decay. In contrast, there is lineshape splitting but no ringing for the case of $(g_0, \kappa, \gamma) = 2\pi \times (12, 50, 3)$ MHz (solid red lines). For comparison, the empty-cavity case is shown and indicated by dashed black lines.	85

6-2	Schematic drawing of a double-pass AOM setup for large detuning of laser frequencies. The optical power after the single-mode fiber is detected and compared to a set point. A control program adjusts the RF power to the AOM to minimize their difference. Lenses have a focus of 150 mm, and their positions orthogonal to the laser beam can be adjusted to compensate for the beam deflections. Red arrows indicate laser beams; black triangles indicate the flow of electronic signals. BB: beam blocks.	87
6-3	Detuning laser frequency by AOMs. The optical power of the first order diffracted beams coupled to a single mode fiber is monitored as the RF driving frequency is detuned. (a) The case of one AOM in the double-pass configuration. The deviation of the diffracted optical power is about 25% without the compensation algorithm (blue trace), and reduced to about 2% with the compensation algorithm (red trace). (b) Optical output after two double-pass AOM. A deviation of about 2% in the diffracted optical power is observed for a detuning range of ± 100 MHz.	88
6-4	Normalized cavity reflection (a) and transmission (b) spectrum. The cavity length is stabilized while the probe beam frequency is detuned using the EOM sideband locking technique. Solid lines are fits based on Lorentzian lineshapes. η is the cavity coupling efficiency, and T_{\max} is the cavity resonant transmission.	89
6-5	Optical setup. A near-resonant 780 nm probe laser couples to the cavity to characterize the light-atom interaction. The transmitted and reflected light is coupled into single-mode fibers connected to avalanche photodetectors. The cavity length is stabilized close to the concentric length. The intracavity field at 810 nm provides also a far-off-resonant standing-wave dipole trap for the atoms. BS: beam splitter with 70% reflectivity; DM: dichroic mirror; PZT: 3D-piezo actuator stack; PD: photodiode; MOT: magneto-optical trap; D1(2): avalanche photodetectors.	90

6-6	Experimental control scheme. The transverse alignment and resonance of the near-concentric cavity are verified at two stages: the resonance lock and the transverse lock. The main experiment proceeds only when both stages pass without adjustment.	92
6-7	Timing sequence of trapping and probing single atoms. After the detection of single atoms, the quadrupole magnetic field and repumping beam are switched off to disperse the MOT. This is followed by an experimental cycle that alternates between 1 ms of probing the cavity transmission, and 1 ms of laser cooling. A probe pulse with 50 ms duration is used to measure the empty-cavity transmission and reflection.	94
6-8	Effect of single atoms on cavity transmission. An experimental sequence with a duration of 200 ms consists of interleaving 1 ms pulses of cooling (red/upper) and probing (blue/bottom). Error bars represent one standard deviation determined from the measured count rates, assuming Poissonian counting statistics.	95
6-9	Average of the cavity transmission when single atoms are loaded into the cavity mode. The probe frequency is tuned to the atom-cavity resonance to observe the highest extinction of the transmission. The average of the resonant extinction ratio is determined to be 39% from a fit indicated by the solid line.	96
6-10	Onset of the normal-mode splitting in the a) reflection and b) transmission spectrum when an atom is trapped in the FORT. Red solid lines are fits based on Eq. 6.5.1a. For comparison the empty cavity reflection/transmission is shown in gray.	97
6-11	Demonstration of variation of the atom-cavity coupling strength. Single atoms are loaded into the bottom of the intracavity dipole trap formed by a 810-nm standing wave (Top). At the bottom is the corresponding atomic positions in the lattice of the resonant cavity mode at 780 nm.	99

6-12	Simulation of variation of the atom-cavity coupling strength for $N=2000$ atom loading events. (a) Atoms are randomly assigned to different trapping sites. This results in the distribution of the normalized coupling strength \bar{g}/g_0 shown in (b).	100
6-13	Cavity transmission spectra for three types of single-atoms indicated by red dots: $P_{\text{fl}} \geq 20$ counts/ms, blue squares: $17 \leq P_{\text{fl}} \leq 20$ counts/ms, black triangles: $13 \leq P_{\text{fl}} \leq 17$ counts/ms. The solid line is predicted spectrum for the effective coupling strength \bar{g} . The dash line is a theoretically predicted spectrum for the maximum coupling strength.	101
7-1	Atom-cavity coupling strength obtained in some existing experiments with Fabry-Perot optical resonators. The respective theoretical predictions for coupling strength in other experiments are represented by red dots; [1] Kimble's group [McKeever et al., 2003], [2] Chapman's group [Fortier et al., 2007], [3] Axel Kuhn's group [Barrett et al., 2018], [4] Rempe's group [Neuzner et al., 2016]. Coupling strength obtained in the near-concentric cavity presented in this thesis: [5] experimental observation, [6] theoretical prediction.	104

Chapter 1

Introduction

The last decades have heralded an exciting era in which quantum physicists start to explore the impact of quantum physics on information and computer science. A broad range of fundamental theories have been developed, from an algorithm that places existing public-key cryptography at risk to proposals to teleport quantum states to communication protocols that are inherently protected from eavesdropping [[Shor, 1995](#), [Boschi et al., 1998](#), [Ekert, 1991](#)].

These stimulating theoretical results provide motivation to explore physical processes that translate those early ideas into reality. On the experimental side, significant efforts have been made to demonstrate relatively simple protocols of quantum information processing with many different physical platforms, including ion traps [[Blatt and Wineland, 2008](#)], superconducting circuits [[Devoret and Schoelkopf, 2013](#)], spins in quantum dots [[Warburton, 2013](#)], crystalline defect centers [[Hanson et al., 2008](#)], and nuclear magnetic resonance [[Vandersypen and Chuang, 2004](#)]. However, in order to transform the early phase of experiments in laboratory environments to the stage that the power of quantum technologies can be harnessed to solve practical problems, the number of quantum bits implemented in the systems must be increased while quantum coherence is preserved. Only recently, a tremendous progress has been made to push the ion traps and superconducting circuits into a regime of quantum supremacy, where the number of operations and amount of information stored in the quantum bits (qubits) exceed what can be hardly implemented in classical counterparts. However, the information carriers in these systems are not yet in

an appropriate form to be transmitted over a long distance. In the case of superconducting circuits, longer coherence time and efficient conversion from microwave to optical photon would be required.

On the other hand, photons at visible and infrared wavelength have good transport properties and are excellent candidates for information carriers. Superposition and entanglement of photonic states can remain for indefinite times. The probability of photon-photon scattering in free-space is almost negligible. This linearity in light propagation, high frequency and hence large bandwidth together with the ease of detection and manipulation have made optical signals a preferable method to convey information faithfully over a long distance [Chang et al., 2014]. In addition, the existence of a vast network of optical fibers deployed by the telecommunication industry eases out the needs and financial investment to construct new infrastructure for quantum communication.

In contrast, information processing relies on some form of interaction between the signals. The same mechanism that protects the photons from decoherence makes them hard to interact with each other, and hence challenging to construct photonic quantum gates [Barenco et al., 1995]. The strategy of having a controllable qubit while decoupling it from the environment to avoid decoherence can be realized by a hybrid system of light and matter qubits: the quantum matter isolated from the environment mediates the interaction between photons via nonlinear optical processes [Cirac et al., 1997].

For years, scientists have observed nonlinear processes in bulk nonlinear materials of sufficiently intense laser beams. Much effort has been spent to advance their efficiency, resulting in the observation of nonlinear behavior of materials at lower light intensity level [Byer, 1997]. However, generating an optical response that is nonlinear at a level of individual photons is still a formidable challenge. This is because a strong nonlinear response requires the amplitude of the electric field of the light beam to be on the same order of magnitude as the field of the nucleus [Chang et al., 2014]. Another hand-waving argument is to consider the probability that a single photon can be scattered by a single atom. This probability is given by the ratio of absorption cross section of the atoms ($\sigma \approx \lambda^2$) and the transverse area of the laser beam ($\sim w^2$). Due to the diffraction limit, the laser beam can be focused to a

minimum waist of the wavelength scale ($w \sim \lambda$), hence the probability of scattering in free space is typically much smaller than unity.

A possible solution is the use of atomic ensembles that consists of a large number of particles. By employing an electromagnetically induced transparency (EIT) scheme, the photonic states can be mapped to a collective state of the atomic ensembles and coherently retrieved later [Lukin et al., 2001, Fleischhauer et al., 2005]. Recent results in this research direction include the storage and generation of nonclassical light fields [Li et al., 2013, Maxwell et al., 2013], single-photon switches and amplifiers [Baur et al., 2014], and the realization of the quantum repeaters which are crucial for the task of distribution of quantum states over long distances [Sangouard et al., 2011].

The work in this thesis focuses on a different approach, where the stationary qubit consists of single trapped neutral atoms. A single two-level atom is arguably the most natural way to implement the nonlinearity as it cannot absorb or emit two photons at the same time. In addition, a single trapped atom can be addressed individually and manipulated with high precision. Beside the radiative coupling to the vacuum field, single atoms can be decoupled almost completely from the environment by trapping and cooling techniques [Metcalf and van der Straten, 2007]. However, as explained above, the light-matter coupling in free space at the level of individual quanta is not large.

One technique to enhance the atom-photon interaction is to increase the electric field strength of a single photon via the use of optical cavities. Intuitively, the cavity increases the photon scattering probability by the number of roundtrips made by the photons in the cavity. In the frequency domain, the cavity imposes a discrete mode spectrum of photons. Therefore, the density of states near a cavity resonance that is close to the emission frequency of the atoms can be enhanced. This enhancement leads to an increase of spontaneous emission rates into the cavity mode. Research in this direction began with Rydberg atoms in microwave resonators [Raimond et al., 2001, Walther et al., 2006], but then has extended into the optical domain and matured into an established field of cavity quantum electrodynamics (CQED) [Kimble, 1998, Reiserer and Rempe, 2015].

A generic CQED system consists of a single atom trapped at the antinode of the cavity field. The two-level atom exchanges energy with the optical field at a

rate characterized by the atom-cavity coupling strength g_0 . The coupling strength depends on how susceptible the atom is to make an electronic transition, as well as the electric field strength of a single photon at the location of the atom. The latter is inversely proportional to the the cavity mode volume, which is defined as the integral of the squared cavity spatial mode [Kimble, 1998]. In addition to the coherent interaction that governs the internal dynamics of the system, there is dissipation that arises from the coupling to a continuous background of modes in the environment. In particular, the atom can emit photons to modes rather than the cavity modes, and this spontaneous emission contributes to energy losses of the system. For cavities that cover a small solid angle, the atomic decay rate (γ) is independent of the cavity geometry and constant for a specific atomic transition. Damping of the cavity field through the cavity mirrors is accounted for by a decay rate

$$\kappa \sim \frac{1}{\mathcal{F}l_{cav}}, \quad (1.0.1)$$

where \mathcal{F} is the cavity finesse and l_{cav} is the cavity optical length.

To utilize a single atom to obtain a nonlinear interaction between photons, the cavity QED system is required to be in the strong coupling regime, in which the coupling between the single atom and a cavity mode must exceed the decay rates: $g_0 \gg (\kappa, \gamma)$. This is reflected by the single-atom cooperativity parameter which is defined as

$$C = \frac{g_0^2}{2\kappa\gamma} \gg 1. \quad (1.0.2)$$

Several designs of optical resonators exist toward realizing the strong coupling regime by either increasing g_0 or minimizing κ and γ . The search for strong coupling in the optical domain began in 1980s and has been active until now. The most common configuration is high finesse Fabry-Perot cavities [Reiserer and Rempe, 2015]. These cavities consist of two curved mirrors with superpolishing surface and ultrahigh reflectivity coating facing each other. The mirror separation is typically on the order of a few hundreds of micrometers which places the cavity in the near-planar regime, where the cavity mode resembles a plane wave. Due to the short cavity length, the requirement for the cavity finesse is high in order to keep the cavity linewidth reasonably narrow. For this design, a typical value of the cavity finesse is on the order

of millions while the transmission and losses of each mirror are below 1 ppm [Kimble, 1998]. Despite of remarkable demonstration of quantum information processing tasks by using these high finesse microcavities, the scaling of this technique remains a question due to the sophisticated coating of the mirrors. In addition, the atom-cavity coupling strength is bounded to a few 100 MHz due to the penetration of the cavity field into the thick mirror coating which consist of multiple dielectric interference layers to achieve a high cavity finesse [Hood et al., 2001].

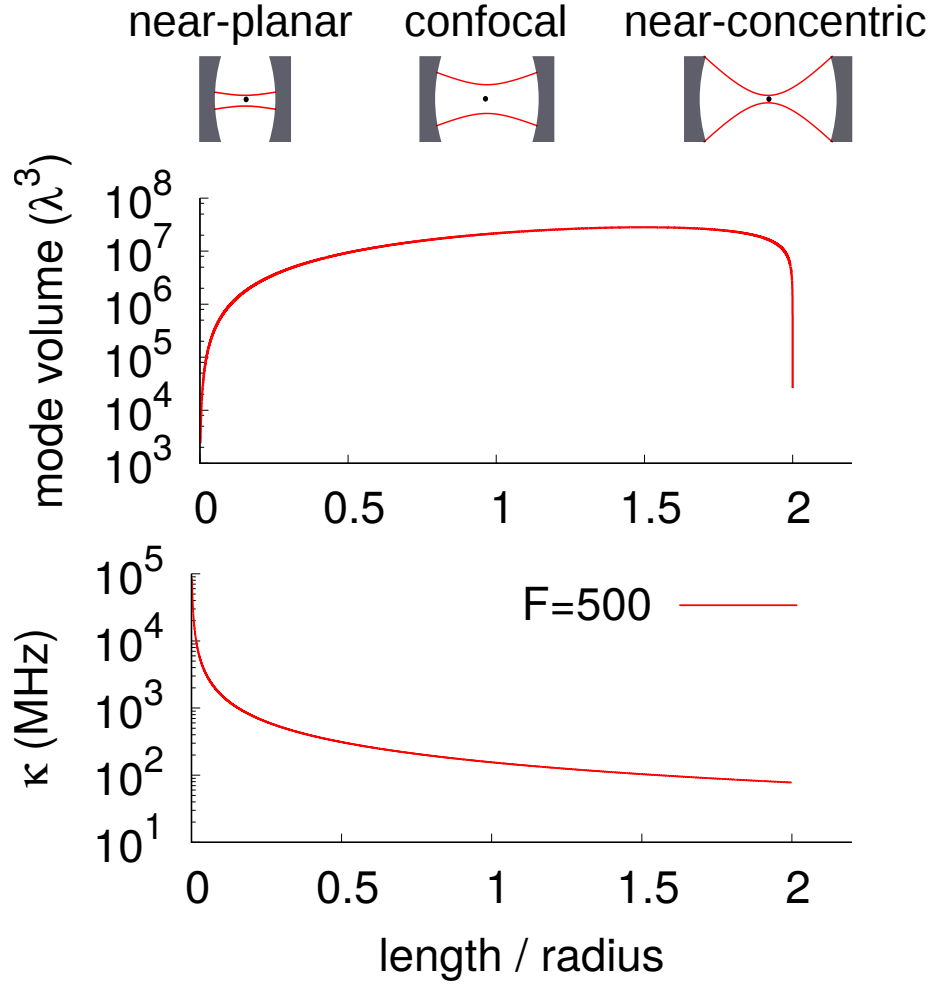


Figure 1-1: Mode volume and linewidth of optical cavities of different geometrical configurations. Near-concentric cavities minimize both the mode volume and linewidth for a given cavity finesse and mirrors' radius of curvature. Top insets show the mode profile at three important cavity regimes.

As a result, new types of cavities and resonant structures to improve the coupling strength have been considered recently. Typical designs include whispering-gallery modes in microspheres, microtoroids and bottle resonators [Vahala, 2003]. For these cavities, the light field is contained and guided in the photonic material, typically made of silicon dioxide. Hence, the atom can only couple to the evanescent field within a distance of hundreds nanometers outside photonic structures. The limit of this approach lies at the difficulties of the trapping of atoms near to dielectric surfaces. Another method to form a cavity with a small mode volume is a fiber-based Fabry-Perot resonator. In this approach, the end facets of two optical fibers are laser-machined to form cavity mirrors with small radii of curvature [Hunger et al., 2010]. Common to these designs is that they require understanding of the fabrication process of the cavities.

Here, we explore an alternative approach of making a small mode volume cavity, not by reducing the physical size of the cavity, but via a strong focusing technique [Morin et al., 1994, Durak et al., 2014, Nguyen et al., 2017]. In particular, we are interested in exploring advantages of the strong focusing mode of near-concentric cavities to realize the strong atom-light interaction, and hence the two-photon non-linearity. Among all geometrical configurations of the Fabry-Perot cavities, the near-concentric cavity, where the cavity length matches twice the radius of curvature of the mirrors, has the strongest focusing mode and a cavity beam waist that can reach a diffraction-limited size of $\lambda/2$. Hence, a small mode volume and, consequently, a strong atom-photon interaction can be obtained even with millimeter cavity lengths. In addition, the millimeter cavity length alleviates the requirement of high finesse. As shown in Fig. 1-1, for a given radius of curvature of the mirrors and a cavity finesse, the near-concentric cavity minimizes both the mode volume and the cavity decay rate. Additional advantages include more optical access to the center of the cavity, where the atoms will be trapped and interact with the cavity mode. For use with trapped ions, the large separation between two mirrors provides the ability to avoid charging problems with dielectric surfaces, which has been a major hindrance to the development of ion traps in optical cavities [Harlander et al., 2010]. As near-concentricity is simply a geometrical configuration of the Fabry-Perot cavities, the techniques developed here can be easily adapted to other types of cavities such as the fiber-based

cavities [Hunger et al., 2010]. Another intriguing aspect of concentric cavities is that the frequencies of the higher-order transversal modes are degenerate. This could allow the realization of multimode cavity QED in the strong coupling regime [Wickenbrock et al., 2013]. Outside of the atomic physics community, near-concentric cavities are gaining more attentions. There are suggestions of using near-unstable cavities such as near-concentric cavities to reduce the influence of thermal noise of the mirror coatings on gravitational wave detectors [Wang et al., 2018].

This thesis presents the first step toward the realization of strong atom-cavity coupling regime in a near-concentric cavity. In particular, the experiment performed in this thesis employs a special design of cavity mirrors to form a near-concentric cavity with a length of 11 mm. The cavity finesse is measured to be 600 which corresponds to a linewidth of 22.5 MHz when tested outside the vacuum system. Chapter 2 gives an overview of the theoretical description of the atom-cavity system. Chapter 3 and 4 cover an alignment technique that was developed to position the mirrors with sufficient accuracy such that the cavity can be kept stable in both transverse and longitudinal directions at the last few resonance lengths with a 780 nm laser. Trapping and detection of single atoms is presented in chapter 5. Onset of the normal mode splitting from a single atom in the near-concentric cavity is observed and analyzed in chapter 6. Chapter 7 concludes the experimental results and provides an outlook on future experiments that could be feasible based on the results of the work presented in this thesis.

Chapter 2

Theory

This chapter provides theoretical concepts behind the interaction between a two-level atom interacting with a single mode of the electromagnetic field contained in an optical cavity. In the absence of dissipation, the dynamic of the atom-cavity system is described by the Jaynes-Cummings Hamiltonian (section 2.1). Inclusion of irreversible losses leads to concepts of strong and weak coupling regimes (section 2.2). To obtain the strong coupling, the interaction strength between the atom and the cavity must dominate the dissipation rates. The interaction strength is proportional to the atomic dipole moment and the amplitude of the cavity field. The latter is determined by the cavity geometry. However, not all cavity configurations can be useful in the context of cavity QED as some cavities do not support a stable mode. Section 2.4 introduces the concept of cavity stability limit, provides an overview of some stable configurations of Fabry-Perot cavities and predict their interaction strength with the atoms.

2.1 A spin and a spring: the Jaynes-Cummings model

We consider a two-level atom with an excited state $|e\rangle$ and a ground state $|g\rangle$, connected by an electric dipole transition at an angular frequency ω_a . The dynamics of this system is equivalent to a spin 1/2 system locating in a magnetic field; the two electronic states correspond to eigenstates of the spin along the magnetic field direction. Here, we adopt the second quantization method and describe the excita-

tion and de-excitation of the atom with atomic raising and lowering Pauli operators: $\sigma^+ = |e\rangle\langle g|$ and $\sigma^- = |g\rangle\langle e|$. Setting the ground state energy zero, the Hamiltonian for the two-level atom is

$$H_a = \hbar\omega_a\sigma^+\sigma^- \quad (2.1.1)$$

Along the similar line with the classical theory of dipole radiation, we need to know the dipole moment of the atom to describe the interaction with the radiation field. The dipole moment is written as

$$\mathbf{d} = -q\mathbf{r}, \quad (2.1.2)$$

where q is the elementary charge, and \mathbf{r} is the operator of the position vector of the electron. Assuming the atomic eigenstates $|e\rangle$ and $|g\rangle$ have opposite parities, we have $\langle e|\mathbf{r}|e\rangle = \langle g|\mathbf{r}|g\rangle = 0$. Consequently, the dipole moment is non-diagonal in the basis spanned by $|e\rangle$ and $|g\rangle$

$$\mathbf{d} = \mu_{eg}(\sigma^+ + \sigma^-), \quad (2.1.3)$$

where $\mu_{eg} = q\langle e|\mathbf{r}|g\rangle$ is the dipole moment associated with the transition between the two states.

A single mode of the electromagnetic field contained in a cavity is dynamically equivalent to a quantum harmonic oscillator. The Hamiltonian of a cavity field with a resonant frequency of ω_c is

$$H_{cav} = \hbar\omega_c(a^\dagger a + \frac{1}{2}), \quad (2.1.4)$$

where a and a^\dagger are the creation and annihilation operators for the cavity mode, respectively. Energy eigenstates of the cavity field are the Fock states, denoted as $|n\rangle$ where n is the number of photons in the cavity. Then, it is clear that each photon has an energy of $\hbar\omega_c$. The electric field operator is written as

$$\mathbf{E} = \hat{e}\sqrt{\frac{\hbar\omega_c}{2\epsilon_0 V}}(a + a^\dagger), \quad (2.1.5)$$

where \hat{e} is the polarization vector of the field, ϵ_0 is the vacuum permittivity, and V is the effective mode volume. The effective mode volume is a measure of the confinement

of the electric field of a single photon in the cavity, and therefore determined by cavity geometrical parameters: mirror' radii of curvature and the cavity length. The interaction Hamiltonian between the atom and the cavity field has the same form as the energy of a classical dipole in a classical radiation field, which is

$$H_{int} = \mathbf{d} \cdot \mathbf{E} \quad (2.1.6)$$

It now follows, on substituting for \mathbf{d} and \mathbf{E} from Eqs. 2.1.3 and 2.1.5 into Eq. 2.1.6, that

$$H_{int} = \hbar g_0 (\sigma^- + \sigma^+) (a^\dagger + a), \quad (2.1.7)$$

where g_0 describes the atom-cavity coupling strength. The coupling strength is proportional to the dipole matrix element μ_{eg} between the two levels and inversely proportional to the square root of the effective mode volume V :

$$g_0 = \frac{\mu_{eg} E}{\hbar} = \sqrt{\frac{\omega_c}{2\epsilon_0 V \hbar}} \mu_{eg}. \quad (2.1.8)$$

The term σa in the interaction Hamiltonian describes the process in which the energy of the atom and the field both increase; whereas $\sigma^+ a^\dagger$ describes the process in which their energy both reduce. Thus, they violate the energy conservation, and can only be observed in timescales compatible with the uncertainty principle. In the rotating wave approximation, these terms can be neglected, and we can simplify the interaction Hamiltonian to

$$H_{int} = \hbar g_0 (a^\dagger \sigma^- + a \sigma^+). \quad (2.1.9)$$

The physical interpretation of this Hamiltonian is that the atom and the cavity interact by exchanging one quantum of excitation with a rate determined by the coupling strength g_0 .

The complete Hamiltonian of the atom-cavity system takes the final form of

$$H = H_a + H_{cav} + H_{int}, \quad (2.1.10)$$

$$= \hbar \omega_a \sigma^+ \sigma^- + \hbar \omega_c a^\dagger a + \hbar g_0 (a^\dagger \sigma^- + a \sigma^+), \quad (2.1.11)$$

which is known as the Jaynes-Cummings Hamiltonian [Jaynes and Cummings, 1963].

The eigenstates and eigenvalues of the coupled system can be found analytically by diagonalizing the interaction Hamiltonian in Eq. 2.1.11. In the limit of vanishing coupling strength ($g_0 \rightarrow 0$), the eigenstates of the system simply are $|g, n\rangle$ and $|e, n\rangle$, which are the products of the atomic and cavity eigenstates. When the interaction is turned on, these states are coupled and the eigenstates are found to be rotation of the uncoupled eigenstates $|e, n-1\rangle$ and $|g, n\rangle$:

$$\begin{aligned} |+, n\rangle &= \cos \theta |e, n-1\rangle + \sin \theta |g, n\rangle, \\ |-, n\rangle &= -\sin \theta |e, n-1\rangle + \cos \theta |g, n\rangle. \end{aligned}$$

The mixing angle θ reflects the relative contribution of the atom and the cavity to the coupled states and depends on the coupling strength g_0 and the atom-cavity detuning $\Delta_{ac} = \omega_c - \omega_a$ as

$$\theta = \arctan \frac{g_0}{-\Delta_{ac}/2 + \sqrt{g_0^2 + (\Delta_{ac}/2)^2}}. \quad (2.1.12)$$

On resonance $\Delta_{ac} = 0$, the eigenstates of the coupled system are the Bell states:

$$|\pm, n\rangle = \frac{1}{\sqrt{2}} (|e, n-1\rangle \pm |g, n\rangle). \quad (2.1.13)$$

The energy level of the coupled system is shown in Fig. 2-1 The coupled atom-photon states are referred to as dressed states, and the ladder of doublets is called the Jaynes-Cummings ladder. The coupled energy eigenvalues are

$$E_{\pm, n} = n\hbar\omega_c - \hbar\frac{\Delta_{ac}}{2} \pm \frac{\hbar}{2}\sqrt{\Delta_{ac}^2 + 4g_0^2n}. \quad (2.1.14)$$

The atom-cavity coupling induces a splitting in the energies of the excited states $E_{\pm, n}$ by $\Delta E = E_{+, n} - E_{-, n} = \hbar\sqrt{\Delta_{ac}^2 + 4g_0^2n}$. As a result, the spectrum of the coupled atom-cavity system exhibits a distinctive doublet corresponding to resonant frequencies of $|\pm, n\rangle$, in contrast to a single peak in the case of empty cavities. Borrowing terms from classical mechanics, the coupling induced frequency splitting is called the normal mode splitting.

On resonance, the normal mode splitting increases nonlinearly as $\hbar 2g\sqrt{n}$. This photon-number dependent energy spectrum gives rise to the photon blockade effect, in which the excitation of the atom-cavity system by one single photon blocks the

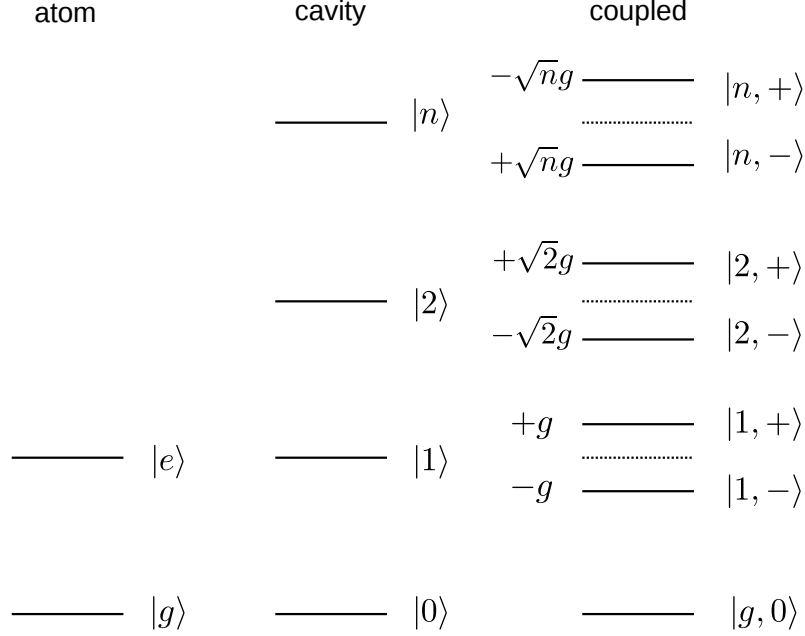


Figure 2-1: The Jaynes-Cummings ladder for resonant case $\Delta_{ac} = \omega_a - \omega_c = 0$. The energy level structure is a series of doublets representing normal-modes of the coupled atom-cavity system.

transmission of the second photon for a particular laser frequency [Birnbbaum et al., 2005].

The atom-cavity coupling strength not only determines how the atom-cavity system can be driven, but also governs the internal dynamics of the system. Assuming the atom is initially excited inside a cavity containing $n - 1$ photons, the initial state of the system is thus $|e, n - 1\rangle$, which can be expressed as a linear superposition of the eigenstates

$$|\Psi(t = 0)\rangle = |e, n - 1\rangle = \frac{1}{\sqrt{2}} (|+, n\rangle + |-, n\rangle). \quad (2.1.15)$$

The time evolution of the state can be found by solving the time-dependent Schrodinger equation:

$$H |\Psi(t)\rangle = i\hbar \frac{d|\Psi(t)\rangle}{dt}, \quad (2.1.16)$$

$$|\Psi(t)\rangle = \frac{1}{\sqrt{2}} (e^{-iE_{+,n}\hbar/t} |+, n\rangle + e^{-iE_{-,n}\hbar/t} |-, n\rangle). \quad (2.1.17)$$

We are interested in the probability of the atom emitting a photon to the cavity and decaying to the ground state:

$$P_{e \rightarrow g}(t) = \langle g, n | \Psi(t) \rangle^2 = \frac{1}{2} [1 - \cos(2g_0\sqrt{n}t)]. \quad (2.1.18)$$

This transition probability describes a Rabi oscillation between $|g, n\rangle$ and $|e, n-1\rangle$ at a frequency of $\Omega = 2g_0\sqrt{n}$. For the case when no photons are initially present in the cavity, $\Omega = 2g_0$. As the oscillation involves the vacuum field, $2g_0$ becomes known as the vacuum-Rabi frequency. In this thesis, we often refer to g_0 as the atom-cavity coupling strength.

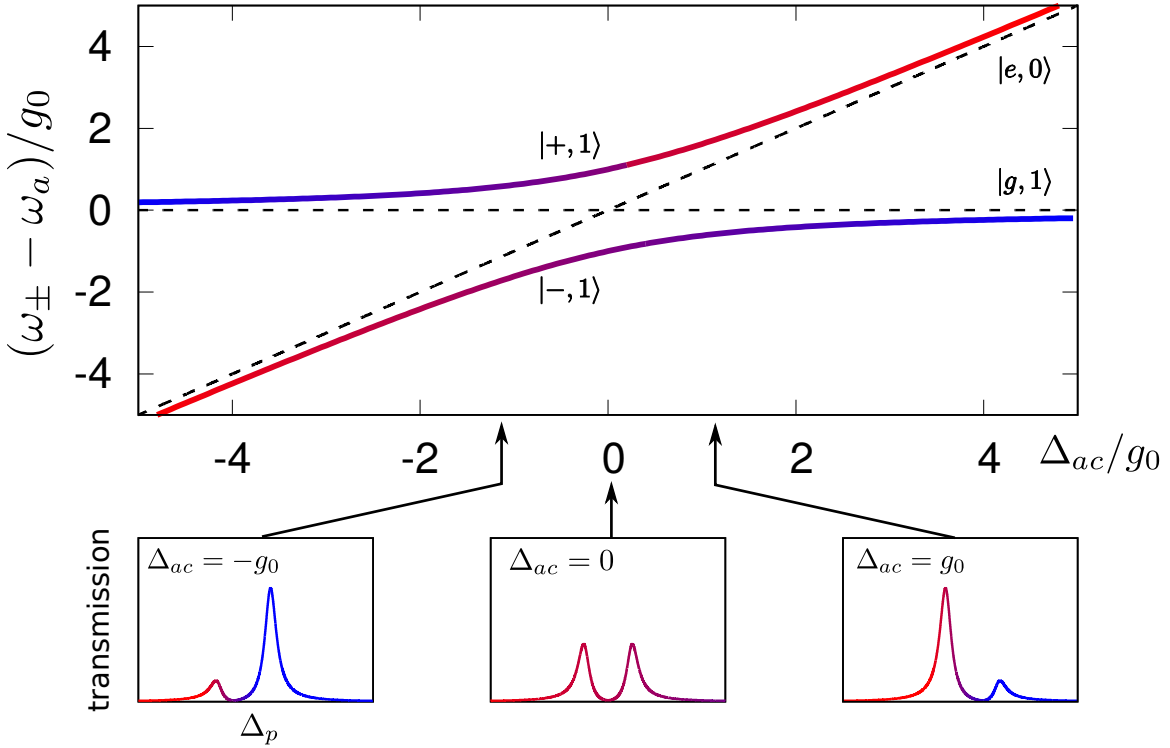


Figure 2-2: Spectroscopy of the Jaynes-Cummings ladder. Top: resonant frequencies ω_{\pm} of the uncoupled system (dash lines) and coupled system (solid lines) when the cavity frequency is fixed and the atomic frequency is tuned over the resonance. Colour indicates the relative amplitude of the atomic bare state $|e, 0\rangle$ (more red), and the cavity bare state $|g, 1\rangle$ (more blue). At $\Delta_{ac} = 0$, Bottom: cavity transmission spectra at different atom-cavity detuning of a weak probe beam such that only the first doublet is excited.

2.2 Damped atom-cavity system

In most of experimentally relevant cases, the atom-cavity system is not completely isolated but is coupled to an environment. This system-environment interaction introduces dissipation and decoherence affecting both the atom and the cavity field. The environment we consider here is the electromagnetic vacuum consisting of a continuous background of modes. The effects of the environment on the system can be classified into two loss channels.

The first loss channel is the spontaneous emission of the atoms into free-space modes rather than the cavity modes. We characterize this loss channel with a rate 2γ . For a cavity covering a solid angle of $\Delta\Omega$, assuming the atoms are unpolarized and have an isotropic radiation, γ is given by

$$\gamma = \frac{\Gamma}{2} \left(1 - \frac{\Delta\Omega}{4\pi}\right), \quad (2.2.1)$$

where Γ is the free-space spontaneous-emission rate.

The second loss channel is the damping of the energy of the cavity mode at a rate 2κ . This damping is due to transmission and losses of photons at the cavity mirrors.

A standard approach to describe the evolution of an open quantum system is to use a Master equation written in the Lindblad form [Carmichael, 1998]. Here, we take an equivalent approach using an effective Hamiltonian [Lien et al., 2016],

$$H_{\text{eff}} = H - i\kappa a^\dagger a - i\gamma \sigma^+ \sigma^-. \quad (2.2.2)$$

The properties of the damped atom-cavity system can be encapsulated in eigenvalues λ_\pm of the effective Hamiltonian H_{eff} . As the Hamiltonian H_{eff} accounts for the dissipation, it is non-Hermitian, and consequently λ_\pm are complex. The eigenvalues can be cast into a more meaningful form of $\lambda_\pm = E_\pm - i\hbar\chi_\pm$. The real parts E_\pm are the eigen-energies of the atom-cavity system and the imaginary part χ_\pm are the linewidths. Consequently, $\omega_\pm = E_\pm/\hbar$ are the resonant frequencies.

In the following, we restrict our description to a subspace spanned by the ground state and the first excitation manifold, $\{|g, 0\rangle, |g, 1\rangle, |e, 0\rangle\}$. This restriction applies for experiments in which the atom-cavity system is probed by a weak laser beam. Diagonalizing H_{eff} , the complex eigenvalues λ_\pm can be expressed as

$$\lambda_{\pm}/\hbar = \frac{\omega_c + \omega_a - i(\kappa + \gamma)}{2} \pm \sqrt{g_0^2 + \left[\frac{\omega_c - \omega_a - i(\kappa - \gamma)}{2} \right]^2}. \quad (2.2.3)$$

With dissipation, the Rabi frequency is no longer simply $g_0\sqrt{n}$ but also dependent on the decay rates:

$$\hbar\Omega_n = E_+ - E_- = 2 \operatorname{Re} \left(\sqrt{g_0^2 - \frac{(\kappa - \gamma)^2}{4}} \right). \quad (2.2.4)$$

A simple way to assess the coupling strength is the critical atom number N_0 , defined as the number of atoms required to significantly affect the transmission of the cavity. The inverse of N_0 denotes the single-atom cooperativity C , which is defined as

$$C = \frac{g_0^2}{2\gamma\kappa}. \quad (2.2.5)$$

Similarly, a critical photon number n_c determines the number of photons required to saturate the atomic transition:

$$n_c = \frac{\gamma^2}{2g_0^2}. \quad (2.2.6)$$

2.3 Coupling regimes

The dissipation broadens the range of dynamics of the atom-cavity system. Depending on the ratio of the three rates (g_0, κ, γ) , three coupling regimes of cavity QED can be identified in experiments (see Fig. 2-3). In the following, we describe the basic physical effects of each regime in more detail.

Weak and intermediate coupling regimes

If $g_0 \ll \kappa, \gamma$, the dissipation dominates the dynamics of the system and the coupling between atom and cavity can nearly be ignored. In this weak coupling regime, from Eq. 2.2.4, the Rabi frequency Ω_n is zero, and hence there is no normal mode splitting (see zone (i) of Fig. 2-3). From the physics point of views, the atom and the cavity are nearly uncoupled and retain their individual properties.

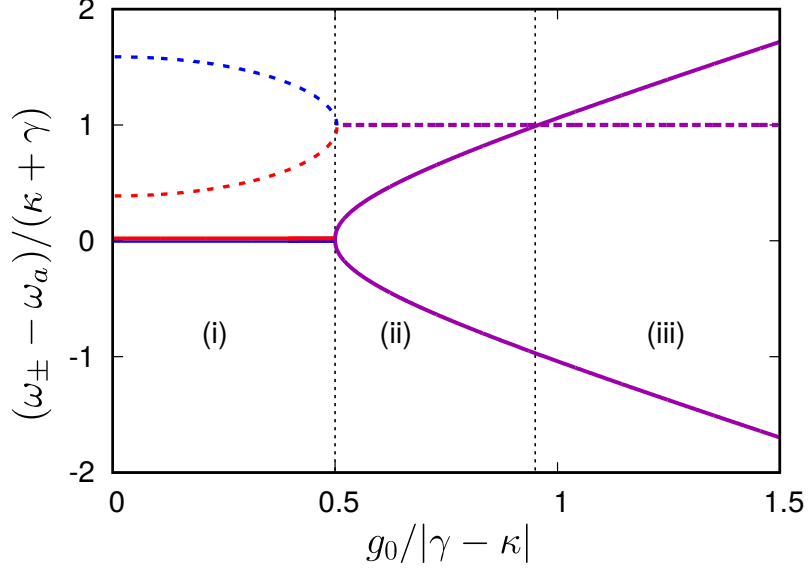


Figure 2-3: Coupling regimes of the atom-cavity system. Solid curves: normalized resonant frequencies; dashed curves: normalized decay rates. Colour indicates the relative amplitude of the atomic bare state $|e, 0\rangle$ (more red), and the cavity bare state $|g, 1\rangle$ (more blue). Zones (i),(ii) and (iii) correspond to the weak regime, the intermediate regime and the strong coupling regime respectively.

Increasing g_0 till $\kappa \gg g_0 \gg \gamma$ and $C \gg 1$, we enter the Purcell regime. The vacuum-Rabi oscillation still cannot be observed as the photons quickly escape the cavity before being absorbed by the atoms. In this regime, the eigenstate $|+, n\rangle$ is mainly represented by the atomic states, and hence E_+ and χ_+ are the new atomic resonant frequencies and the decay rate modified by the cavity, respectively. From Eq. 2.2.3, the atomic decay rate γ_c into the cavity mode is

$$\gamma_c = \chi_+ = \gamma \left(1 + \frac{g^2}{\gamma\kappa} \right) \approx \frac{g^2}{\kappa}, \quad (2.3.1)$$

which is equivalent to

$$\frac{\gamma_c}{\gamma} = 2C. \quad (2.3.2)$$

This enhancement of atomic emission rate of a factor proportional to the cooperativity C is known as the Purcell effect and was exploited to realize efficient sources of single photons [Kuhn et al., 2002].

The normal-mode splitting appears only when $g_0 \gg |\kappa - \gamma|/2$ (see zone (ii) of

Fig. 2-3). In this regime, the damping rate of the atoms and the cavity merges to a mean value of $(\kappa + \gamma)/2$. However, the doublet of the normal modes is not clearly resolved as the splitting is still smaller the damping rate, and hence this regime is referred to as the intermediate coupling regime.

Strong coupling regime

The strong coupling regime corresponds to zone (iii) of Fig. 2-3. In this regime, the atom-cavity coherent coupling dominates the two dissipative rates:

$$g_0 \gg \kappa, \gamma \implies C \gg 1 \quad (2.3.3)$$

The dynamics of the system is marked by the coherent exchange of energy between the atom and the cavity. However, the population of excitation within each doublet is no longer conserved as in the lossless case, but transferred from $|\pm, n\rangle$ to the lower doublet at a decay rate of χ_{\pm} . For strong coupling systems, the decay rate of the normal modes are identical and equal to

$$\chi_{\pm} = \chi = \frac{\gamma + \kappa}{2} \quad (2.3.4)$$

Hence, multiple Rabi oscillations occur before the dissipation takes place and removes the energy from the system. In contrast to the ideal lossless case, the Rabi frequency $\Omega_{n=0}$ depends on both g_0 and the imbalance between the two decay rates

$$\Omega_0 = 2g_0 - \frac{(\kappa - \gamma)^2}{4g_0}. \quad (2.3.5)$$

2.4 Cavity configuration and stability

A single mode of electromagnetic field is experimentally realized by confining light in optical resonators. The most common type of optical resonators is Fabry-Perot cavities which consist of two facing mirrors with radii of curvature R_1 and R_2 separated by a distance l_{cav} . Light is confined in such cavities by reflecting multiple times from the mirrors and interfering. Due to the interference, only certain intensity distributions are reproduced after every round trip in the cavities. These radiation patterns

are known as eigenmodes, and the cavities that support these modes are referred to as stable cavities. Eigenmodes in stable cavities can be divided into two types: longitudinal modes which have the same transverse intensity pattern but differ in resonant frequencies; and transverse modes which may differ in both. Of particular interest to this work and many other experiments in cavity QED is fundamental transverse modes described by a Gaussian beam and their interaction with atoms. The effective mode volume that determines the atom-cavity coupling strength of these fundamental modes is $V = 1/4\pi w_0^2$, where w_0 is the waist of the Gaussian beam or the cavity beam waist.

Not every optical cavity is stable. An example of unstable cavities is formed by two convex mirrors; light in such cavity diverges progressively when reflecting from the mirrors, and eventually escapes the cavity. Two mirrors acts as a stable cavity only when

$$0 \leq \left(1 - \frac{l_{cav}}{R_1}\right) \left(1 - \frac{l_{cav}}{R_2}\right) \leq 1, \quad (2.4.1)$$

which is often referred to as the stability criterion and can be derived by using methods such as the ray transfer matrix analysis [Siegman, 1986]. To describe the cavity properties, it is useful to introduce stability parameters

$$g_1 = 1 - \frac{l_{cav}}{R_1} \quad \text{and} \quad g_2 = 1 - \frac{l_{cav}}{R_2}. \quad (2.4.2)$$

In terms of these parameters, the stability criterion is simplified to

$$0 \leq g_1 g_2 \leq 1, \quad (2.4.3)$$

and the cavity beam waist is

$$w_0^2 = \frac{l_{cav}\lambda}{\pi} \sqrt{\frac{g_1 g_2 (1 - g_1 g_2)}{(g_1 + g_2 - 2g_1 g_2)^2}}, \quad (2.4.4)$$

where λ is the wavelength of light that is resonant with the cavity.

It is convenient to visualize cavities in the stability diagram in which each cavity can be represented by a point in the $g_1 g_2$ plane. The stability criterion described in Eq. 2.4.3 infers that the region of stable cavities in the $g_1 g_2$ plane is bounded by the

coordinate axes and the hyperbolas $g_1 g_2 = 1$; whereas outside this region corresponds to unstable cavities. Near to the hyperbolas, cavities are susceptible to both misalignment in transverse direction and any tilting between two optical axes of cavity mirrors. Perhaps the most common configurations of cavity are symmetric cavities,

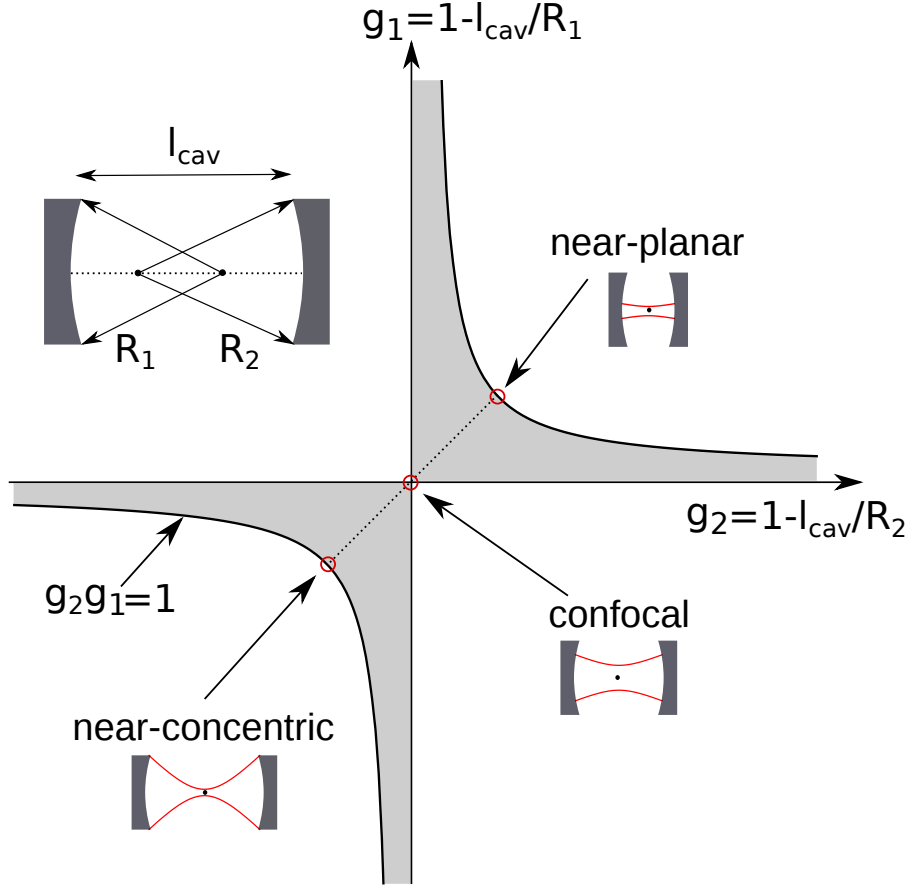


Figure 2-4: The stability diagram for two-mirror optical cavities. The grey area indicates the stable region.

which have mirror curvatures $R_1 = R_2 = R$, and hence the stability parameters $g_1 = g_2 = g = 1 - l_{cav}/R$. Three examples within this class are of special interests to the study of atom-light interaction:

- **Confocal cavities:** The central point in the stability diagram is the symmetric confocal stable cavity with $R = l_{cav}$ and $g = 0$. The focal points of the cavity mirrors coincide with each other at the cavity center. Hence, though locating near to

the stability limit, the confocal cavity is insensitive to misalignment. Tilting of the mirrors only displaces the optical axis of the cavity by a small amount.

- **Near-planar cavities:** Mirrors that have long radii of curvature ($R \gg l_{cav}$) form a near-planar cavity. As the cavity length is shorter than the two times of the Rayleigh range, the cavity waist varies only slightly in the near-planar cavity. The cavity waist and the mirror spot sizes are nearly equal to

$$w_0^2 \approx \frac{l_{cav}\lambda}{\pi} \sqrt{\frac{R}{2l_{cav}}} \quad (2.4.5)$$

- **Near-concentric cavities:** In the region closer to the lower limit, $g \rightarrow -1$, the cavity length is slightly lesser than two times of the radius of curvature. This cavity is referred to as the near-concentric cavity and has a very strong focusing mode with a cavity waist of

$$w_0^2 \approx \frac{l_{cav}\lambda}{\pi} \sqrt{\frac{(2R - l_{cav})}{8l_{cav}}}, \quad (2.4.6)$$

which can be on the order of a few μm [Stute et al., 2012, Nguyen et al., 2017]. As near-concentric cavity waist are very small, they are not useful in laser designs which often require large cavity mode volumes to interact with bulky lasing medium, and hence have not been widely used before. However, in the context of cavity QED in which the medium consists of only one or a few atoms, the near-concentric cavity can offer strong interaction as the cavity field is concentrated to locations of the atoms with a cavity waist comparable to σ_{abs} , the absorption cross section per atom.

To obtain the strong coupling regime with a given atomic transition, one need to maximize g_0 and minimize the cavity decay rate κ . As shown in Fig. 2-5, the coupling strength g_0 can be optimized by choosing either near-planar with very short cavity lengths or near-concentric cavities as the mode volumes are minimal at these two cavity configurations. However, to keep cavity decay rate low enough, which scales as $\kappa \propto 1/F l_{cav}$, the near-planar cavities require mirrors with a very high finesse. On the other hand, the near-concentric cavities can keep the decay rate low with a decent cavity finesse. This describes the motivation behind using near-concentric cavities for

cavity QED experiments.

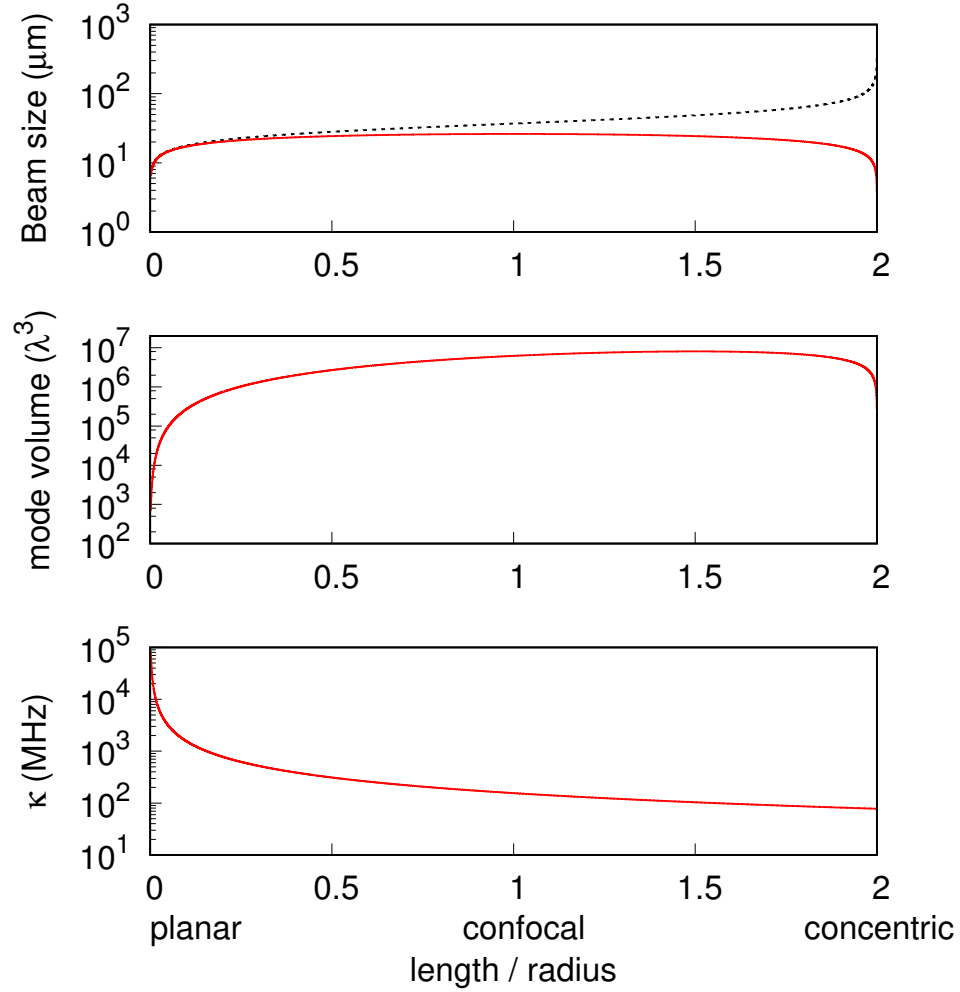


Figure 2-5: Comparison of properties of a fundamental transverse mode for stable cavity configurations. The cavity is formed by a pair of mirrors with the radius of curvature of $R = 5$ mm and a finesse of 500. Top: beam size of the cavity mode at the mirrors (dashed line) and the cavity waist at the center (solid line). Middle: effective mode volume in the unit of λ^3 where $\lambda = 780$ nm. The mode volume is minimum at the near-planar and near-concentric regime and maximum at $l_{cav}/R = 3/2$. In the near-concentric region, the mode volume reduce more rapidly than the near-planar region. Bottom: the cavity loss (κ) inversely proportional to l_{cav} .

Chapter 3

Building a near-concentric cavity

This chapter provides a “recipe” to build a near-concentric Fabry-Perot optical cavity. In particular, we present a detailed description of a cavity design and a step-by-step instruction to construct and align the near-concentric cavity. The constructed cavity has a length that can be varied from $3.5\,\mu\text{m}$ shorter to $1\,\mu\text{m}$ longer than the critical length. Further, we discuss techniques for characterizing cavity length and perform an analysis of cavity modes at the last resonant cavity length for laser light at $780\,\text{nm}$, which corresponds to a distance of $207(3)\,\text{nm}$ away from the critical length and a stability parameter $g = -0.99996(28)$. At this length, we obtain a coupling efficiency of 37% into a fundamental mode of the cavity. The cavity fundamental mode maintains similar cavity linewidths and transmission as the nominal values. Some design challenges and technical hurdles about working with near-unstable cavities are also discussed. At the end of the chapter, we present a new design of the cavity mount to overcome the alignment difficulties.

3.1 Design of the cavity

The cavity system is designed to obtain a strong interaction with a single trapped ^{87}Rb atom. Drawing on previous experiences of trapping a single atom between a pair of high-numerical-aperture lenses and some previous attempts to construct the concentric cavities, we consider the following aspects for our cavity design:

Compactness. The system is located inside a glass cuvette with a size of $25 \times$

25 × 150 mm, which provides a convenient optical access to the cavity focus for other optical beams preparing atoms in experiment. Moreover, by using a compact cuvette, magnetic coils can be reduced in size, and hence, require only a low current to generate a sufficient magnetic field gradient (~ 20 G/cm) for the magneto-optical trap (MOT) with little heat generation.

Tunability. The positions of the cavity mirrors are adjustable in both axial and transverse direction with sub-nanometer resolution, and a travelling range of more than a few microns.

MOT formation. As we would like to form a MOT directly inside the cavity, there must be optical access for three cooling laser beams. In addition, a clear path must exist between the atom dispenser and the center of the cavity. However, a line-of-sight between the cavity mirrors and the dispenser must be avoided to prevent the contamination of the cavity mirrors.

In addition to these geometrical constraints, the cavity needs to be stabilized during the experiment. In the following sections, each components of the design will be discussed in more details.

3.1.1 Mirror design

Central to the experiment is a pair of cavity mirrors, separated by a distance of approximately 11 mm ($l_{cav} \approx 11$ mm). The cavity mirrors are manufactured by Asphericon and made of N-SF11 glass. One surface is superpolished into a spherical form with a radius of curvature of 5.5 mm ($R_C = 5.5$ mm) and a diameter of 8.39 mm in cross section (see Fig. 3-1). The spherical surface has a high reflectivity (HR) coating and, hence, acts as a cavity mirror. The HR coating of the cavity mirrors has a nominal value of 99.5% with the central wavelength at 780 nm, which corresponds to cavity finesse of $\mathcal{F} \sim 600$. Because all mirrors are coated in the same coating run, it is reasonable to assume that they have identical optical properties. We will revisit this assumption again in the discussion about mirror losses.

The choice of $R_C = 5.5$ mm is a compromise of the following factors: a sizable atom-cavity coupling strength and technical difficulties in superpolishing and implementing the HR coating on spherical surfaces with small radii of curvature. In particular, by reducing R_C and hence reducing the cavity length to maintain the geo-

metrical requirement of near-concentric ($l_{cav} \sim 2R_C$), we can increase the atom-cavity coupling strength. However, this requires a mirror coating with higher reflectivity to maintain the same cavity linewidth, as the cavity linewidth scales as $\delta\nu \propto l_{cav}/\mathcal{F}$. On the contrary, an increase of R_C alleviates the coating requirement but increases the cavity mode volume and hence the coupling strength is reduced.

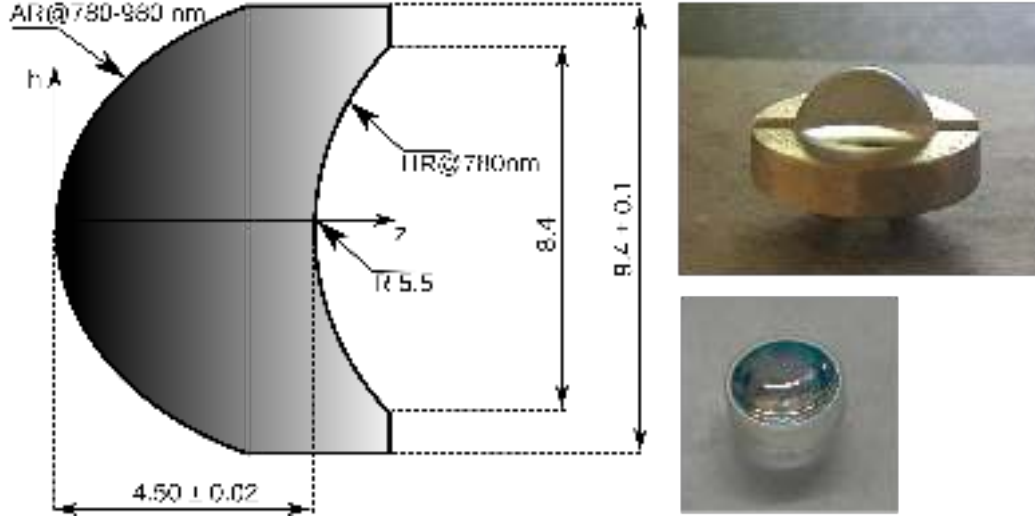


Figure 3-1: Design of the near-concentric cavity mirrors. Left: Schematic drawing of the mirror. The spherical surface with HR coating at 780 nm acts as the cavity mirror. The input surface has an elliptical profile and employed as the mode-matching lens. Top right: Image of the cavity mirror in the shield. Bottom right: Image of the cavity mirror surface.

Previous experiments in cavity QED with short cavity lengths in a range of few hundreds microns employ a standard design of plano-concave cavity mirrors [Raizen et al., 1989, Thompson et al., 1992, Boca et al., 2004]. The cavity lengths are shorter than the Rayleigh range, and hence such cavities have cavity modes that resemble plane waves. The mode-matching lenses used in the experiments with the plano-concave cavity mirrors are located outside of the vacuum chamber and separated from the cavity setup by a thick window. Though there are "problematic" planar surfaces that may introduce aberrations in the mode-matching process, it has been reported that the mode-matching efficiency of coupling light into such cavities does not suffer significantly [Meschede, 2013]. For near-concentric cavities, the cavity mode has a spherical wavefront that extends a large solid angle. Such cavity mode with a large beamwaist and a large spherical wavefront introduces more difficulties to the

cavity mode-matching.

Recently, it has been demonstrated that the planar surface of the plano-concave mirror reduces the mode-matching efficiency of near-concentric cavity significantly [Durrak et al., 2014]. Here, to address this mode-matching problem, we take a different approach to the design of the cavity mirrors. In particular, we replace the planar surface of the cavity mirror’s substrate with an anaclastic surface (see Fig. 3-1). The anaclastic surface acts as a mode-matching lens that transforms the strong focusing cavity mode in the near-concentric regime into a collimated Gaussian mode. The relative offset between optical axes of the coupling lens and the mirrors is critical to the coupling of light in and out of the cavity. In the case of using a separate mode-matching lens, a drift of the lens can change both the transverse position and the beam waist of the input laser at the cavity mirrors, which consequently affects the coupling efficiency. In our approach of combining the mode-matching lens and the cavity mirrors into one substrate, this shifting and the additional effort of alignment of the mode-matching lens are minimized.

3.1.2 Mechanical positioning of the mirrors

Near to concentric point, the cavity modes are sensitive to misalignment in the transverse direction. Therefore, we need to introduce some control elements to the design which is capable of moving one of the cavity mirrors in the transverse directions. Heating elements can be employed to control positions of cavity mirrors via the thermal expansion of the cavity holder. This approach can offer a solution with an adjustment range of hundreds micrometers to even millimeters. However, the thermal control does not provide sub-nanometer resolution and independent movements in three directions. Consequently, actuators such as piezoelectric materials are more viable.

The piezo used in our experiment is a customized piezo (PI P-153.10H). The piezo consists of 72 shear-piezo stacks glued together, which can be grouped into three segments corresponding to three orthogonal travelling directions. In each direction, the piezo is able to move $\pm 5 \mu\text{m}$ with sub-nanometer resolution. In addition, there is another ring piezo which can cover a shorter travelling distance but provides a higher locking bandwidth.

3.1.3 Cavity mount

The cavity mounting system is designed to be compact and fit to a scientific cuvette which can provide convenient optical access to the experiment. Figure. 3-2 shows the schematic of our design. The system essentially consists of: a piezo holder, cavity mirror shields, and a L-shaped block.

As will be shown in section 4.2, the near-concentric cavity is sensitive to the displacement of the cavity mirrors in the transverse direction. This transverse displacement is mainly caused by the temperature change of the cavity mount. We observe that a cavity mount made of aluminium did show a too large dependence on the ambient temperature. Hence, except the cavity mirror shields, all the components are made of titanium to reduce structural changes of the mounting system due to thermal fluctuations.

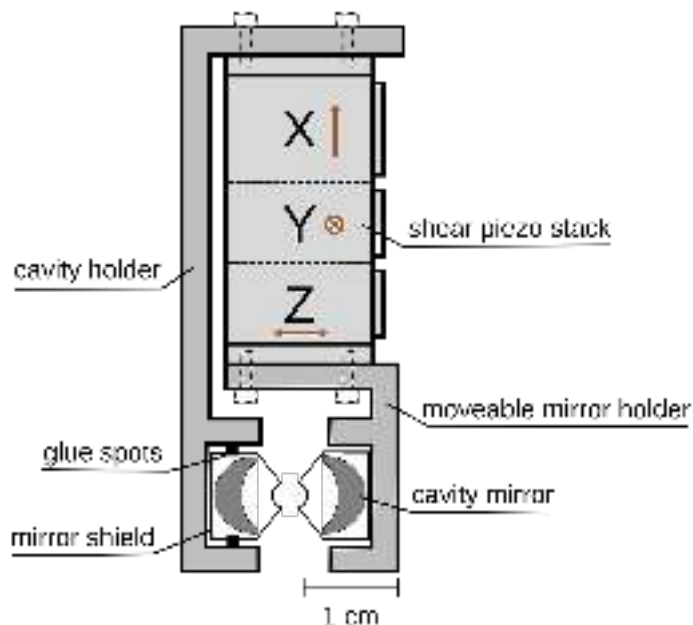


Figure 3-2: An overview of the near-concentric cavity mounting system.

The cavity mirror is placed into a mirror shield made from aluminium and secured with a vacuum-compatible epoxy. The shields provide general protection and prevent the cavity mirrors from being contaminated by atomic beams emitted from a dispenser which is located about 20 cm away from the cavity. The cavity holder is the main body of the cavity mounting system and accommodates the stack piezo. The cavity

holder is machined from a block of Ti6Al4V Grade-5 titanium. The cavity holder has a protruding arm with a spherical opening to hold one of the cavity mirrors. The four columns at the opening provide anchor points to glue the cavity mirror. The other mirror would be mounted inside a similar structure located on the L-shaped block (the movable mirror holder). The diameter of the spherical openings is $\sim 100 \mu\text{m}$ larger than the diameter of the mirror shields. This gap between the shield and the four columns provides space to adjust the mirror's position during the alignment process. A larger gap, though allows for more machining tolerances, but requires a higher amount of glue to apply and hence causes the cavity mirrors to drift more during the curing process.

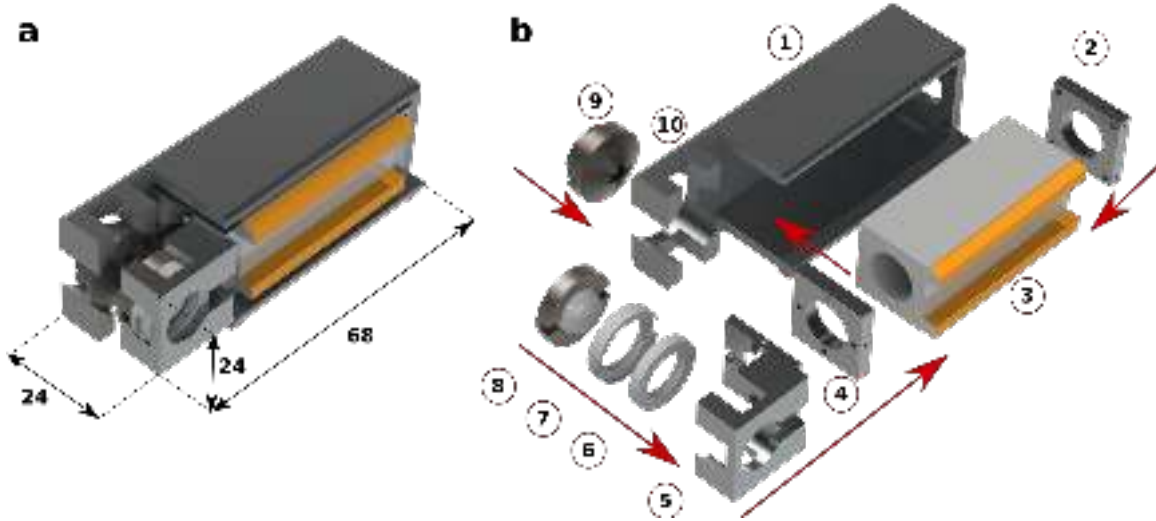


Figure 3-3: Three-dimensional model of the near-concentric cavity system. (a) The completed assembly view with system dimensions in millimeters. (b) The exploded view: 1 Cavity holder. 2 Back plate. 3 Stacked piezo. 4 Front plate. 5 L-shaped block. 6 Ring piezo. 7 PEEK spacer. 8 Right cavity mirror in the shield. 9 Left cavity mirror in the shield. 10 Spherical opening. The yellow bars indicate the piezo electrodes. Arrows show the direction of assembling parts.

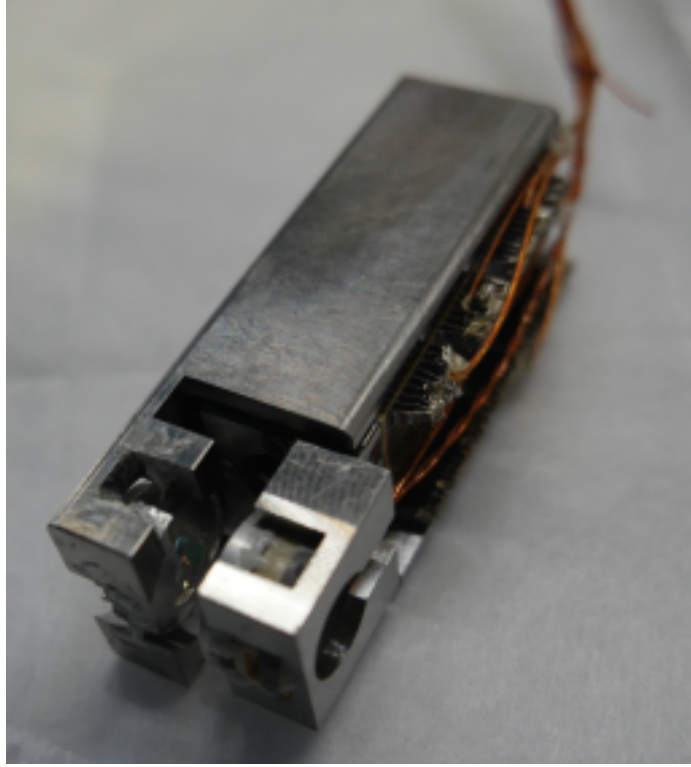


Figure 3-4: Image of an assembled near-concentric cavity.

3.2 Cavity construction

3.2.1 Assembly procedure

The optical axes of the cavity mirrors need to be nearly overlapped within a travelling range of the piezo. Hence, the two spherical opening of the block and the holder, which accommodate the mirrors, must be aligned within $\pm 5 \mu\text{m}$. In the following, we describe a precise pre-alignment procedure to achieve this requirement.

Figure 3-3 shows the basic assembly steps. First, the two ends of the piezo are glued to two thin plates which have four tapped holes at the corners. They provide a non-destructive and convenient way to detach the piezo from the holder. The piezo with two attached metal plates is fixed on the holder by means of four titanium screws. A cylinder that goes through both holes on the piezo and the holder is used as a reference to align the position of the piezo on the holder. The other end of the piezo is attached in a similar way to a L-shaped block, which is the mounting structure for

the cavity mirror and the ring piezo. The adjustment cylinder is withdrawn after the assembling is done.

The ring piezo is electrically isolated from the holder with a PEEK spacer (Polyether ether ketone). The mirror contained in the shield is secured to the spacer. Altogether, they form a stack that is mounted to the L-shaped block. To allow for obstructed movement of the ring piezo, it is advisable to avoid any contacts between the four columns of the block and the stack. The only contact point is between the ground electrode of the ring piezo and the L-shaped block.

3.2.2 Alignment procedure

The relatively large numerical aperture of near-concentric cavity modes and the aspheric outside surface of the cavity mirrors require that the optical axes of the two cavity mirrors coincide – a requirement that is much less critical in conventional cavity arrangements. Additionally, the absolute transverse separation of the mirror surfaces needs to be near the critical distance within the moving range of the piezo translator. In the following, we describe the steps required to align the cavity mirrors and assemble them into the cavity mount. Figure. 3-5 shows the schematics of the alignment setup.

The first step is to have an optical setup of two fiber-couplers (FC1 and FC2) coupled to each other. The laser beam between the two fiber-couplers defines a reference line for the alignment of the cavity mirrors. In other words, the optical axes of two cavity mirrors will be aligned to be coincident with the reference laser beam. This provides a coarse alignment and a finer adjustment is carried out subsequently. The cavity mounting system with one glued cavity mirror is mounted on a xyz precision translation stage (TS) (Thorlabs PT3/M) with a tip-tilt mirror mount (KM100-E02). This arrangement allows us to adjust the mirrors with three degrees of freedom in translation and two rotational degrees of freedom.

The next step is to adjust the cavity mirror such that the laser beam hits the center of the cavity mirror. This can be ensured by checking the symmetry of the reflected beam from the mirror on a camera. The adjustment of the tip-tilt mirror (TM) makes the reflected beam from the cavity mirror back to the fiber coupler.

On the left side, the other mirror, which is denoted as the left mirror, is clamped to

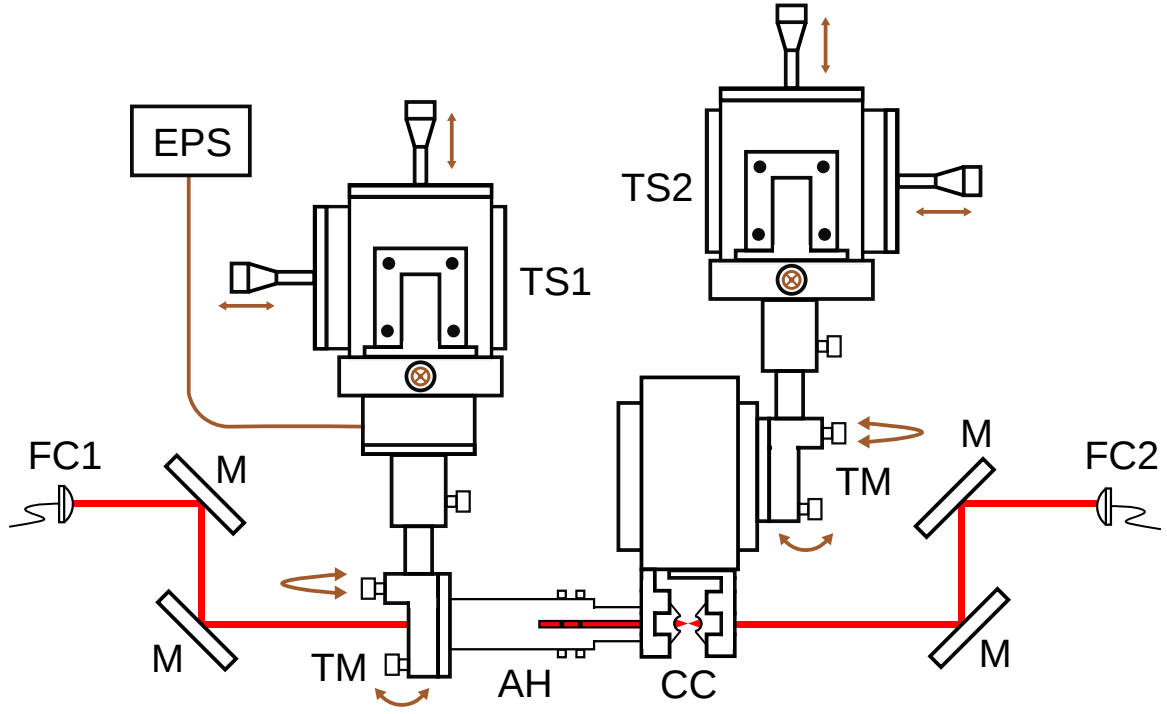


Figure 3-5: Schematic of the cavity alignment setup. Two single-mode fiber couplers (FC) coupled to each other define a reference line for the optical axis of concentric cavity (CC). An auxiliary holder (AH) is placed on the left translation stage (TS1) with an external piezo system (EPS). The cavity mounting system is on the right translation stage (TS2). Rotational degrees of freedom are provided by tip-tilt mounts (TM). M: mirrors.

an auxiliary holder (AH). We employ another translation stage to control the position of the left mirror. The mirror can be released from the holder by untightening the screws on the top of the auxiliary holder after the gluing process. Following the same procedure, the optical axis of the left mirror is aligned with the reference beam. Here, besides the coarse movement of the micrometer, the left mirror can be moved with nanometer-resolution steps provided by an external piezo system (EPS) (Jena Piezo System).

When the two cavity mirrors are well aligned with the reference beam, the left mirror is slowly moved into the holder through the spherical opening of the cavity holder. In order for the left mirror to avoid touching the cavity holder which can alter the alignment, we monitor the electrical continuity between the holders and the mirror shield. In addition, the optical power of the reflected beam into the fiber couplers is ensured to be relatively constant during the transport process. When the cavity mirror is totally inside the holder, fine adjustment of the transverse position is carried out with the external piezo system. We use the cavity transmission as a feedback for the alignment. Note that during the alignment procedure, the alignment of laser beams are maintained fixed, only the positions of two cavity mirrors are adjusted to get the optimized cavity transmission.

When the alignment is completed, vacuum-compatible epoxy (Torrseal) is applied at contacts between the cavity mirror shield and the four columns at the spherical opening of the holder. Torrseal is chosen because of its relatively low shrinkage, ultrahigh vacuum compatibility, and high elasticity modulus. We observe that the curing process can change the volume of glue and hence pushing the cavity mirror out of the alignment. Therefore, it is critical to apply an equal amount of glue at the four corners to cancel the drift during the curing process. We observe that it takes about two hours at room temperature for the Torrseal to be cured and hardened. During the curing process, the position of the cavity mirrors needs to be constantly monitored and adjusted to maintain the cavity alignment. After the mirror's position is secured by the cured Torrseal, the mirror is released from the auxiliary holder, and the holder is withdrawn, leaving the cavity mirrors assembled and aligned inside the cavity holder. The aligned cavity is moved into a glass cuvette with a vacuum system that can reach a pressure of 10^{-9} mbar.

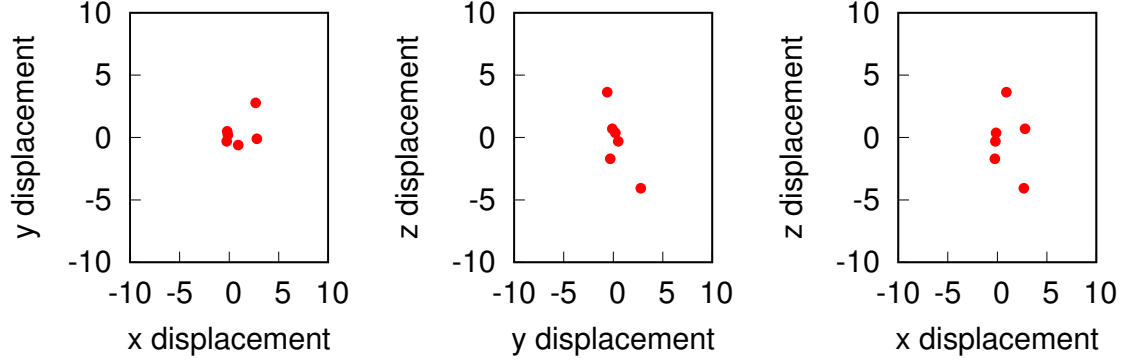


Figure 3-6: Cavity drifting after alignment. Each red dot indicates the drift of one cavity mirror with respect to the other after one attempt of cavity alignment.

3.2.3 Post-alignment drift

After each attempt to align the cavity, we record the drifts of the mirrors in three directions. The statistics of these displacement is shown in Fig 3-6. The average drift is $0.49 \pm 0.65 \mu\text{m}$, $0.21 \pm 0.56 \mu\text{m}$, and $-0.11 \pm 1.17 \mu\text{m}$ for x,y, and z direction respectively. The average total drifting distance is $1.26 \pm 0.9 \mu\text{m}$. We observe that the drift is random in all directions. By careful application of the same amount of glues at four corners, we can minimize the drift to be below the maximum travelling distance of the piezo. However, after the vacuum bake out at around 50°C to 70°C , the drifting of the cavity is more significant and capricious. We attribute the irreversible change in the alignment of the two mirrors to the thermal stress and hysteresis of the structure and glue points.

3.3 Characterization of cavities

A good understanding of cavity and cavity mirrors' properties is essential to predict the cooperativity of the atom-cavity system and to eliminate systematic errors in our experiments. In the following, we will describe and discuss methods of characterizing cavity properties. A summary table of the properties of the cavity is presented at the end of the section.

3.3.1 How near is near to concentric?

In the stable regime, the atom-cavity coupling strength varies insignificantly in relation to the cavity length. However, when operating near to concentric point, one observes a much more sensitive relationship between l_{cav} and g_0 . As a result, the determination of cavity length is important to estimate the atom-cavity coupling strength.

Comparison of methods

There are several methods to determine a cavity length. One of these is to measure the free spectral range of the cavity and deduce the cavity length by using a simple relationship:

$$l_{cav} = c/(2\nu_{fsr}) \quad (3.3.1)$$

where ν_{fsr} is the free spectral range, and c the speed of light in vacuum.

The free spectral range can be measured with a phase-modulated laser coupled to the cavity. The cavity transmission of the phase-modulated laser consists of three peaks: a carrier and two sidebands. The frequency spacing between the carrier and the sideband is denoted as ν_{sb} . When $\nu_{sb} \sim \nu_{fsr}/2$, the sidebands overlap and the transmissions of the sidebands increase. By taking a derivative of l_{cav} with respect to ν_{fsr} , we can approximate the required accuracy of the measurement of ν_{fsr} to determine l_{cav} accurately: $\delta l_{cav}/\delta \nu_{fsr} = c/2\nu_{fsr}^2$. The nominal free spectral range of our 11-mm cavity is $\nu_{fsr} \sim 13.6$ GHz. Substituting this into Eq. 3.3.1, we can determine that, in ideal measurements, an accuracy of 800 kHz in the determination of the cavity free spectral range is required to determine the cavity length with uncertainty below 10 nm. This leads to further technical requirements for the experimental setup: (1) one must be able to generate a frequency marker which is tunable around $\nu_{fsr}/2 = 6.8$ GHz and (2) to overlap the two sidebands with an accuracy of 800 kHz, the cavity linewidth should be as narrow as possible preferably on the same order of the desired accuracy. These requirements are indeed not very severe and can be satisfied. However, this method could not be applied for shorter cavities with free spectral ranges on the order of hundreds of THz, or cavities with broad linewidth such as the near-concentric cavity presented in this thesis.

The second method to measure the cavity length is to compare the frequencies of two laser beams that are simultaneously resonant with the cavity. This method is

convenient for our experiment as to trap atoms and to lock the cavity, we often operate 780-nm and 810-nm lasers on resonance with the cavity. This resonant condition implies that the cavity length must satisfy these equations simultaneously:

$$l_{cav} = n \frac{\lambda_{780}}{2}, \quad (3.3.2a)$$

$$l_{cav} = m \frac{\lambda_{810}}{2}. \quad (3.3.2b)$$

where λ_{780} and λ_{810} are wavelengths of 780 nm and 810 nm laser respectively, m and n are longitudinal mode numbers. As a result, we have the following relationship between the resonant wavelengths of the two lasers:

$$\frac{\lambda_{780}}{\lambda_{810}} = \frac{m}{n}. \quad (3.3.3)$$

The wavelength of the lasers can be determined from a calibrated wavemeter to an accuracy of 10 MHz. Subsequently, m and n can be solved and hence we can determine the cavity length by substituting the mode numbers into Eq. 3.3.2. We note that Eq. 3.3.2 is only valid for plane-wave cavity modes, as it is assumed that the phase shift of the cavity mode is due to only the propagation along the cavity axis. For arbitrary modes with intensity distribution varying along the propagation axis, such as Gaussian beams or higher-order Laguerre-Gaussian modes, Eq. 3.3.2 must be corrected for the additional Gouy phase shift. As explained in the next session, this Gouy phase shift is the same for different longitudinal modes. In contrast, the first method is free from this modification, as it calculates a difference of resonant frequencies between two consecutive longitudinal modes - the free spectral range.

The two methods, though conceptually simple, require a rather complicated setup and changing experimental parameters when measuring different cavity lengths. In particular, in the first method, the generated sideband must be scanned to find the overlapping point. While, in the second method, frequencies of two laser beams must be changed to be resonant with different cavity lengths. More importantly, the above methods can determine only l_{cav} and hence could not provide us with the crucial information about how near to the critical concentric point the cavity length is. In other words, besides the cavity length l_{cav} , we are interested in determining the critical distance $d = 2R_C - l_{cav}$ and the stability parameter $g = 1 - l_{cav}/R_C$,

which are required to estimate the atom-cavity coupling strength g_0 . In fact, if one knows the radii of curvature of the cavity mirrors with an uncertainty less than half of the wavelength, the above techniques are adequate. In other experiments with near-planar cavity mirrors, an accurate determination of R_C is not a concern as a variation of R_C does not affect g_0 significantly. However, for the cavity mirrors in our experiments, which have a relatively small radius of curvature ($R_C = 5.5$ mm), the tolerance in manufacturing is $\pm 0.1\%$ of the nominal value, which is equivalent to ± 5.5 μ m. In the near-concentric regime, such variation of R_C implies an uncertainty of more than an order of magnitude of g_0 .

Transverse mode spacing

As a result of the above analysis, we take a different approach to measure the cavity length and the stability parameter in our experiment. The approach relies on a property of concentric cavities that transverse cavity modes are degenerate in resonant frequencies. Laguerre-Gaussian (LG) functions form a complete basis to solutions of the paraxial wave equation, and thus can be used to describe the eigenmodes of a spherical optical resonator. We denote cavity modes as LG_{nlp} where n, l, p are integer numbers. Modes of different n are known as the longitudinal modes, while the indices (l, p) indicate spatial dependences of the cavity modes on transverse coordinates, hence known as transverse modes. Following the work of Allen in orbital angular momentum of light [Allen et al., 1992], we can write down the mode functions of LG_{nlp} as

$$u(r, \phi, z) = \frac{C_{lp}}{w(z)} \left(\frac{r\sqrt{2}}{w(z)} \right)^{|l|} \exp\left(-\frac{r^2}{w^2(z)}\right) L_p^{|l|}\left(\frac{2r^2}{w^2(z)}\right) \exp\left(-ik\frac{r^2}{2R(z)}\right) \exp(-ikz) \exp(-il\phi) \exp(i\psi(z)), \quad (3.3.4)$$

where C_{lp} is the normalization factor, $R(z)$ the radius of curvature, $w(z)$ beam width at position z , k wave vector, $L_p^{|l|}$ generalized Laguerre polynomials, and $\psi(z) = (|l| + 2p + 1) \tan^{-1}(z/z_0)$ the Gouy phase.

Equation 3.3.4 can be separated into two parts: the last four terms represents the total phase of the field, while the remaining terms depict the amplitude distribution. We can confine our attention to the total phase of the field at the optical axis ($r = 0$)

$$\Phi = -kz - l\phi + \psi(z). \quad (3.3.5)$$

The total phase shift of the cavity modes after one round trip in the cavity is then given by

$$\Delta\Phi = -2kl_{cav} + 2\psi(l_{cav}/2z_0) . \quad (3.3.6)$$

The resonant frequencies of the cavity modes are determined by the condition that the round-trip phase shift in the cavity must be an integer multiple of 2π

$$-2kl_{cav} + (|l| + 2p + 1) \tan^{-1}(z/z_0) = n2\pi. \quad (3.3.7)$$

By substituting $k = 2\pi\nu/c$ into Eq. 3.3.7 and rearranging the terms, we can obtain an expression for the resonant frequencies of the cavity with identical spherical mirrors and under paraxial approximation

$$\nu_{n,l,p} = n \frac{c}{2l_{cav}} + (1 + |l| + 2p) \frac{c}{2l_{cav}} \frac{\Delta\psi}{\pi}, \quad (3.3.8)$$

where c is the speed of light, $\Delta\psi = 2 \tan^{-1}(l_{cav}/2z_0)$ is the Gouy phase shift of LG₀₀ for a round trip in the cavity length, and z_0 is the Rayleigh range of the cavity [Saleh and Teich, 2001]. From this, we derive the expression for the frequency spacing of LG₀₀ and LG₁₀ in terms of l_{cav} and R_C :

$$\Delta\nu_{tr} = \nu_{00} - \nu_{10} = \frac{c}{2l_{cav}} \left(1 - \frac{\cos^{-1}g}{\pi} \right), \quad (3.3.9)$$

where $g = 1 - l_{cav}/R_C$ the stability parameter. As the cavity length approaches critical length, the shift of the transverse mode frequencies approach one unit of the free spectral range. Therefore all transverse modes are co-resonant for concentric cavities.

To determine $\Delta\nu_{trans}$ from the cavity transmission spectrum, we detune the cavity length within a free spectral range by applying a sawtooth voltage to the z-segment of the stacked piezo, which controls the cavity length. We record the spectrum at multiple resonant cavity lengths and use a peak-detection algorithm to determine the resonance frequencies. Monitoring the intensity distribution of the light transmitted through the cavity on a linear camera helps us to distinguish different transverse modes.

To obtain a frequency marker, we modulate the probe laser by using an electro-

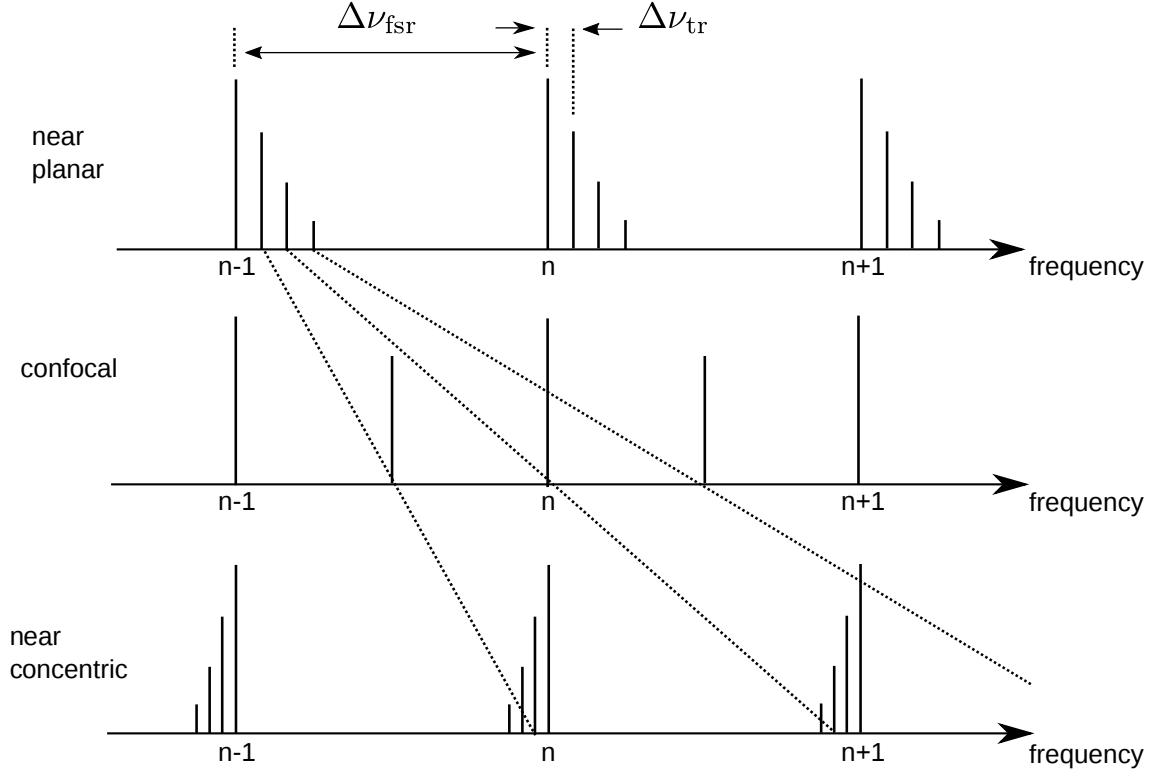


Figure 3-7: Transverse mode frequencies in various geometrical configurations of optical cavities. The longitudinal mode spacing (or the free spectral range) is denoted as $\Delta\nu_{\text{fsr}}$. The transverse mode spacing is denoted as $\Delta\nu_{\text{tr}}$.

optical phase modulator (EOM). The two sidebands emerged in the cavity transmission are used as a frequency reference for the peak-detection algorithm. Fig. 3-8 shows the transverse mode frequency spacing at different cavity lengths which are resonant with the 780-nm laser. From a fit of Eq. 3.3.9 to experimental data, we determine $d = 207(13)$ nm at the last stable resonance, which corresponds to the stability parameter $g = -0.99996(2)$. This is consistent with our observation that when increasing the cavity length by another half wavelength, the cavity enters the unstable regime and exhibits lossy modes (see Fig. 3-9 and the next section).

The good agreement between the experimental data, including the last resonant point before critical length, and the fit based on the paraxial equation prompts us to discuss about the validity of the paraxial approximation in our near-concentric cavity. The amplitude of the electric field distribution that propagates in the z direction can be described as $E(x, y, z) = u(x, y, z)e^{-ikz}$, where k is the wave vector. To be valid for

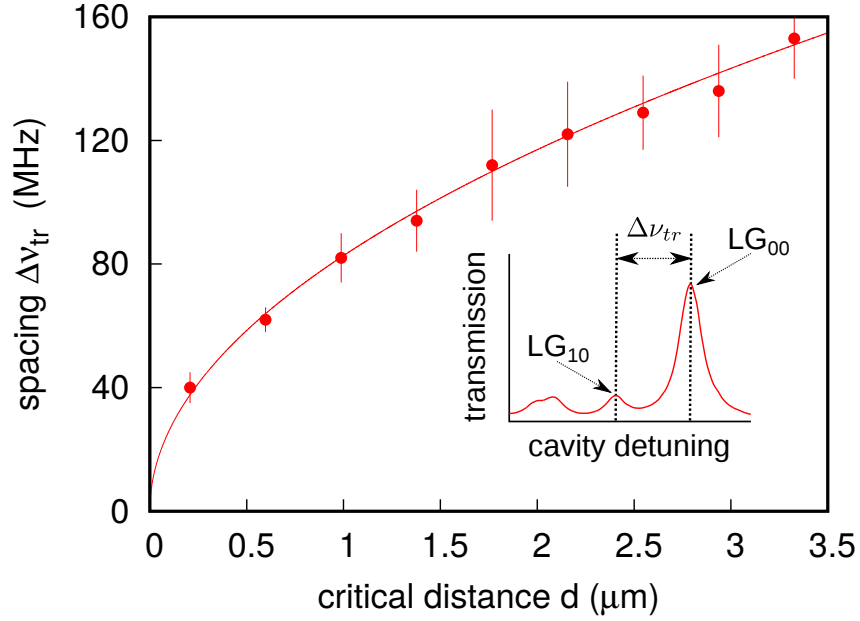


Figure 3-8: Transverse mode frequency spacing at different cavity lengths that are resonant with a 780-nm laser. Solid line are theoretical fit based on Eq. 3.3.9. Error bars show the standard deviation of the measurement.

paraxial approximation, it requires that

$$\left| \frac{\partial^2 u}{\partial^2 z} \right| \ll \left| 2k \frac{\partial u}{\partial z} \right|. \quad (3.3.10)$$

Conventionally, Equation. 3.3.10 is considered valid for optical beam components with an angle with the optical axis up to ≈ 30 degrees [Siegman, 1986]. Transverse fundamental near-concentric cavity modes (LG_{n00}) have a beam divergence of $\theta = \lambda/\pi w_0$, where λ is the wavelength of the resonant mode taken to be 780 nm, and w_0 is the cavity beam waist. Taking the beam divergence now as a characteristic angle with the optical axis, the validity limit of 30 degrees for the paraxial approximation corresponds to $w_0 \geq 496$ nm, or equivalently $d \geq 0.5$ nm. As a result, the paraxial approximation is still valid to describe the modes in our near-concentric cavity. We also note that the definition of the critical distance d and validity of Eq. 3.3.9 are based on a meaningful definition of a mirror surface position. The thickness of the dielectric Bragg stacks forming the mirrors for our cavity exceed by far the critical distances d for the last stable longitudinal resonances, so the absolute position of the

mirror surface has to refer to an effective position of these Bragg stacks.

3.3.2 Cavity mode analysis

Beside the sensitivity to misalignment, another factor that hinders the feasibility of using near-concentric cavities is the reduction of the linewidth and transmission. Previous observations indicated that the cavity finesse reduces significantly as the cavity is pushed toward the geometrical instability [Haase et al., 2006]. In contrast to this, possibly due to refined manufacturing techniques of large angle spherical surfaces, we demonstrate in this section that our near-concentric cavity can maintain the transmission and linewidth at the last two resonant cavity lengths before the unstable regime.

An optical resonator can be viewed as a system that can store electromagnetic energy. The lifetime of stored energy (or a photon) in the cavity determines its linewidth. The possible decay channels are the coupling to an external mode or the scattering and absorption losses of the cavity mirrors. In the context of cavity QED, the dissipation should be minimized to achieve the strong coupling regime. The cavity losses are also important in practice as they determine an insertion loss of the atom-cavity system employed as a node in a quantum network. While the cavity linewidth depends on the reflectivity of the cavity mirrors and the cavity length, the transmission is a function of both the cavity losses and the mode matching of a probe field to the cavity mode. The reduction of cavity transmission and the cavity photon lifetime in near-unstable cavities can be attributed to the mode-matching and misalignment losses. Ineffective mode-matching excites multiple transverse cavity modes. In the near-concentric regime, where all the transverse mode are co-resonant, the excitation of multiple cavity modes broadens the linewidth and reduces the coupling into the fundamental modes. In addition, as explained in the next section, any tilting between two cavity mirrors introduces a diffraction loss in the cavity. The undesired effects can be alleviated by employing the aspheric mode-matching surface and the careful alignment procedure described in section. 3.2.

A ringdown measurement is usually employed to determine the cavity linewidth [Rosenfeld, 2003]. The ringdown technique basically is a time-domain method that tracks the cavity field decay rate when the pumping light is suddenly switched off.

This requires a setup that is capable of switching off the laser faster than the estimated photon lifetime in the cavity, which is on the order of 20 ns for our cavity. Here, we characterize the cavity properties by measuring the cavity transmission spectrum. This method requires the probe laser linewidth to be much narrower than the cavity linewidth, which is technically more difficult with high finesse cavities. However, it especially suits to our cavity specifications with an expected cavity linewidth of around 30 MHz.

We use a diode laser operating at a wavelength of 780 nm to probe the cavity. This is the wavelength of the D₂ transition of ⁸⁷Rb, which is our target transition of the atom-cavity coupling. The laser linewidth is about 1 MHz. The cavity transmission is recorded as the cavity length is detuned across the resonant frequency of the probe laser. To obtain a frequency reference, we modulate the phase of the probe laser with an electro-optical modulator (EOM), driven by a RF signal generator (WindFreak, SynthUSBII 34MHz - 4.4GHz). The optical side-bands act as frequency markers to convert the piezo's voltage to units of frequency. Typical cavity transmission spectra are shown in Fig. 3-9. The transmission of two cavity modes (LG₀₀ and LG₁₀) can be modelled by a summation of two Lorentzian functions:

$$T(\nu) = \frac{T_1}{4(\nu - \nu_1)^2/\delta\nu_1^2 + 1} + \frac{T_2}{4(\nu - \nu_2)^2/\delta\nu_2^2 + 1}, \quad (3.3.11)$$

where $T_{1(2)}$ are transmission coefficients, $\nu_{1(2)}$ are resonant frequencies, and $\delta\nu_{1(2)}$ are linewidths of the cavity modes LG₀₀ and LG₁₀, respectively. We can determine the cavity linewidths and transmission by fitting Eq. 3.3.11 to the data. We acknowledge that the accuracy of the linewidth measurement relies on the linearity of the piezo scan. As a result, the frequency for the phase modulation must be similar to the expected linewidth of the cavity, which is chosen to be 50 MHz in our experiment.

At $d = 207$ nm, we observe that the cavity fundamental mode maintains the similar cavity linewidth and transmissions. In particular, the linewidth of the fundamental mode LG₀₀ measures 22.43(5) MHz which agrees with the nominal value of 21.7 MHz, determined from the cavity mirror's design reflectivity of 99.5% at 780 nm. At this length, the cavity transmission is 37%. However, at the last resonant length, as the transverse modes start to overlap and the probe laser simultaneously couples to multiple higher-order modes, the second cavity mode becomes difficult to identify, and has

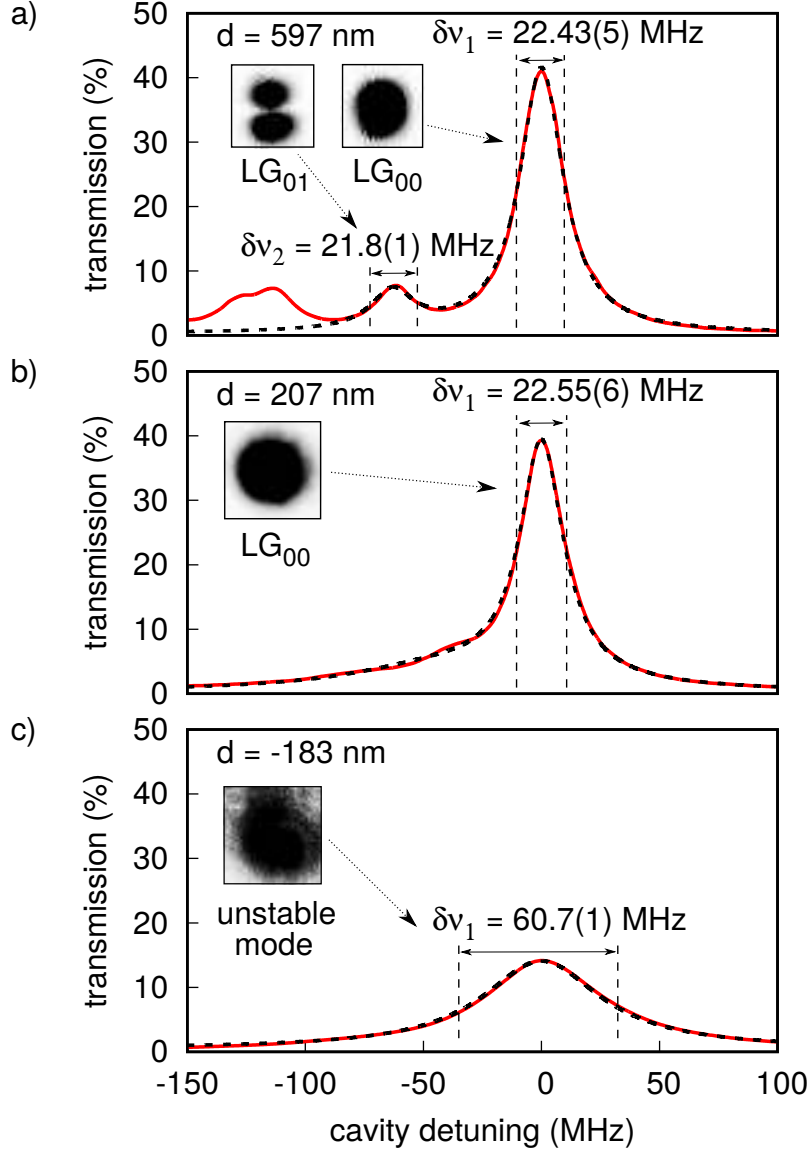


Figure 3-9: Cavity transmission spectra measured by detuning the cavity length. (a) $d = 597$ nm. The dashed line is the fit based on a summation of two Lorentzian functions, corresponding to two resonant peaks. (b) $d = 207$ nm. Transverse modes become degenerate and form a long tail extending out to the lower frequencies. (c) $d = -183$ nm. The cavity is in the unstable regime. The insets show the transverse mode profiles.

a broadened effective linewidth, which is determined from the fit to be $98(2)$ MHz. When increasing the cavity length by another half wavelength ($d = -183$ nm), we observe a sudden decrease in the cavity transmission and a sudden increase in the cavity

linewidth, which are indicative of unstable cavity modes. Moreover, the transverse profile of the cavity mode deviates from a Gaussian profile.

3.3.3 Cavity losses

The intra-cavity photon can escape the cavity via two independent processes: transmitting through the cavity mirrors and being absorbed or scattered by defects on the mirror coating. Both processes contribute to the cavity decay rate. However, there is a fundamental difference. The transmitted photons are coherently coupled to a well-defined output mode and can be detected on photodetectors. In contrast, scattering is a dissipative process and should be considered as an irreversible loss in the cavity. In almost all applications of optical resonators, cavity losses should be minimized as information about the system gets lost to undetectable channels. Knowing the cavity linewidth alone is also not enough to quantify the rate of each process independently. Characterization of the cavity losses is therefore essential as the only property of the cavity mirrors provided by the manufacturer is the reflectivity of 99.5 %; no information on the losses and transmission is provided.

In this section, we analyze the two types of losses of the near-concentric cavities: (1) losses due to the imperfection of the mirror's HR coating and (2) the diffraction loss due to the misalignment between two optical axes of the two cavity mirrors.

Mirror losses

Optical properties of cavity mirrors can be described by three parameters: the coefficients of reflectivity R , transmission T , and loss A . The principle of energy conservation requires $T + A + R = 1$. The loss coefficient includes absorption and scattering losses. One approach to experimentally determine these coefficients is to measure the transmission and reflection of an incident laser beam on the cavity mirrors. In the case of high finesse cavity mirrors, the reflectivity of the mirror is extremely high with a typical value of transmission and loss on the order of ppm. Therefore, though being direct and simple to set up, the above measurement is experimentally not feasible with high finesse cavity mirrors, and as shown below, also not suitable for our cavity mirrors with small radii of curvature.

As a result, we employ an alternative method described in [\[Hood et al., 2001\]](#).

The method requires that a cavity must be formed by the two mirrors that need to be characterized. Subsequently the three coefficients that characterize the optical properties of the mirrors can be determined from the resonant transmission P_t , the resonant reflection P_r and the finesse \mathcal{F} of the cavity.

We begin with the derivation of formulas used in [Hood et al., 2001] and specify the assumptions of the derivation. On resonance, for a monochromatic light with input power P_{in} incident on an optical cavity, the transmitted and reflected power are given by

$$P_t = \frac{T^2 (1 - A)}{[1 - R(1 - A)]^2} P_{in} , \quad (3.3.12)$$

$$P_r = \frac{RA}{[1 - R(1 - A)]^2} P_{in} . \quad (3.3.13)$$

Here, the mirrors are assumed to have the same optical properties, meaning that $R_1 = R_2 = R$, and $T_1 = T_2 = T$. This is a reasonable assumption as all of the mirrors coating are produced in the same coating run. Further steps are taken with the assumption that the reflectivity of the mirrors is close to unity and the cavity mirror loss is small but not negligible, meaning that with $R \approx 1$ we have the relations

$$P_t = \frac{T^2}{(T + A)^2} P_{in}, \quad (3.3.14)$$

$$P_r = \frac{A^2}{(T + A)^2} P_{in}. \quad (3.3.15)$$

With this assumption, the cavity finesse can be approximated by

$$\mathcal{F} = \frac{\pi}{A + T}. \quad (3.3.16)$$

In experiments, it is necessary to take into account the fact that not all optical power of the incident resonant light can be coupled to the cavity. This is taken into account by introducing the mode-matching factor η , so that $(1 - \eta) P_{in}$ is the optical power rejected by the cavity and reflected directly off the input cavity mirror. Then, ηP_{in} can be considered as effective incident input optical power. Equations 3.3.14 and

3.3.15 must be modified as following

$$\frac{P_t}{\eta P_{in}} = T^2 \left(\frac{\mathcal{F}}{\pi} \right)^2, \quad (3.3.17)$$

$$\frac{P_r - (1 - \eta) P_{in}}{\eta P_{in}} = A^2 \left(\frac{\mathcal{F}}{\pi} \right)^2. \quad (3.3.18)$$

To eliminate η from the equations, we divide Eq. 3.3.18 by Eq. 3.3.17. This gives us an expression for the effective cavity transmission α

$$\alpha = \frac{P_t}{P_{in} - P_r} = \frac{T^2 \left(\frac{\mathcal{F}}{\pi} \right)^2}{A^2 \left(\frac{\mathcal{F}}{\pi} \right)^2 - 1}. \quad (3.3.19)$$

Combining with Eq. 3.3.18, we can determine T , R , A and η from experimentally accessible quantities:

$$T = \frac{2\alpha}{1 + \alpha} \frac{\pi}{\mathcal{F}}, \quad (3.3.20)$$

$$A = \frac{1 - \alpha}{1 + \alpha} \frac{\pi}{\mathcal{F}}, \quad (3.3.21)$$

$$R = 1 - A - T, \quad (3.3.22)$$

$$\eta = \frac{P_t}{P_{in}} \frac{(T + A)^2}{T^2}. \quad (3.3.23)$$

We determine P_{in} , P_t , and P_r with a calibrated photodetector. The cavity finesse was obtained according to the method described in Sec. 3.3.2. All additional losses due to other optical elements such as the glass cuvette are taken into account. Operating the cavity at $d = 207$ nm, for an optical input power of $P_{in} = 2.430(1)$ mW, we measure $P_t = 1.010(1)$ mW, and $P_r = 1.332(1)$ mW. From these values, we find $A = 0.0217(4)\%$, $T = 0.4990(4)\%$, and $R = 99.48\%$.

Misalignment losses

Besides the scattering and absorption loss, the cavity can exhibit additional diffraction losses due to the finite aperture of the mirrors if there is a misalignment between the two optical axes of the cavity mirrors. The misalignment causes a shift of the cavity intensity profile on the mirror. This diffraction loss due to misalignment becomes

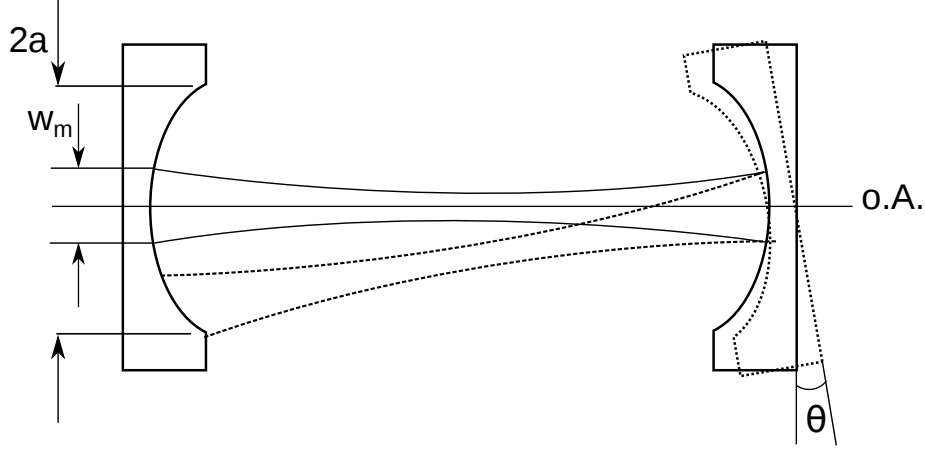


Figure 3-10: Tilting misalignment of spherical optical cavities. A tilt of one of the cavity mirrors about the optical axis (o.A.) by θ induces additional diffraction loss per round trip. The total diffraction loss is a function of stability parameter g , the mode beam waist on mirror w_m , and the radius of mirror aperture a .

more critical for near-unstable cavities as the beam waist at the cavity mirror is large. Hence, it is important to assess the degree of misalignment in our cavity. Here, we assume that the misalignment is entirely due to the tilting of the mirrors, as one of the mirrors can be translated by the piezo. With that assumption, the misalignment loss per round trip is given by [Hauck et al., 1980]

$$\alpha = \theta^2 \frac{1 + g^2}{(1 - g^2)^{3/2}} \frac{\pi l_{cav}}{\lambda} \frac{(a/w_m)^2}{\exp[2(a/w_m)^2] - 1}, \quad (3.3.24)$$

where θ is the misalignment angle, a is the radius of cavity mirror's aperture, and w_m is the beam waist at the mirrors (see Fig. 3-10). From the observation that the cavity linewidth is comparable to the nominal value and assuming that all the cavity losses is due to the tilting misalignment, we can estimate the tilting angle between the two cavity mirrors to be better than 0.5 degrees ($\theta \leq 0.5 \text{ deg}$) in the near-concentric regime. This estimation agrees with what can be guaranteed in the alignment procedure described in section 3.2.2, as the reflected laser beams from the cavity mirrors are ensured to couple back to the fiber couplers. Table 3.1 summarizes the optical properties of the near-concentric cavities.

Table 3.1: Cavity parameters at the last few stable resonances.

$d = 2R_C - l_{cav}$	597 nm	207 nm	-183 nm
Transmission T_1 (%)	41.13(5)	37.06(6)	13.60(1)
Linewidth $\delta\nu_1$ (MHz)	22.43(5)	22.55(6)	60.7(1)
Stability parameter g	-0.998903(2)	-0.999962(2)	-1.000033(2)
Tranverse mode spacing $\delta\nu_{tr}$ (MHz)	62(4)	40(5)	NA
Cavity waist $w_0(\mu\text{m})$	3.17	2.44	NA
Coupling strength g_0 (MHz)	$2\pi \times 15.46$	$2\pi \times 20.15$	NA
Cooperativity C	3.62	6.15	NA

3.4 Contamination of cavity mirrors

The reported cavity properties in Table 3.1 were characterized in air. After the alignment process, we place the cavity setup in a vacuum chamber and perform a bake-out at a temperature of 70°C measured at the glass cuvette for two weeks. The cavity properties remain similar to the values obtained in air. However, after operating the dispenser at a high current of 3.5 A for aligning the MOT, we observed a degradation of the cavity mirrors reducing the cavity finesse from 600 to 136 at 780 nm wavelength. This corresponds to an increase of the cavity linewidth from 22 to 100 MHz. In addition, the cavity transmission decreases to 4.6(2)%. Using the technique described in Section 3.3.3, we determine the round-trip loss of the cavity to be 3.6%. However, we do not observe any significant reduction of the cavity coupling efficiency.

Several attempts have been carried out to recover the cavity finesse in the vacuum chamber. Attributing this degradation to the contamination of mirrors by rubidium atoms, we focus a cw 450 nm laser beam with an optical power of 20 mW at the cavity

mirrors. It has been reported that strong UV-light can remove rubidium atoms from the stainless steel surface of the inner vacuum chamber [Torralbo-Campo et al., 2015]. However, we do not observe any improvement after operating the 450-nm laser in 48 hours. Pulsed UV lasers with higher delivered optical energy may be required to break chemical bonds between the adsorbate and the mirror coating. However, the optical energy impinged on the mirror coatings should not exceed the laser damage threshold for our HR-coating, which is provided by the manufacturer to be 12 J/cm^2 with a pulse duration of 6 ns, a duty cycle of 100 Hz and at the wavelength of 532 nm. We do not observe any improvement with powerful LEDs at 430 nm wavelength and heat lamps with a broad emission spectrum. On the other hand, outside the vacuum chamber, we are able to clean the cavity mirrors by soaking them in distilled water at a temperature of 70° . The cavity transmission recovers from 1% to 7%.

3.5 Upgrading the design

A severe limitation of the current design is the limited travel range of the stacked piezo. In the new design of the cavity system, we replace it with a piezo scanner (Attocube ANSxyz100). The new piezo scanner is able to move $50 \mu\text{m}$ in x and z directions, and $24 \mu\text{m}$ in y direction. The cavity mount was redesigned to accommodate the scanner. The new mount consists of only two parts: a cavity mount and a mirror mount. The scanner is stationed on a solid base plate of the cavity mount. Due to the space constraints, the mirror is not mounted on the top of the scanner. Instead, the mirror mount sits on the top plate of the scanner with a spherical opening to accommodate the mirror. To increase the stability, we add a rib to the mirror mount. In addition, we place the ring piezo on the cavity mount. This is to avoid the potential cross-talk between the movement of the piezo and the piezo scanner during dual-piezo locking process.

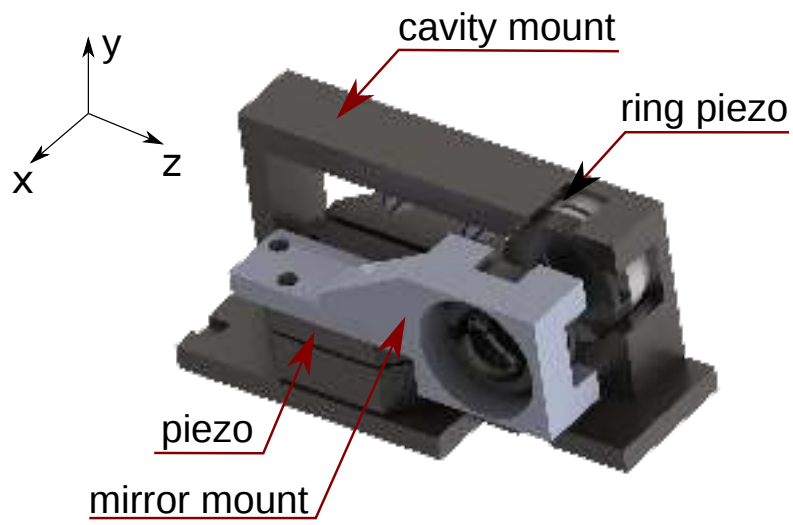


Figure 3-11: Assembly of the cavity system with the Attocube piezo scanner (AN-Sxyz100).

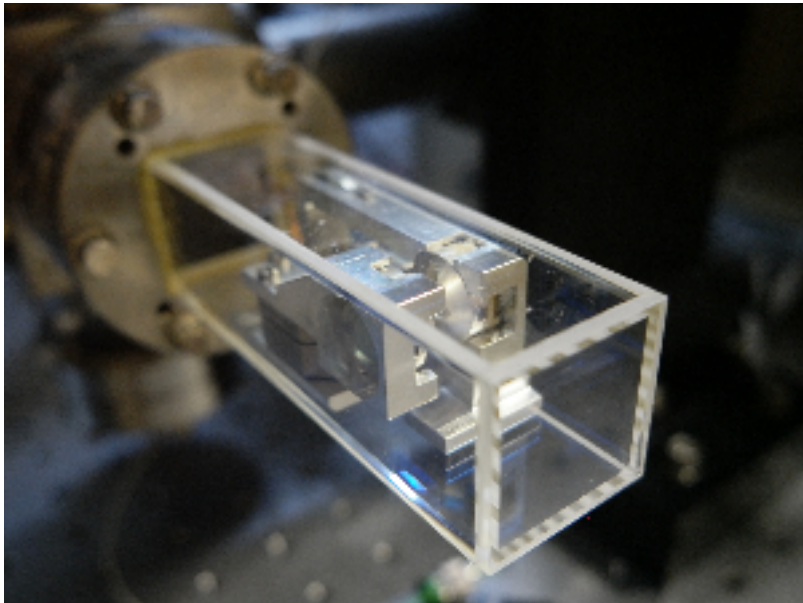


Figure 3-12: Image of an assembled cavity with the Attocube piezo scanner.

Chapter 4

Taming a near-concentric cavity

In the context of cavity QED experiments which focus on the near-resonant atom-light interaction, the cavity length must be tuned such that the cavity resonant frequency and the atomic transition are nearly overlapped, preferably within the three parameters that characterize the atom-cavity system: the cavity linewidth (κ), the atomic decay rate (γ), and the coupling strength (g_0). In practice, unwanted disturbances such as mechanical vibrations or temperature changes cause the cavity length to fluctuate or drift away from its resonance. A displacement of δl_{cav} of the cavity length causes a shift of cavity resonance by

$$\delta\nu = F\Delta\nu\frac{\delta l_{cav}}{\lambda/2}, \quad (4.0.1)$$

where F is the cavity finesse, λ is the laser wavelength that is resonant with the cavity, and $\Delta\nu$ is the cavity linewidth. In order to have the cavity resonance stabilized within 10% of the cavity linewidth ($\delta\nu \approx 0.1\Delta\nu$), the fluctuation of the cavity length has to be less than

$$\delta l_{cav} = \frac{1}{10} \frac{\lambda}{2F}. \quad (4.0.2)$$

For our cavity parameters, $F = 610$ and $\lambda = 780$ nm, and hence $\delta l_{cav} = 60$ pm, which is approximately the mean radius of a ground state electron orbit in hydrogen atoms (the Bohr radius). Such degree of stabilization is typically challenging for passive stabilization elements such as damped springs or vibration isolators. This leads to the need for continuous stabilization of the cavity length, which is the main topic of

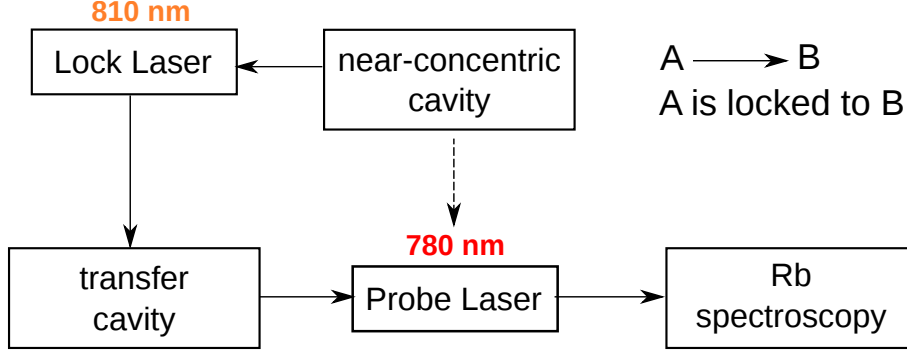


Figure 4-1: Schematic of the near-concentric cavity locking chain. The strategy is to have the near-concentric cavities indirectly locked to the 780-nm laser, indicated by the dashed arrow, via intermediate nodes: the 810-nm laser and the transfer cavity.

this chapter.

The effect of misalignment in transverse direction is often negligible in nearly flat cavities that are used in most other cavity QED experiments [Raizen et al., 1989, Thompson et al., 1992, Boca et al., 2004]. On the contrary, we observe that even with the cavity length stabilized, the cavity resonant transmission of the near-concentric cavity exhibits a long-term drift on the time scale of minutes to hours. We attribute this drift mainly to thermal expansion in the transverse direction of the cavity mount. Therefore, we developed an algorithm to stabilize the transverse alignment of the cavity. With a combination of temperature stabilization and the active transverse algorithm, the near-concentric cavity remains aligned over a few hours. This is an important step for the observation of atom-cavity coupling presented in the next chapters.

4.1 Longitudinal stabilization

Our goal is to stabilize the resonance of the near-concentric cavity to the atomic transition $5S_{1/2}, F=2 \rightarrow 5P_{3/2}, F=3$ of ^{87}Rb atoms at 780 nm wavelength. To avoid the resonant scattering of the atoms trapped in the cavity mode, we do not lock the near-concentric cavity directly to a 780 nm laser. Instead, we stabilize the near-concentric cavity with the help of intermediate locking nodes (see Fig. 4-1).

The locking chain consists of three locking nodes: the near-concentric cavity lock,

the transfer cavity lock, and the lock of the 780 nm laser. As the 780 nm laser is resonant with the atomic transition, we refer to it as the resonant laser. The chain starts with stabilizing the resonant laser to the D2 transition of ^{87}Rb , $\omega_{\text{res}} = \omega_a$. The resonant laser provides concurrently cooling light for the magneto-optical trap (MOT),

The resonant frequency of the near-concentric cavity ω_c is stabilized to the frequency of a lock laser ω_l :

$$\omega_c = \omega_l + n_1\nu_c, \quad (4.1.1)$$

where n_1 is the longitudinal mode number, and ν_c is the free spectral range of the near-concentric cavity. The lock laser also serves as an intra-cavity dipole trap to capture single atoms. As will be explained in section 5.2, to reduce the scattering rate, the lock/trap laser frequency is set to be far detuned with respect to the atomic transition. We choose the wavelength to be 810 nm, which by design lies in the region of the high reflectivity of the cavity mirrors.

Due to the absence of accessible atomic frequency standards near to 810 nm, we set up a transfer cavity to pass the stability from the resonant laser to the lock laser. The lock laser is stabilized to the transfer cavity which is locked to the resonant laser,

$$\omega_l = \omega_{tr} + n_2\nu_{tr}, \quad (4.1.2)$$

$$\omega_{tr} = \omega_{780} + n_3\nu_{tr}, \quad (4.1.3)$$

where n_2 and n_3 are the mode numbers, ω_{tr} is the resonant frequency of the transfer cavity, and ν_{tr} is the free spectral range of the transfer cavity. The resonant frequency of the cavity is then locked to

$$\omega_c = \omega_a + (n_3 + n_2)\nu_{tr} + n_1\nu_c, \quad (4.1.4)$$

As the free spectral ranges of the two cavities are different ($\nu_{tr} \neq \nu_c$), the resonant frequency of the stabilized near-concentric cavity would have an offset from the atomic frequency. To compensate for this offset, we introduce a difference in frequencies ($\Delta\nu_l$) between the two lock laser beams that couple to the two cavities. By setting $\Delta\nu_l = m\nu_c - (n_3 + n_2)\nu_{tr}$, the near-concentric cavity can be set to be resonant with

the atoms

$$\omega_c = \omega_a + (m + n_1)\nu_c. \quad (4.1.5)$$

In practice, we determine $\Delta\nu_l$ by overlapping the resonant peaks of the resonant laser and the lock laser on the transmission of the near-concentric cavity.

4.1.1 Optical setup

Transfer cavity

The transfer cavity has a finesse of 6200, inferred from the reflectivity 99.94% of the mirrors. The two cavity mirrors are separated by an Invar spacer. The distance between the mirrors is 1.1 cm corresponding to a free spectral range $\nu_{tr} = 12.8$ GHz and a linewidth of 2.8 MHz. To minimize the frequency drift, we place the transfer cavity in a compact vacuum chamber (5×10^{-6} mbar) and stabilize the temperature using heating tapes. This can reduce the temperature fluctuation down to about 100 mK corresponding to a fluctuation of 42 MHz of the transfer cavity resonant frequency, which is about two times of the near-concentric cavity linewidth. To further improve the stability, we stabilize the transfer cavity length by controlling a piezo attached to one of the mirrors.

Lock laser

The lock laser is an external cavity diode laser (ECDL) with a grating in the Littrow configuration. The center wavelength of the free-running diode emission is 808 nm. By adjusting the diffraction grating, the diode can reliably operate at 810 nm. After the grating and optical isolators, the optical power is approximately 20 mW. This laser power is distributed to two paths for the two cavities. A frequency difference ($\Delta\nu_l$) between two paths is generated by sending one of the paths to a fiber-based electro-optic phase modulator (EOM) to generate frequency sidebands. We refer to this path as the modulated path.

One approach to implement the locking chain is to couple the modulated beam to the near-concentric cavity. The frequency of the near-concentric cavity is stabilized to one of the sidebands, and the lock laser is stabilized to the transfer cavity via the

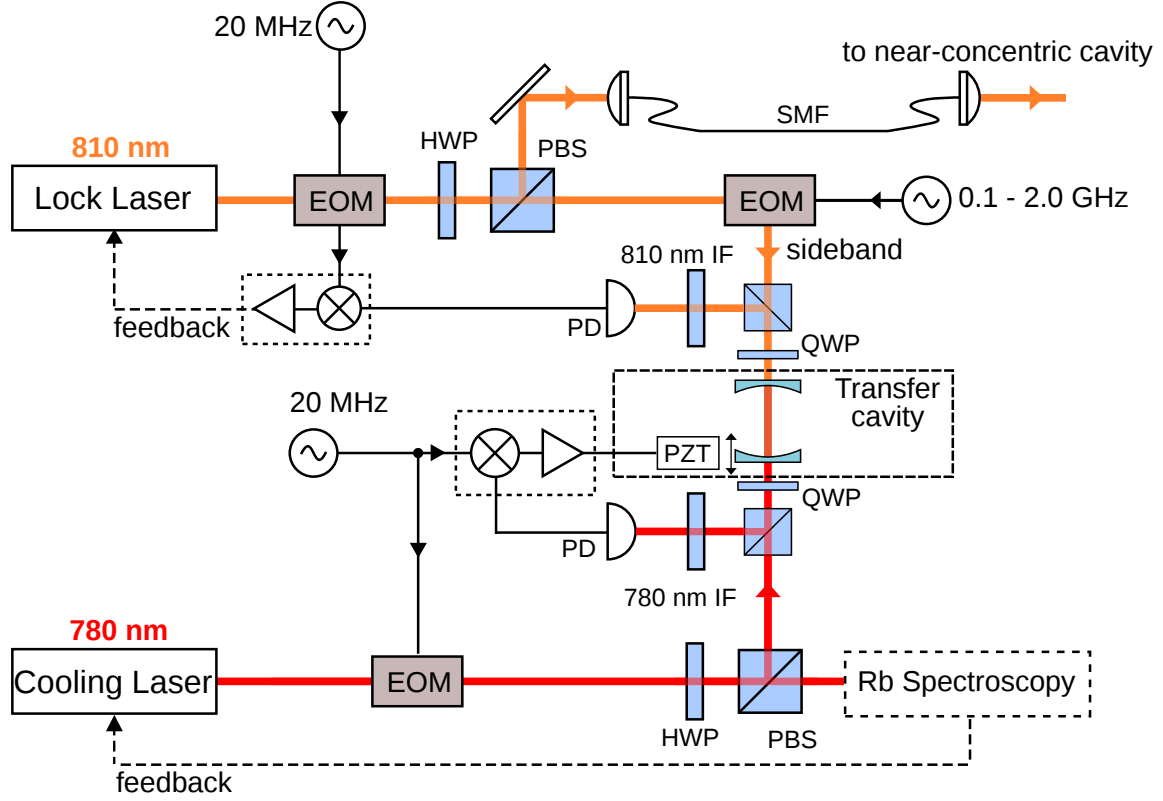


Figure 4-2: Optical locking scheme of transfer cavity and the 810-nm lock laser. Red and orange lines indicate beams from 780-nm laser and 810-nm lock laser, respectively. The 780-nm laser serves as the cooling laser for atom trapping. The frequency of the 780-nm laser is stabilized to a D2 transition of ^{87}Rb . The lock laser's sideband is stabilized to a resonance of the transfer cavity, which in turn is stabilized to the 780-nm laser. The frequency of the lock laser can be tuned by adjusting the sideband's frequency. All cavity locking schemes use the standard Pound-Drever-Hall technique with 20-MHz phase modulation. EOM: electro-optic phase modulator. PD: high-bandwidth photodetector. HWP: half-wave plate. QWP: quarter-wave plate. PBS: polarization beam splitter. SMF: single-mode fiber. IF: interference filter.

unmodulated path. By changing the sideband frequency, the resonant frequency of the near-concentric cavities can be tuned. This method, however, requires optical filters such as etalons to prevent other sidebands and the carrier from coupling to the near-concentric cavity which would inevitably introduce additional complications to the optical setup. Furthermore, as the maximum optical power of the sideband that can be generated is about 40% of the total optical power, one would need a higher emitted power from the lock laser diode to achieve a sufficient trap depth.

To overcome these problems, we instead lock the modulated path to the transfer cavity and the unmodulated path to the near-concentric cavity (see Fig. 4-3). The frequency of the lock laser can be fine-tuned by controlling the frequency of the sideband. We observe that a large tuning of the sideband’s frequency causes the laser lock to loose quickly. To avoid these sudden kicks to the control loop of the laser lock, we therefore change the sideband’s frequency only slowly in steps of 1 MHz per 0.5 seconds in the control script. We determine the frequency of the lock laser using a wavemeter with a resolution of 10 MHz. Setting the sideband frequency $\Delta\nu_l = 160$ MHz, we observe that the resonant laser, the lock laser and the near-concentric cavity are co-resonant. At this sideband frequency, we determine the frequency of the trap laser to be $\nu_{810} = 370.04568(1)$ THz, which is red-detuned below the D2 transition by 14.184 THz. This detuning corresponds to 1043 times of the free spectral range of the near-concentric cavity.

Near-concentric cavity lock

The optical setup for locking the near-concentric cavity is, in principle, similar to the the locking scheme of the transfer cavity (see Fig. 4-4). The two laser beams (810-nm and 780-nm) are combined at a dichroic mirror and coupled to fundamental modes of the near-concentric cavity. The 780 nm laser is used to align the cavity and probe the trapped atoms. A combination of a dichroic mirror and interference filters separates the 780 nm transmission from the 810 nm transmission. The cavity transmission of the 810-nm laser is coupled to a single-mode fiber to clean up the spatial mode and subsequently detected on a high-bandwidth photodetector. Here, the locking error signal is derived from the cavity transmission of 810-nm laser instead of the reflection because multiple-modes interference at the reflecting path may distort the error signal shape. We adjust the frequency of the lock laser by tuning the frequency of the sideband such that the cavity resonances of the 810 nm and 780 nm overlap. We find that it is essential to use angled physical contact (APC) single-mode fibers and optical isolators in the optical setup to reduce back-reflections that cause residual amplitude modulation of the error signal.

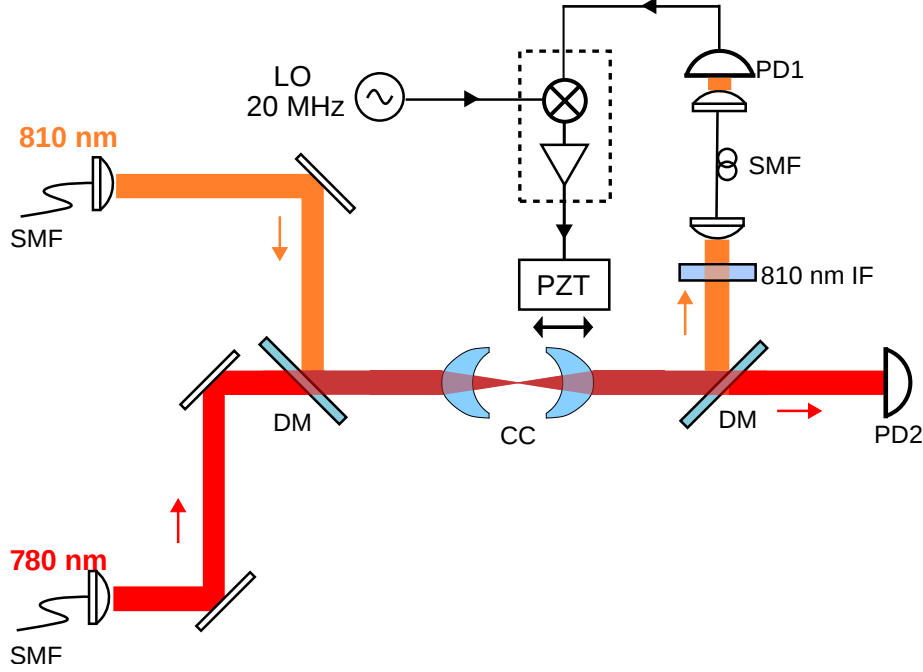


Figure 4-3: Optical locking scheme of the near-concentric cavity. Red and orange lines indicate the beams from 780 nm laser and 810 nm lock laser, respectively. The two laser beams are combined at a dichroic mirror (DM) and coupled to the fundamental modes of the cavity. The locking error signal is derived from the cavity transmission which is coupled to a single-mode fiber for the spatial mode filtering. PD: high-bandwidth photodetector. SMF: single-mode fibers. IF: interference filters.

4.1.2 Locking circuit

The error signals used to lock the cavities are derived using the standard Pound-Drever-Hall (PDH) technique [Drever et al., 1983]. Similar techniques to PDH are the frequency-modulation (FM) spectroscopy and its variation, the modulation transfer spectroscopy, which are used to stabilize lasers to atomic transitions in our experiment [Bjorklund, 1980, McCarron et al., 2008]. The two techniques have the same working principle and are derived from an older method of controlling the frequency of microwave oscillators, also developed by Pound [Pound, 1947]. Consequently, the laser and the cavity locking in our experiment have the same electronic design.

The locking circuit consists of two primary parts: the signal processing part and the control loop (see Fig. 4-4). A direct digital synthesizer (DDS) supplies a modulation signal ($f_m = 20$ MHz). The 20-MHz signal is coherently split into two paths;

one acts as a local oscillator (LO), and the other drives the EOM that modulates the phase of the lasers. The cavity reflection/transmission of the modulated laser is detected on a high-bandwidth photodiode, and the photocurrent is passed to a transimpedance amplifier. The photodiode signal is subsequently amplified and demodulated by multiplying with the LO at a RF frequency mixer (Mini-circuits, RP2). The result of the mixing is a combination of a DC and a high-frequency signal at $2f_m$. The DC part provides the error signal for the locking scheme. Unequal delays between the signal and the LO reduce the magnitude of the error signal [Black, 2001]. We compensate for delays with a phase shifter (Mini-circuits, JSPHS-26) to before the LO. A low pass filter removes the high-frequency signals. The feedback control loop is carried out using an analog Proportional-Integral (PI) controller. The controller output drives the piezo to keep the cavity length on resonance. A sawtooth voltage signal can replace the controller output to scan the cavity length and find a good lock point.

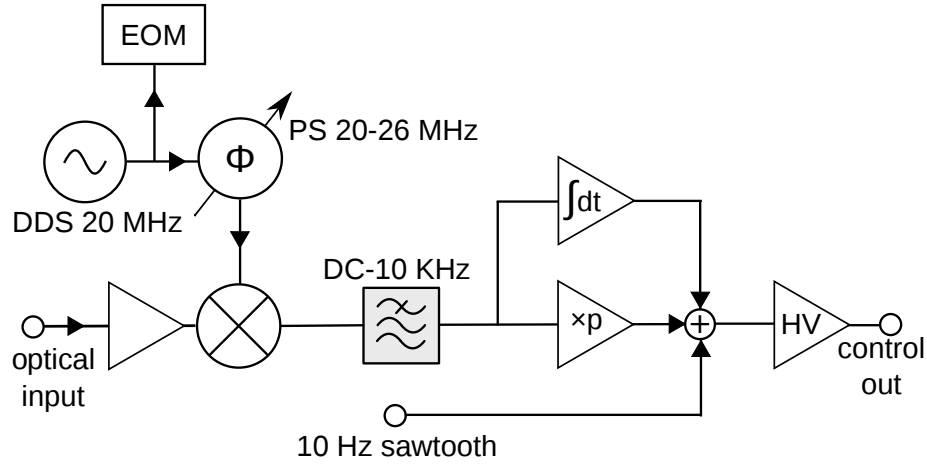


Figure 4-4: Schematic diagram of the electronic circuit to generate the error signal and to lock the cavity resonance using the PDH technique. A modulation signal at 20 MHz drives the EOM and operates as a local oscillator. The optical signal from the cavity reflection/transmission is amplified and demodulated at the mixer to generate the error signal. The control loop consists of Proportional-Integral feedback implemented with operational-amplifiers. The phase shifter (PS) adjusts the phase of the local oscillator (LO) to compensate for the phase offset. HV: high voltage amplifier.

4.2 Transverse stabilization

4.2.1 Transverse misalignment sensitivity

The alignment of near-concentric cavities is sensitive to the transverse position of the cavity mirrors [Yariv, 2010, Wang et al., 2018]. To quantify this effect, we measure the resonant transmission of the cavity fundamental mode coupled to a single-mode fiber as we displace one of the cavity mirrors in x and y directions (see Fig. 4-5). Throughout the measurement, the cavity length is locked to the frequency-stabilized 810-nm laser. The transverse profile in Fig. 4-5 shows a FWHM of 59(3) nm in radial direction. In Fig. 4-6, we repeat the transverse sensitivity measurement every 30 minutes. We observe a directional drift with a time scale correlated to the temperature change in the vicinity of the experiment. Therefore, we attribute the transverse displacement mainly to the thermal expansion of the cavity structure. From the FWHM of the transverse profile, we approximate that a change of temperature of the cavity on the order of 100 mK is sufficient to reduce the resonant transmission of the fundamental mode by 10%. This result re-emphasizes the importance of using a three-dimensional actuator to stabilize the position of the near-concentric cavity mirrors.

4.2.2 Transverse stabilization algorithm

Practical operation of a near-concentric cavity therefore requires either aggressive temperature stabilization, or a transverse locking scheme. Unlike the longitudinal direction, the transverse direction lacks a clear way to derive a locking error signal to implement feedback control. To actively compensate for the transverse drift, we implement an two-dimensional lock-in algorithm based on the gradient-search method to maximize the cavity transmission [Nguyen et al., 2018].

The algorithm is triggered when the cavity transmission drops below a threshold value. The cavity mirror is transversely scanned in incremental steps surrounding the initial position to find the direction of steepest ascent of the cavity transmission. We implement a raster scan to alleviate the hysteresis by avoiding any large voltage jumps send to the piezo. The algorithm repeats the iteration until the cavity transmission reaches the maximum within a predefined tolerance for termination. The size of the

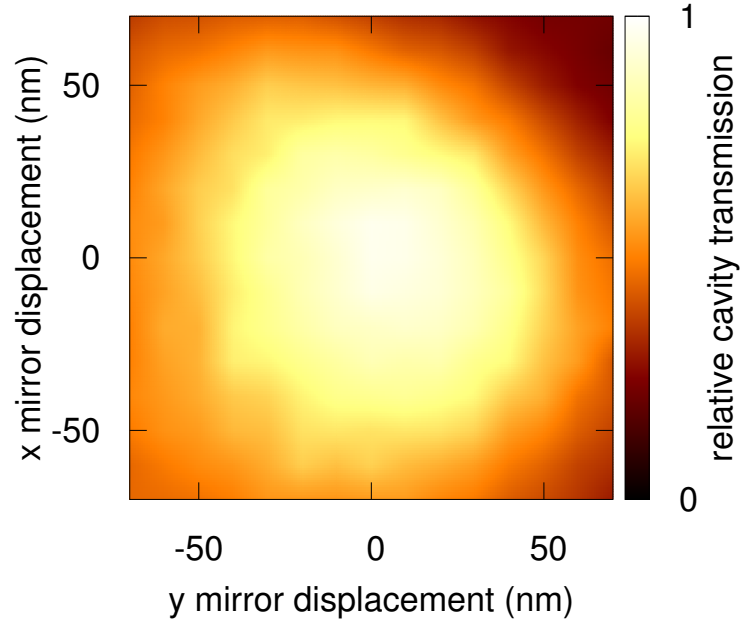


Figure 4-5: Sensitivity of cavity transmission coupled to a single-mode fiber as a function of transverse displacements. The cavity mirror is displaced in x and y directions while the cavity length is stabilized.

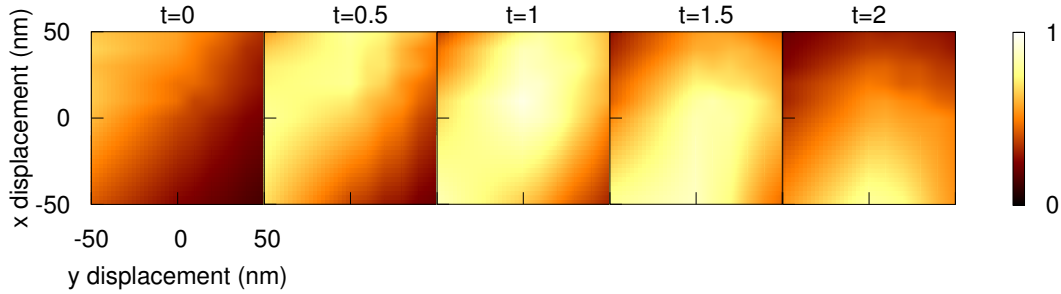


Figure 4-6: Observation of drift of transverse cavity alignment. The cavity transmission coupled to a single-mode fiber as a function of transverse displacements is recorded at an interval of 30 minutes. The drift is directional and is attributed to the thermal expansion of the cavity structure.

scanning step is reduced as the cavity transmission increases to avoid unnecessary “aggressive” correction near to the optimal alignment position.

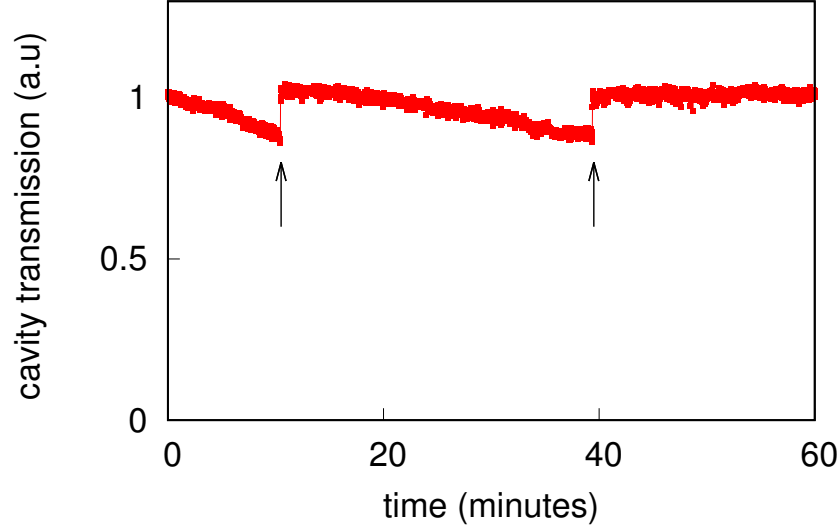


Figure 4-7: Long-term stability of the near-concentric cavity at $d = 207$ nm. The cavity length is locked during the measurement. The slow drift of cavity transmission on the order of minutes is due to the transverse misalignment which is caused by temperature change. Vertical arrows indicate the activation of the stabilization algorithm. The cavity transmission recovers to the maximum value after the successful implementation of the algorithm.

Figure 4-7 shows a typical record of cavity transmission at the last resonant length as the transverse stabilization algorithm is in effect. We attribute the slow drift on the order of minutes to the temperature change of the cavity, while the fast fluctuation of the maximum transmission is due to the vibration of the cavity length. To separate the effects of the fast fluctuation from the transverse offset, the algorithm takes an average of cavity transmission on a time scale that is much longer than the cavity length fluctuation. The threshold can be chosen to be as high as 97% to have a high duty cycle. The average search time to recover to the maximum cavity transmission is on the order of seconds. With a combination of both temperature stabilization and the transverse stabilization algorithm, the near-concentric cavity remains aligned for the course of a few hours.

Chapter 5

Trapping single atoms in a near-concentric cavity

Single atoms interact strongly with a cavity mode when they are placed at locations where the cavity photons exhibit the strongest electric field. The field of photons contained in a Fabry-Perot optical cavity is not uniform; it has a global maximum at an antinode of the cavity focus, decreases in the radial direction (the Gaussian profile), and varies periodically in the axial direction (the standing-wave pattern). Therefore, to obtain the optimal coupling strength, the atoms need to be positioned at the central antinode preferably with a spread of much less than the period of the standing wave $\lambda_{cav}/4$.

The transit time of the atoms through the cavity mode is also an important factor in determining the atom-cavity cooperativity. An atom beam with a velocity v traversing a cavity beam waist w_0 has an effective absorption line broadened by $\Delta\nu_{\text{transit}} \approx v/4\pi w_0$ due to the finite interaction time. For example, a thermal atomic beam of ^{87}Rb at a temperature of 300K has $\Delta\nu_{\text{transit}} = 5.4$ MHz when crossing a cavity beam waist $w_0 = 4 \mu\text{m}$. Another hand-waving argument is that the interaction time between the atoms and the cavity must be longer than one period of the Rabi oscillation. Therefore, in addition to $g_0 > (\kappa, \gamma)$, the strong coupling also requires that $g_0 \gg 2\pi\Delta\nu_{\text{transit}} = 1/\tau_d$, where $\tau_d = v/2w_0$ is the transit time of the atoms in the cavity mode [Kimble, 1998]. Altogether, it is important to trap the atoms with sufficient long storage times in the cavity mode.

Here, we present an experimental setup to trap a single neutral ^{87}Rb atom in a near-concentric cavity. The trap is a red-detuned far-off-resonance intra-cavity dipole trap (FORT) [Ye et al., 1999], implemented in a standing-wave configuration along the cavity axis. The dipole trap depth is on the order of few mK, so a pre-cooled atom cloud is required to load the dipole traps. We prepare a cold cloud of ^{87}Rb atoms directly in the near-concentric cavity mode using the magneto-optical-trap (MOT) technique. This arrangement avoids the need of any sophisticated atom delivery methods such as an atomic fountain and an atomic conveyor belt [Fortier et al., 2007]. The atoms in the MOT are probabilistically loaded into the cavity mode. We detect the trapped atoms based on the atomic fluorescence collected by the cavity mode. In the absence of additional cooling methods, we observe an average trap lifetime of 230(30) ms.

5.1 Magneto-optical traps

Principle of operation

Cooling and trapping of atoms by light-induced forces are two related phenomena. In particular, cooling requires a velocity-dependent force which plays a role of friction or a damping force. Trapping, on the other hand, relies on a position-dependent restoring force, and acts like a spring. A combination of restoring force and friction is able to halt fast moving atoms and constrain them in a well defined region. The magneto-optical-trap (MOT) is a technique developed to simultaneously cool and trap neutral atoms [Raab et al., 1987]. Using the MOT technique, it is able to prepare samples of cold neutral atoms with a temperature of few microkelvins.

The cooling effect in the MOT is realized by overlapping three counter-propagating and circularly polarized laser beams. In addition, the cooling beams must be red-detuned with respect to an atomic transition. Due to the Doppler effect, an atom moving in the overlapping region preferably absorbs the photons from the beam opposite to its motion. When an atom absorbs or scatters a photon, its momentum changes by $\hbar k$ according to the law of momentum conservation. As the scattering is random in all directions, the average momentum transferred to the atom by the emission process is zero. The net result is the slowing down of the atom in the opposite

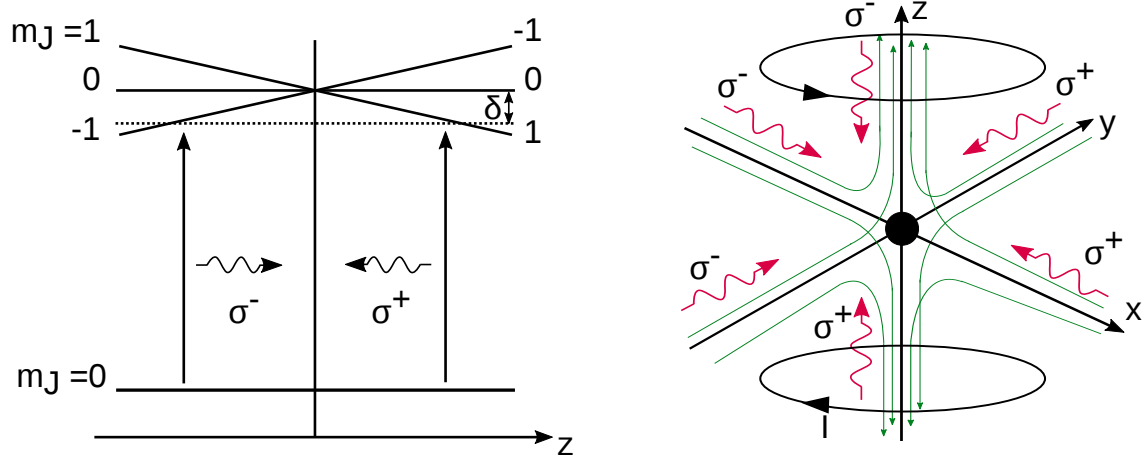


Figure 5-1: Principle of operation of magneto-optical trap. (Left): one-dimensional view of the energy level of atoms located in the magnetic quadrupole field. The degeneracy of excited sub-Zeeman states is lifted and their energy varies linearly with the atomic position. The two counter-propagating lasers are circularly polarized and red-detuned. (Right): three-dimensional view. Green lines indicate the magnetic field lines created by a pair of anti-Helmholtz coils.

direction to the atomic motion, with an effective damping force that is proportional to the velocity of the atoms.

Cold atoms gradually diffuse and eventually escape from the trapping region. Hence, it requires a trapping mechanism to capture and contain the atoms. By introducing a magnetic quadrupole field with a center at the trapping region, the atoms experience a position-dependent light-induced force. This mechanism is illustrated in Fig. 5.1 for the case of $J = 0 \leftrightarrow J = 1$.

When the atoms are displaced, for example, to the right of the trap center, the atomic transition shifts closer to resonance with the σ^+ beam, which propagates to the left, and further away from resonance with the σ^- beam. As a result, the atoms preferably absorb photons of the σ^+ beam. The net effect is that the atoms are pushed back to the opposite direction with a rate proportional to its distance from the trap center.

The effective operation of the MOT relies on the tiny but repetitive momentum kicks from the absorption of red-detuned photons. However, for atoms with high

enough initial velocity, the transit time through the trap is not long enough for many cooling cycles to happen. This is reflected through the capture velocity v_c which is defined as the maximum velocity of the atoms that transverse the trapping region and still can be captured by the MOT. The capture velocity determines the cut-off population of the thermal atomic beams that will be successfully trapped in the MOT. The number of atoms in the MOT is related to the capture velocity and the trapping volume (V_{trap}) by a relation [Lindquist et al., 1992, Gattobigio et al., 2010]:

$$N \propto v_c^4 V_{\text{trap}}^{2/3} \quad (5.1.1)$$

An important experimental parameter that determines both v_c and V_{trap} is the waist of the cooling beams (w_m). For a configuration of three orthogonal MOT beams, we can have an approximation that $v_c \propto \sqrt{w_{\text{MOT}}}$ and $V_{\text{trap}} \propto w_m^3$. As a consequence, $N \propto w_m^4$, which clearly illustrates the importance of having a large beam waist for the MOT cooling beams.

Optical setup

The cooling transition for the MOT in our setup is the closed cycling transition $5S_{1/2}, F=2 \rightarrow 5P_{3/2}, F=3$ of the D2 line of ^{87}Rb (see Fig. 5-4). In contrast to the simplified picture shown in Fig. 5.1, the excited manifold of the D2 line consists of closely spaced hyperfine levels. The atoms can be off-resonantly excited to $5P_{3/2}, F=2$ and subsequently decay to $F=1$ in the ground state, which is a dark state with respect to the cooling transition. This spontaneous decay usually happens before the cold temperature of the atomic cloud can be reached, and thus hinders the formation of the MOT. Hence, we apply a repump laser to transfer the population of the atoms back to the cooling cycle. The repump laser is resonant to the $5S_{1/2}, F=1 \rightarrow 5P_{1/2}, F=2$ transition of the D1 line at 795 nm. More details of the level scheme are shown in Fig. 5-4.

The experimental setup is shown in Fig. 5-2. The cooling and the repump lasers are diode lasers in the Littrow configuration, with frequencies stabilized to reference cells of ^{87}Rb atoms. The repump laser is locked to the cross-over of $5S_{1/2}, F=1 \rightarrow 5P_{1/2}, F=1/2$, and its frequency is shifted up to $F=1 \rightarrow F=2$ using acousto-

optic modulators (AOM) in a double-pass configuration. On the other hand, we lock the cooling laser directly to the cooling transition using the modulation transfer spectroscopy (a variation of the FM spectroscopy technique) [McCarron et al., 2008]. We detune the cooling laser using two single-pass AOMs in the +1 and -1 diffraction order. The cooling and repump lasers are combined on a PBS and coupled to an 1-to-3 fiber beam splitter that delivers optical power to the three MOT beams. The polarization of each output fiber of the fiber beam splitter is controlled by three-paddle polarization controllers.

The large spacing between the cavity mirrors (11 mm) allows us to prepare the MOT at the center of the near-concentric cavity. This removes the need for additional complex setups to deliver the atoms to the cavity. This advantageous feature can be exploited to increase the single-atom loading rate in future experiments. We employ a MOT configuration with an angular separation of 20 degrees between the two vertical MOT beams. The third MOT beam is orthogonal to the cavity axis and the two vertical beams.

The cooling power is recycled by reflecting the MOT beams back to the fibers. The MOT performance requires an intensity balance between the counterpropagating cooling beams. Since the glass cuvette has a transmission of approximately 90% at 780 nm, the reflecting MOT beams lose about 9% of their optical power in comparison to the incoming MOT beams. To compensate for this imbalance, we slightly focus the returning MOT beams to waists of approximately 0.9 mm at the trapping region such that the peak intensity of the two counterpropagating MOT beams is nearly equal.

The frequency of the cooling laser is red-detuned by $1.6\Gamma = 10$ MHz, where $\Gamma = 6$ MHz is the spontaneous-emission rate of the D2 transition. The typical intensity for each cooling beam is about $100 \mu\text{W}$. The total optical power of the repump beams is set to be one third of the cooling power.

The magnetic quadrupole field is realized by a pair of anti-Helmholtz coils. Due to the compact size of the glass cuvette, the anti-Helmholtz coil can be designed with a relatively small diameter of 50 mm and a spacing of 25 mm. The coil provides a magnetic field gradient of 20 G/cm with a current of 1A and therefore little heat generation, which is important to minimize temperature change of the cavity. In

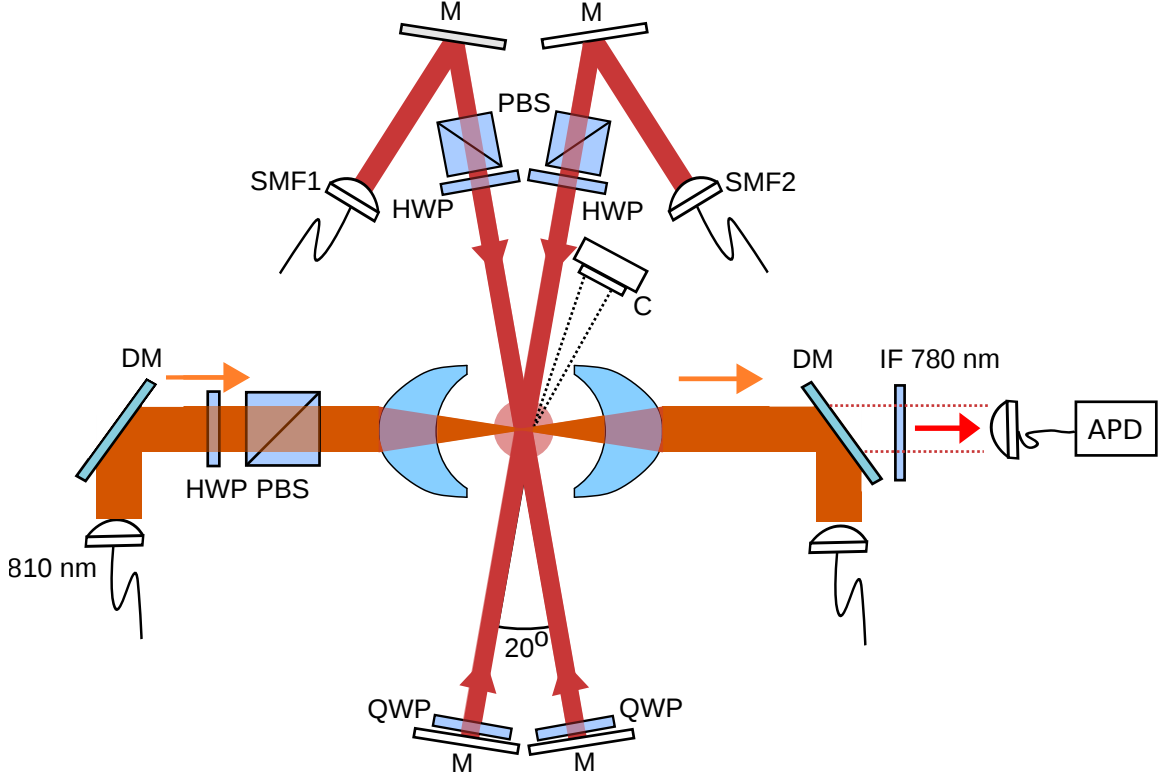


Figure 5-2: Schematic experimental setup of trapping single atoms in the near-concentric cavity. A magneto-optical trap (MOT) of ^{87}Rb is prepared at the cavity focus. The two vertical MOT beams, indicated by red lines, form an angle of 20 degrees. Not shown is the horizontal cooling beam and the magnetic coils. The coil axis is orthogonal to the plane of the paper. The trap laser couples to the fundamental mode of the cavity to form an intra-cavity far-off-resonance dipole trap. Single atoms are probabilistically loaded into the trap and coupled to the cavity mode. The fluorescence light of the trapped single atoms collected into the resonant cavity mode is spectrally filtered and coupled to a single-mode fiber which is attached to an avalanche photodiode (APD).

addition, three orthogonal pairs of coils in a Helmholtz configuration are employed to compensate stray magnetic fields.

The thermal atom source that loads the MOT is a rubidium dispenser (SAES NF series) located 20 cm from the trapping region (see Fig. 5-3). We typically run the dispenser at a heating current of 2.5A to load the trap. To verify that the location of the MOT is at the cavity focus, we image the MOT on a camera placed at the top of the setup. We observe that the MOT becomes unstable in the vicinity of the cavity mode, which is resonantly driven by the probe laser. In addition, the cavity resonant

transmission of a weaker probe beam is significantly reduced in the presence of the MOT. Using these two observations as feedback, we can position the MOT in the proximity of the cavity focus, which is necessary to achieve the optimal atom-cavity coupling strength.

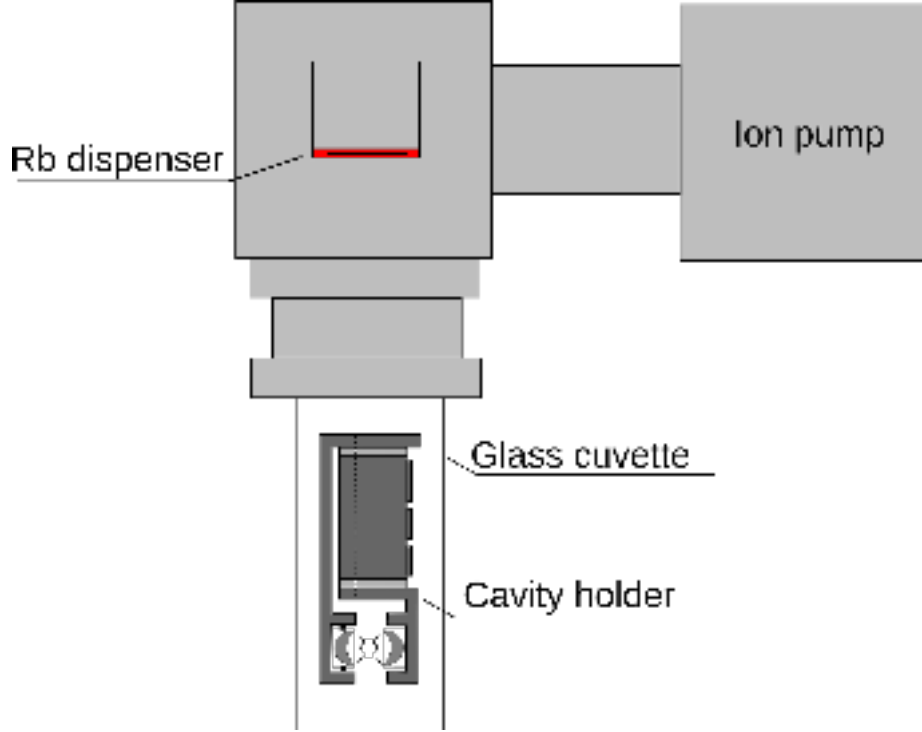


Figure 5-3: Schematic of a vacuum chamber for atom trapping experiments with near-concentric cavities.

5.2 Intra-cavity dipole traps

Radiation pressure traps such as magneto-optical traps are excellent in preparing a cold atomic ensemble with temperature in a range of several microkelvins. However, the number of atoms in the MOT varies from run to run. The minimum attainable temperature of the atomic cloud is limited by atomic recoils in random direction due to the spontaneous emission [Lett et al., 1989]. Furthermore, the internal dynamics of the atoms is strongly perturbed by interacting with the cooling beams on a time scale of microseconds. For the purpose of quantifying the atom-photon coupling strength, it is therefore preferable to switch off all near-resonant interactions with the trapped

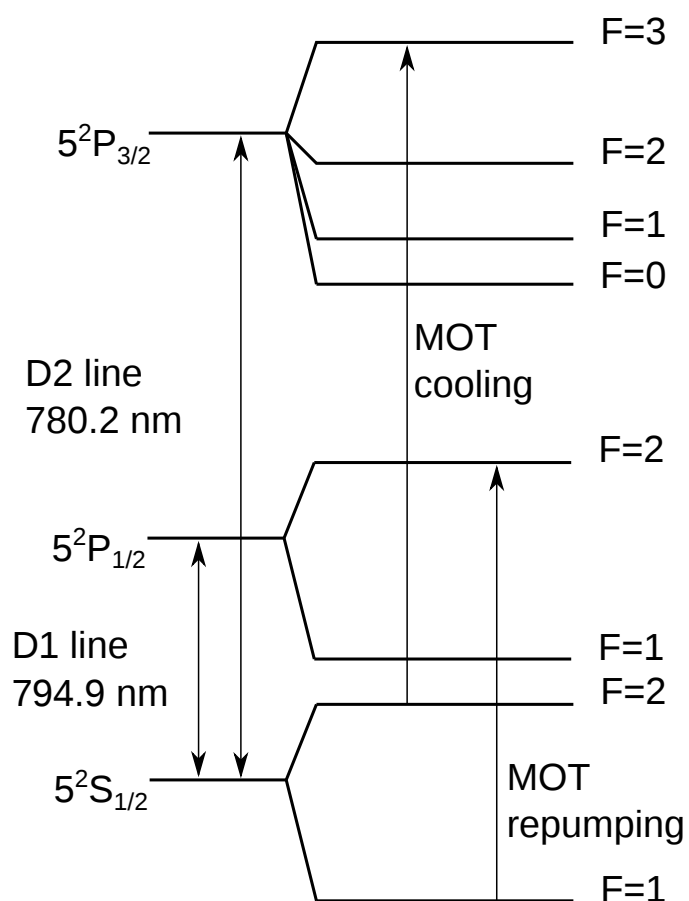


Figure 5-4: ^{87}Rb D1 and D2 transition with hyperfine levels. Shown are the transitions used for MOT cooling and MOT repump lasers.

atoms except the cavity field, and weakly probe the atom-cavity system from the cavity axis.

Another type of radiation forces that does not involve the absorption of light is the dipole force, which is used in far-off resonant dipole traps (FORT). A dipole trap can be experimentally realized in several ways. A common configuration is single-focus trap consisting of a microscope objective or a high numerical aperture lens [Schlosser et al., 2001, Tey et al., 2008]. In a single-focus dipole trap, a collimated Gaussian red-detuned laser beam is focused to a micron-sized waist and forms an intensity maximum to attract the atoms. These traps achieve a high confinement in the radial direction. Another configuration is a one-dimensional optical lattice, where a pair of counter-propagating of laser beams of the same polarization interferes to form a standing wave [Bloch, 2005]. Due to the interference, the intensity at the antinodes increases by four times.

Here, we employ a dipole trap formed by the cavity fundamental mode at 810 nm. This intra-cavity dipole trap has an advantage of increasing the trap depth by a factor proportional to the cavity finesse. For the near-concentric cavity, the cavity beam waist is on the order of few microns which would greatly enhance the trap confinement in the radial direction. In addition, the boundary condition of the cavity ensures the spatial overlap of the dipole trap and the probing field as they both couple to the cavity fundamental modes.

The dipole force

One way to understand simply dipole force is to consider refraction of light by a nearly-transparent objects. Its mechanism can be understood from a classical model in which the atom is treated as a damped harmonic oscillator driven by a classical radiation field. The classical model provides an intuitive way to understand the dipole force and is sufficient to calculate the ground-state shifts and the scattering rate in the low excitation regime. The maximum of the ground-state shift is interpreted as the depth of the dipole trap. Calculation of excited-state energy shift requires the perturbation theory. The full quantum approach with exact treatment of the force fluctuation and momentum diffusion in the dipole trap can be found in [Cohen-tannoudji and Dupont-roc, 1997].

Unlike the radiation pressure the dipole force is a conservative force, and hence its magnitude and direction can be derived from the gradient of the corresponding potential energy. An atom interacting with the radiation field is classically modeled as a driven harmonic oscillator (the Lorentz's model). The electron of the atom is treated as a point-like particle elastically bound to a fixed nucleus by a spring-like force with a resonant frequency ω_0 corresponding to the optical transition frequency. In addition, there is a damping term Γ associated with the radiative decay due to the charge acceleration. The driving term is the Coulomb force acting on the electron by the electric field $E(t) = E_0 e^{-i\omega t}$ of the incident polarized light¹. Denote $x(t)$ as the displacement of the electron from the equilibrium position, the equation of motion of the electron is

$$\ddot{x} + \Gamma \dot{x} + \omega_0^2 x = -eE(t)/m_e. \quad (5.2.1)$$

The electric dipole moment of the atom is related to the displacement as $d(t) = ex(t)$, where e is the elementary charge. Consider only a small displacement of the electron, to the first order approximation, the induced dipole moment responses linearly to the driven electric field: $d(t) = \alpha(\omega)E(t)$, where $\alpha(\omega)$ is polarizability. Integration of Eq. 5.2.1 yields the explicit expression for the polarizability,

$$\alpha(\omega) = \frac{e^2}{m_e} \frac{1}{\omega_0^2 - \omega^2 - i\omega\Gamma}. \quad (5.2.2)$$

The potential energy of the dipole interaction is:

$$U_{dip}(\mathbf{r}) = -\frac{1}{2} \langle dE \rangle = -\frac{1}{2\epsilon_0 c} \text{Re}(\alpha) I(\mathbf{r}), \quad (5.2.3)$$

where the brackets denote the time average over many oscillation periods of the electric field, \mathbf{r} is the position vector of the atom, and $I(\mathbf{r}) = 2c\epsilon_0 |E_0|^2$ is the electric field intensity.

The dipole force results from the gradient of the dipole potential

$$\mathbf{F}_{dip} = -\nabla U_{dip}(\mathbf{r}) = \frac{1}{2\epsilon_0 c} \text{Re}(\alpha) \nabla I(\mathbf{r}) \quad (5.2.4)$$

¹As the laser light is polarized, the electric field and the induced displacement of the electron can be taken as scalar value in the basis of the polarization vector.

The dipole force is only approximately conservative, as the atoms can dissipate the energy by absorbing and scattering the photons. This photon scattering of atoms in the dipole trap sets the limit for the trap lifetime. Due to the limited available excited states in the two-level system, each absorption event of the atoms must be followed by an spontaneous re-emission of a photon. As a result, the scattering rate is determined by the absorbed optical power divided by the energy per photon of the driving field

$$R_{sc} = \frac{P_{abs}(\mathbf{r})}{\hbar\omega} = \frac{\langle \dot{d}E \rangle}{\hbar\omega} = \frac{1}{\hbar\epsilon_0 c} \text{Im}(\alpha) I(\mathbf{r}). \quad (5.2.5)$$

The separate contribution of the imaginative and the real part of the polarizability in Eq. 5.2.4 and 5.2.5 consolidates our initial view on the nature of the dipole force and the radiation pressure. In particular, $\text{Re}(\alpha)$ gives a measure of the refractive index of the atomic medium. Its variation extends over a large range of frequency and has an asymmetrical lineshape across the resonant atomic frequency. This reflects the dispersive nature of the dipole force. On the other hand, $\text{Im}(\alpha)$ has a Lorentzian profile with a peak on resonance and is related to the absorption coefficient.

For large detuning $\Delta = \omega - \omega_0$, the dipole potential and the scattering rate can be approximated as

$$U_{dip}(\mathbf{r}) = \frac{\hbar\Gamma^2}{8I_0} \left(\frac{1}{\omega - \omega_0} + \frac{1}{\omega + \omega_0} \right) I(\mathbf{r}), \quad (5.2.6)$$

$$R_{sc}(\mathbf{r}) = \frac{\Gamma^3}{8I_0} \left(\frac{1}{\omega - \omega_0} + \frac{1}{\omega + \omega_0} \right)^2 I(\mathbf{r}), \quad (5.2.7)$$

where $I_0 = 1.67 \text{ W/cm}^2$ is the saturation intensity of the D_2 transition of ^{87}Rb atoms. Making the rotating-wave approximation ($\Delta \ll \omega_0$), we can neglect the counter-rotating term $\omega + \omega_0$, and Eq. 5.2.6 and 5.2.7 are simplified to:

$$U_{dip}(\mathbf{r}) = \frac{\hbar\Gamma^2}{8I_0\Delta} I(\mathbf{r}), \quad (5.2.8)$$

$$R_{sc}(\mathbf{r}) = \frac{\Gamma^3}{8I_0\Delta^2} I(\mathbf{r}). \quad (5.2.9)$$

The trap potential scales as $I(\mathbf{r})/\Delta$ while the scattering rate scales as $I(\mathbf{r})/\Delta^2$. Therefore, in experiments, it is preferable to have a large detuning to minimize the

scattering rate given a certain trap depth. Another observation is that the direction of the dipole force depends on the sign of the detuning Δ . This leads to the division of the dipole trap into two classes: red-detuned traps and blue-detuned traps. For red-detuned trap ($\Delta < 0$), the dipole potential is negative, and the atoms are trapped at the local minima of the trap potential, which coincide the maximum intensity of the trap laser. Above resonance ($\Delta > 0$), the dipole force repels the atoms to the locations where the intensity is minimum.

Without deriving the explicit expression for the dipole trap potential, its sign can be inferred from the phase relationship between the driven harmonic oscillator and its driving field. Below resonance, the oscillator follows the driving field, hence the product $\langle dE \rangle \simeq \langle \sin(\omega t) \rangle^2$ is positive. Above the resonance, the oscillator has a π phase lag behind the driving field. As a result, $\langle dE \rangle \simeq \langle \sin(\omega t) \sin(\omega t + \pi) \rangle = -\langle \sin(\omega t) \rangle^2$ is negative.

Before moving on to the application of the dipole trap for the near-concentric cavity, there is a caveat about the above derivation that worth mentioning. We have so far described the dipole force in a classical framework, utilizing only Newton's laws and the Coulomb force. One may ask at which conditions the classical model will break down and the full quantum treatment is required. In fact, if we are interested in only the averaged values and limits ourself in the low atomic excitation regime, which is valid for the far-off-resonant dipole trap, the expressions for the dipole potential and the scattering rate in the two frameworks are identical [Grimm et al., 2000]. However, the estimation of the decay rate Γ is different. In the classical treatment, the decay rate Γ is calculated from the Lamor's formula:

$$\Gamma_{\text{classical}} = \frac{e^2 \omega_0^2}{6\pi\epsilon_0 m_e c^3}. \quad (5.2.10)$$

In quantum theory, the radiative decay of the electron can no longer be treated as a continuous process resulting from the acceleration of the the charge particles, but a discrete jump between two energy-levels. The radiative decay rate is then called the spontaneous emission rate, and determined by the matrix element of the dipole moment between the ground and the excited states:

$$\Gamma = \frac{\omega_0^3}{3\pi\epsilon_0 \hbar c^3} |\langle e|\mu|g \rangle|^2. \quad (5.2.11)$$

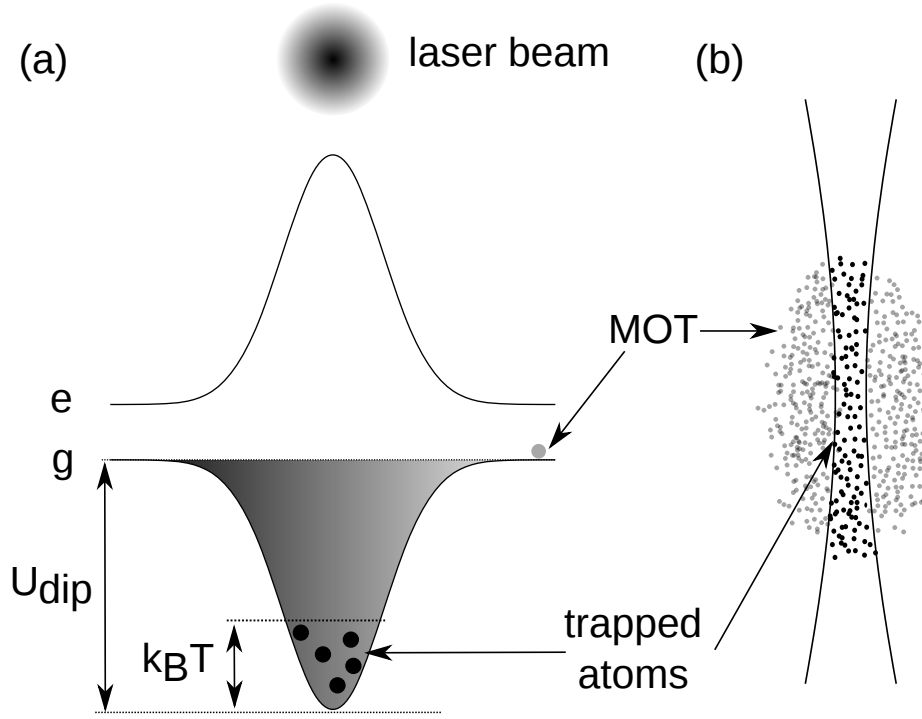


Figure 5-5: (a) Energy level of atoms interacting with a red-detuned laser. The atomic energy is shifted according to the laser-intensity profile. The ground-state atoms are attracted to the maxima of the intensity, while the excited-state atoms are repelled from it. (b) Atoms from the MOT can be loaded to the dipole trap when their kinetic energy $k_B T$ is below the trap depth U_{dip} .

Another limit of the classical theory is its incapability to estimate the dipole potential when the atom is not in the ground state. The dipole potential that experienced by the excited atoms has the opposite sign compared to those values calculated for the ground state (see Fig. 5-5). This can be explained by using the dressed-state formalism and numerically calculated with the perturbation theory where the dipole potential is the energy shifts of the atomic eigenstates (AC Stark-shift) [Cohen-tannoudji and Dupont-roc, 1997].

Calculation of the trap depth

In this section, we calculate the dipole trap depth and the scattering rate of the intra-cavity dipole trap. First, we derive the intra-cavity power from the cavity transmission under the ideal condition of no cavity losses. The relation can be obtained from the

more general equations of optical resonators [Saleh and Teich, 2001]. Here, we choose a simpler way which relies on an intuition that on resonance the cavity is an optical storage. We depict the optical beam as a stream of infinitesimally thin optical pulses. When an optical pulse couples to the cavity, it will be contained in the cavity with an average lifetime of τ_{cav} . At a given time and at a transverse plane inside the cavity, the total optical power is the summation of the power of all optical pulses which have been circulating in the cavity. As a result, the intra-cavity optical power is enhanced by a factor of α_e which is equal to the number of circulating pulses during τ_{cav} :

$$\alpha_e = \frac{\text{duration of a photon stays in the cavity}}{\text{the round trip time}} = \frac{\tau_{\text{cav}}}{2L/c}. \quad (5.2.12)$$

Substituting $\tau_{\text{cav}} = 1/2\pi\gamma$, we obtain:

$$\alpha_e = \frac{c}{4L\pi\gamma} = \frac{F}{2\pi}, \quad (5.2.13)$$

where F is the cavity finesse. This yields the relationship between the cavity transmission power and the intra-cavity power:

$$P_{\text{intra}} = 2\alpha_e P_t = \frac{F}{\pi} P_t, \quad (5.2.14)$$

where the factor of two comes from the fact that we only measure the transmission from one side.

The spatial profile of the dipole potential of the intra-cavity trap follows the spatial intensity distribution of the cavity fundamental mode

$$U_{\text{dip}} = -U_0 \frac{w_0^2}{w^2(z)} \exp \left[-\frac{2(x^2 + y^2)}{w^2(z)} \right] \cos^2 \left(\frac{2\pi}{\lambda} z \right), \quad (5.2.15)$$

with the cavity beam waist w_0 , and the beam radius $w(z) = w_0(1 + z^2/z_R^2)^{1/2}$.

The trap depth U_0 is given by Eq. 5.2.8 as

$$U_0 = \frac{\hbar\Gamma^2}{8I_0\Delta} I_{\text{max}}, \quad (5.2.16)$$

where the peak cavity intensity is

$$I_{\max} = \frac{4P_{\text{intra}}}{\pi w_0^2} = \frac{4F}{\pi^2 w_0^2} P_t. \quad (5.2.17)$$

The factor of four accounts for the standing-wave pattern: the electric field at the antinode of the cavity mode has twice the amplitude, and hence four times of the intensity compared to the running wave case. Combining these results, we can relate the dipole trap depth to the cavity finesse and beam waist

$$U_0 = \frac{\hbar \Gamma^2}{2I_0 \Delta} \frac{F}{\pi^2 w_0^2} P_t. \quad (5.2.18)$$

The scattering rate is obtained in a similar way

$$R_{sc} = \frac{\Gamma^3}{2I_0 \Delta^2} \frac{F}{\pi^2 w_0^2} P_t. \quad (5.2.19)$$

Experimental setup

The dipole trap laser is simultaneously used to lock the near-concentric cavity. The frequency stabilization of the trap laser was discussed previously in chapter 4. Here, we provide more details which are relevant to the single-atom trapping experiment.

We couple the linearly polarized trap laser to a fundamental transverse mode of the near-concentric cavity. With a typical input power of 2.6 mW, we observe a cavity transmission of about $100 \mu\text{W}$. Using the methods describe chapter 3, we measure a cavity finesse of 100 and a cavity coupling efficiency of 22% at 810 nm. As the dipole trap is linearly polarized, all of the Zeeman states of the ground states have an equal trap depth. Figure. 5-6 shows the trap potential of the near-concentric cavity operated at the critical distance $d = 1.7 \mu\text{m}$ corresponding to a beam waist of $4.1 \mu\text{m}$. From Eq. 5.2.19 we predict that the trap depth is 27 MHz and the scattering rate is 11 events per second.

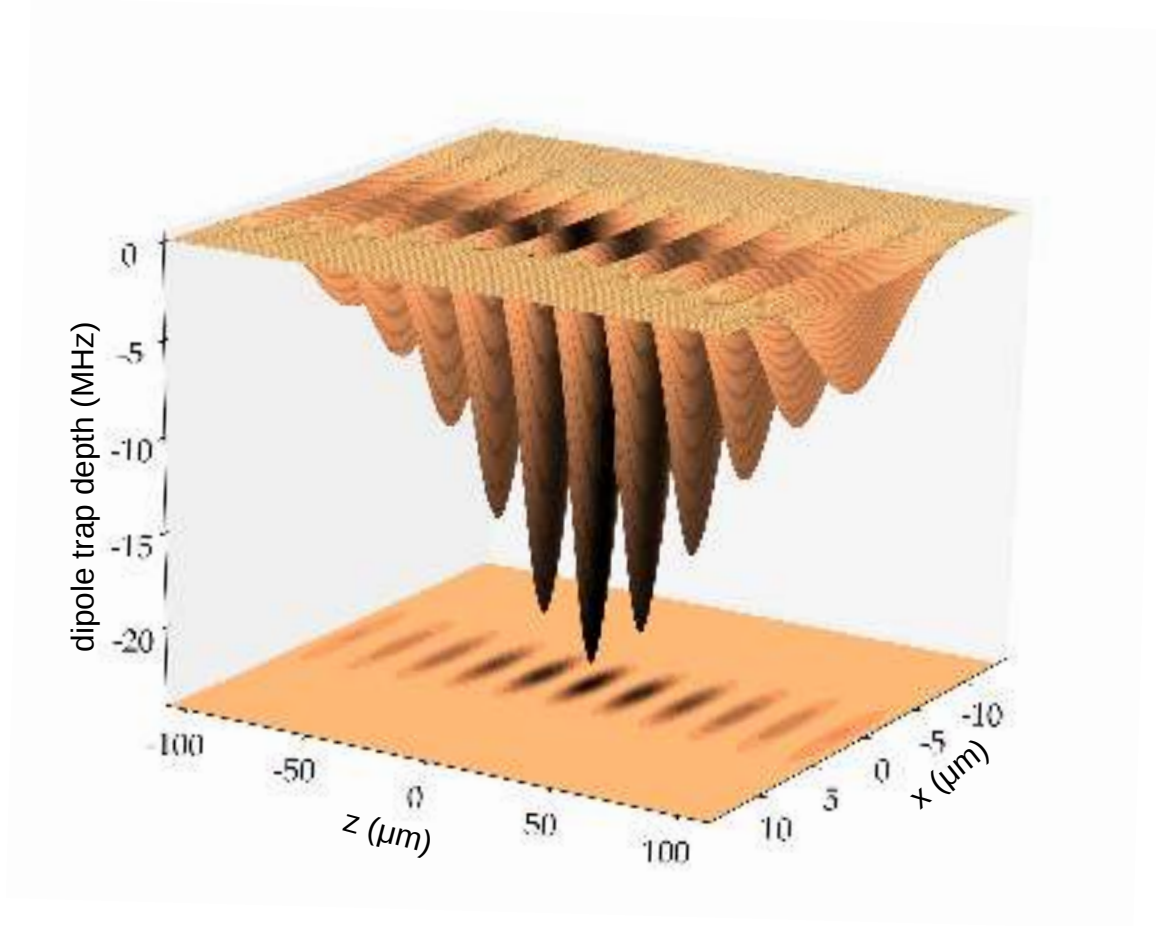


Figure 5-6: Intra-cavity dipole potential of the near-concentric cavity. The cavity length is set at $1.7 \mu\text{m}$ away from the concentric point. The intra-cavity power is 11 mW. The wavelength was stretched by a factor of 100 in z direction to display individual trapping sites.

5.3 Detection of single atoms

Cold atoms from the MOT are probabilistically loaded into the intra-cavity dipole trap when their kinetic energy is well below the trap depth. As the dipole trap and the resonant cavity mode share the same spatial mode, the trapped atoms would scatter photons from the MOT cooling beams to the cavity. The near-resonant scattering rate is proportional to the position-dependent coupling strength $g_0(\vec{r})$. Hence, to determine if the single atoms are loaded into the cavity, we monitor and analyze the atomic fluorescence into the cavity mode at 780 nm wavelength. We couple the

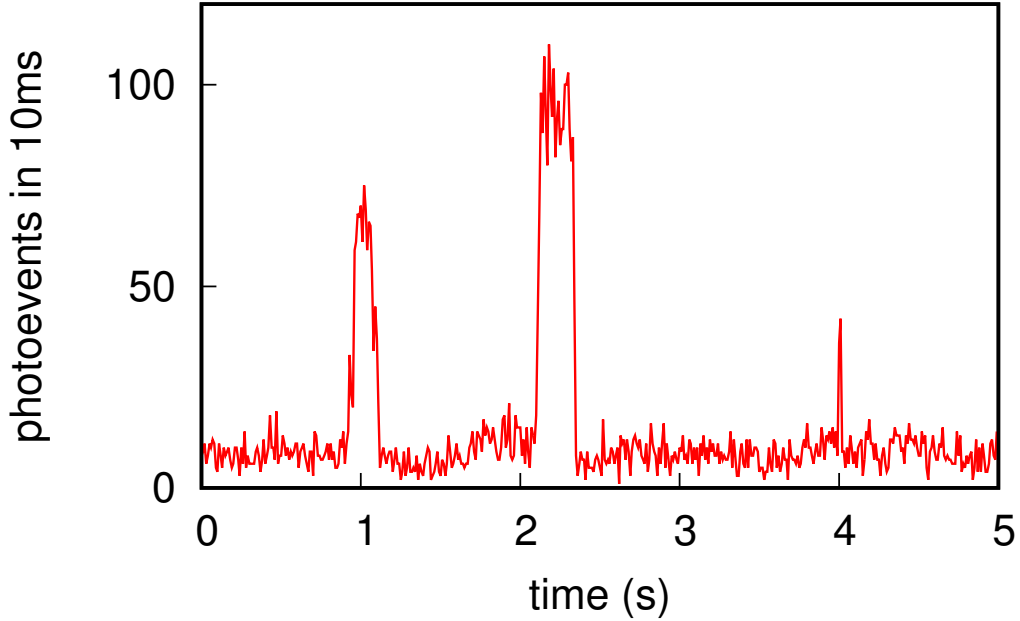


Figure 5-7: Typical trace of detection events during the atom loading process. The sudden increase of fluorescence indicates the entering of an atom into the dipole trap.

cavity transmission of 780 nm to a single-mode fiber, which is subsequently detected by an APD (see Fig. 5-2). To account for the light shift induced by the trap, the cavity length is set so that the resonance frequency is 22 MHz higher than the atomic transition ($\Delta_{ca} = 22$ MHz). While operating the MOT with the presence of the dipole trap, we detect the coupling of individual atoms to the fundamental cavity mode by the sudden increase of photoevents at the APD. The photoevents are recorded and time-tagged with a timestamp device. On the other hand, the sudden decrease indicates the escape of the atoms out of the trap. Figure 5-7 shows a typical time trace during the loading process exhibiting a telegraph signal which is characteristic for single atom loading. The background is mainly due to cavity mirrors' shields scattering the MOT beams into the cavity mode.

Even though the cavity beam waist is small ($\omega_0 \approx 4.1 \mu\text{m}$), we are not operating the dipole trap in a regime of collisional blockade that ensures a single-atom occupancy at any trapping event [Schlosser et al., 2002]. The standing-wave pattern of the cavity mode creates many independent trapping sites at antinodes. The large number of the trapping sites increases the probability of loading more than one atom. We estimate

the number of trapping sites n_{tr} as the number of antinodes in the interval of two Rayleigh ranges of the cavity mode

$$n_{tr} \approx \left[\frac{4z_R}{\lambda_{810}} \right] = \left[\frac{4\pi w_0^2}{\lambda_{810}^2} \right], \quad (5.3.1)$$

where the square brackets denotes the nearest integer function. For the cavity with a beam waist of $4.1 \mu\text{m}$, there are about 250 trapping sites. However, we can operate the MOT at a regime such that the frequency of the loading is low (less than one event per second). Hence, the probability of simultaneously loading more than two atoms in the center region of the cavity is small. Figure 5-8 shows samples of fluorescence of trapped atoms. We posit that it is unlikely for more than one atoms to enter and escape the trap simultaneously. This leads us to attribute the loading of single atoms to samples that have a clear telegraph signal with a sharp transition between two levels. For comparison, the loading of two atoms is also shown in Fig. 5-8(b). Based on this classification, we estimate the probability of a successful loading of single atoms to be approximately 30%.

Measurement of atom lifetime

After loading the atoms, we switch off the cooling and repump light. The quadruple magnetic field is also switched off to disperse the MOT. We wait for a period of τ and switch on the cooling lasers to detect the presence of the trapped atoms. Figure 5-9 shows the survival probability as a function of τ . We determine a $1/e$ lifetime of 230(30) ms from an exponential fit.

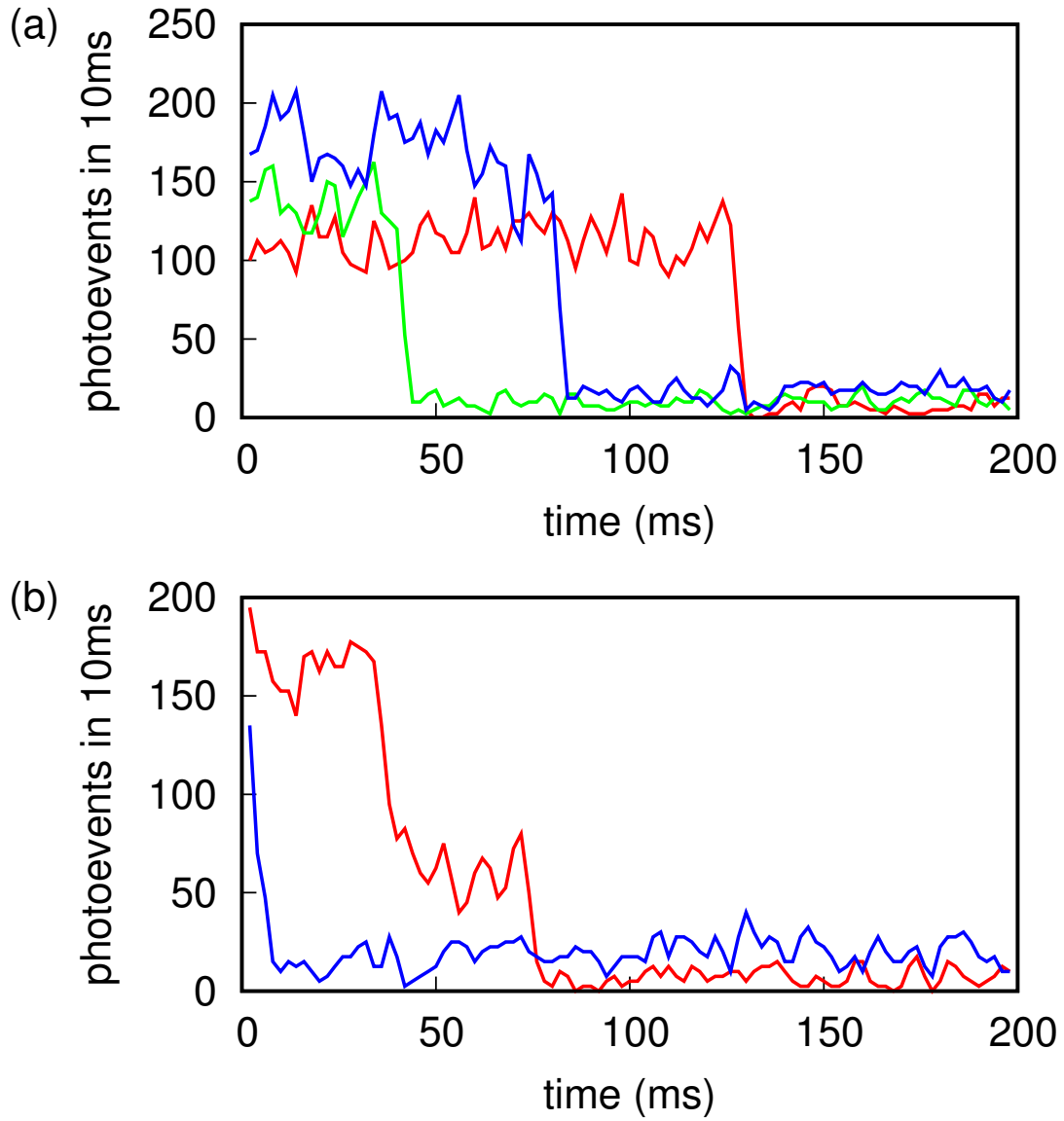


Figure 5-8: Samples of fluorescence of trapped atoms in the cavity mode. (a) The fluorescence of single atoms exhibits a clear telegraph signal characteristic. (b) Representative traces of short-lifetime atoms (blue) and two atoms (red).

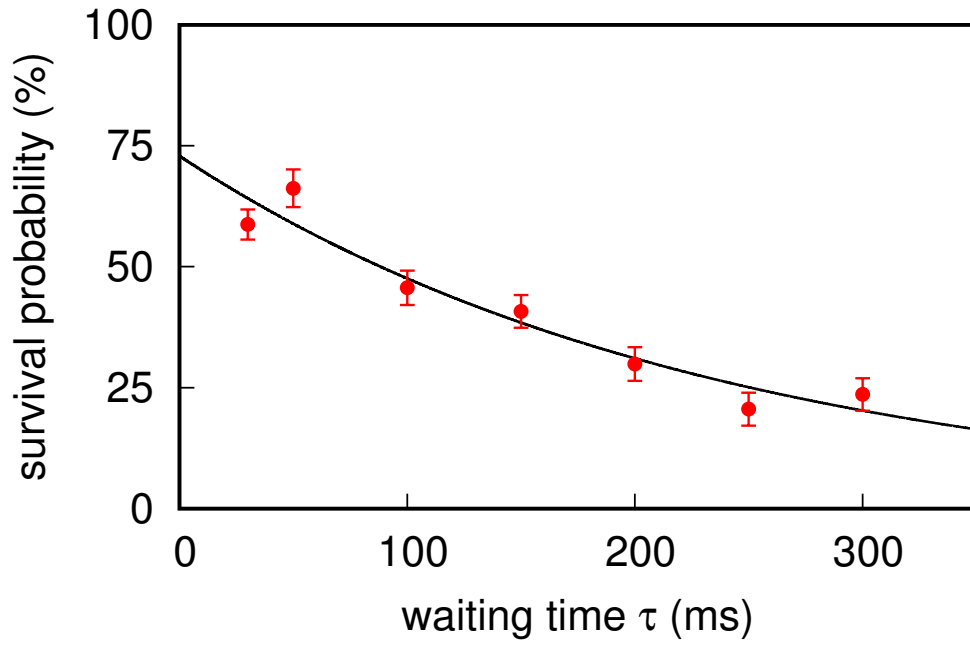


Figure 5-9: Lifetime of single atoms in the dipole trap without cooling light for a duration τ . The solid line represents an exponential fit with a $1/e$ lifetime of 230(30) ms.

Chapter 6

Determining the atom-cavity interaction

In this chapter, we cover an experiment to determine the interaction strength between a single ^{87}Rb atom and a fundamental transverse mode (LG_{00}) of the near-concentric cavity via a direct spectroscopic measurement. For this purpose, the cavity length is chosen such that the frequencies of the transverse modes are not degenerate, preferably with a transverse mode spacing larger than the cavity linewidth of $99(1)\text{ MHz}$. Therefore, we choose the cavity length to be $1.7\text{ }\mu\text{m}$ shorter than the critical point at which the transverse mode spacing is $112(18)\text{ MHz}$. We stabilize the cavity such that a transverse LG_{00} mode is near-resonant with the $5S_{1/2}, F=2 \rightarrow 5P_{3/2}, F=3$ transition. We discuss methods of probing the atom-cavity system in section 6.1. To obtain the cavity spectrum, we need to detune the probe laser frequency in a range of at least one to two times of the cavity linewidth, while the probe power must be maintained constant. Such detuning range is not technically trivial as conventional methods of using acoustic optical modulators (AOM) mostly support a range from 50 MHz for a single pass configuration to 100 MHz for a double pass configuration. We then present two techniques for detuning the laser frequency in a range of $\pm 100\text{ MHz}$ with constant optical power. Next, we describe an optical setup and an experimental procedure to obtain the atom-cavity spectrum. The experimental procedure consists of a control scheme to stabilize the near-concentric cavity in all directions and an experiment sequence of trapping and probing atoms. Subsequently,

we present and analyze the transmission and reflection spectrum in section 6.5. We observe a two-peaked structure of the cavity transmission and reflection spectra from which we determine an atom-cavity coupling strength $g_0 = 2\pi \times 5.0(2)$ MHz and the single-atom cooperativity $C_0 = g_0^2/(2\kappa\gamma) = 0.084(4)$.

6.1 Methods of probing the atom-cavity interaction

The radiative coupling between an atom and a cavity field alters the energy structure and the dynamic response of both systems. Consequently, either steady-state response (frequency domain) or transient response (time domain) of the atom-cavity system can be probed to determine the atom-cavity coupling constant g_0 . In the transient response method, a short probe pulse excites either the atom or the cavity, and the subsequent decay of the cavity field is recorded. In the strong coupling regime, the cavity decay shows an oscillation in response to a sudden reduction of the cavity field, in contrast to the otherwise exponential decay of the empty cavity. This oscillation of the cavity field is a physical manifestation of a reversible energy exchange between the cavity mode and the atom at the rate of $2g_0$. Significant ringing can be observed only when more than one oscillation occurs before the energy of the system is dissipated to the environment. This is equivalent to the fundamental consideration of the condition for strong coupling that the coherent interaction must dominate the other irreversible decay channels. Probing either the atom or the cavity in this regime yields similar information about the properties of the composite atom-cavity system.

In the regimes of weak and intermediate coupling, the presence of one system perturbs the other. Similar to the free-space scenario, the atom emission into the cavity mode is an exponential decay but with a modified rate; the emission rate Γ_{cav} can be either enhanced or suppressed depending on the relative size of cavity parameters (g_0, κ, γ) . Such modification was predicted by [Purcell et al., 1946, Kleppner, 1981] and observed in [Goy et al., 1983]. In the broad cavity limit where $\kappa \gg \gamma$, the decay rate Γ_{cav} is given by

$$\Gamma_{\text{enh}} = \frac{2g_0^2}{\kappa} . \quad (6.1.1)$$

Therefore, the coupling strength can be induced from the linewidth of the atomic emission spectrum [Heinzen et al., 1987].

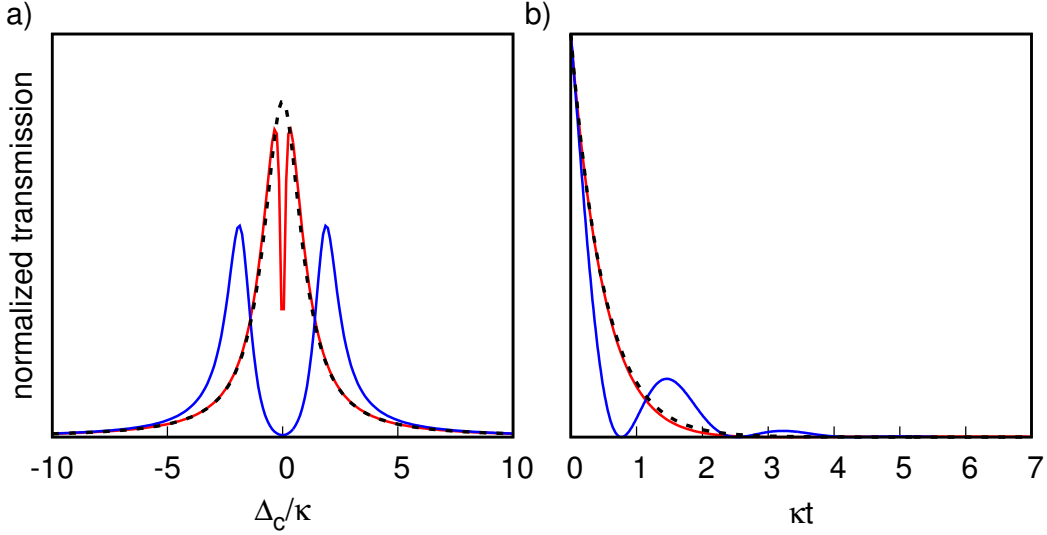


Figure 6-1: Modifications of the cavity field by a single atom observed via two different probing methods: (a) the cavity transmission spectrum and (b) the decay of the cavity field. In the strong coupling regime with $(g_0, \kappa, \gamma) = 2\pi \times (20, 11, 3)$ MHz (blue solid lines), evidence of the normal modes are a distinctive doublet of the spectrum and the ringing of the cavity decay. In contrast, there is lineshape splitting but no ringing for the case of $(g_0, \kappa, \gamma) = 2\pi \times (12, 50, 3)$ MHz (solid red lines). For comparison, the empty-cavity case is shown and indicated by dashed black lines.

On the other hand, the steady-state response can be obtained with spectroscopic measurements. A weak coherent probe beam is coupled to the cavity, and the cavity transmission is recorded as the probe frequency is tuned across the atom-cavity resonance. A manifestation of a significant atom-cavity coupling is a modification of the cavity spectrum. In the case of strong coupling, the cavity transmission spectrum exhibits two distinct Lorentzian lineshapes centered at normal mode frequencies ω_+ and ω_- . Hence, the atom-cavity coupling strength can be induced from the spectrum as $2g_0 = \omega_+ - \omega_-$. However, the observation of the splitting does not infer the normal-mode ringing observed in the transient response. In other words, the appearance of the doublet is only a necessary condition for the strong coupling.

The transient response method requires probing the cavity at only one frequency detuning. This has the advantage of a short measurement duration, and is favorable

to experiments that are challenging to be kept stable over long periods of time, such as with the near-concentric cavity in this work. However, in the weak and intermediate coupling regimes, the effect of the atom-cavity coupling on the cavity field is less evident in the time domain than in the frequency domain. After the mirror contamination (see section 3.4), the optimal atom-cavity parameters of the near-concentric cavity are predicted to be $(g_0, \kappa, \gamma) = 2\pi \times (12, 55, 3)$ MHz. A theoretical prediction of the transmission spectrum and cavity field decay for these parameters is shown in Fig. 6-1 (red solid lines), in comparison to the strong coupling case (blue solid lines) and the empty-cavity case (dashed black lines). In the transient response, using Eq. 2.2.3, we predict the cavity decay rate only slightly increases from 3.18 ns for the empty-cavity case to 3.35 ns for the coupled atom-cavity case; whereas the splitting can be observed clearly in the cavity spectrum. Therefore, a spectroscopic measurement was selected to determine g_0 in our experiment.

6.2 Wide-range detuning of laser frequencies

The near-concentric cavity has a linewidth of 99 MHz. Hence, the probe frequency detuning has to be on the order of ± 100 MHz with respect to the atom-cavity resonance. Besides, the optical power of the probe laser that couples to the cavity must be constant across the detuning range. This can be a technical challenge for the laser system involved. In this section, we describe two solutions to this technical problem.

6.2.1 Detuning by AOM

Experiments frequently employ acoustic-optic modulators (AOM) to detune laser frequencies. As the AOM has a limited operating bandwidth, the diffracted optical power drops significantly at large detuning frequencies. Here, we employ a feedback algorithm to keep the optical power of the diffracted beam constant across the detuning range. With an improvement in the speed of the control loop, this method can also be used to continuously stabilize the lasers power

The probe laser frequency ω_p is locked to the $5S_{1/2}, F=2 \leftrightarrow 5P_{3/2}, F=3$ of the D2 line in ^{87}Rb using the transfer modulation spectroscopy [McCarron et al., 2008] ($\omega_p = \omega_a$). Also, the near-concentric cavity length is set to be near-resonant

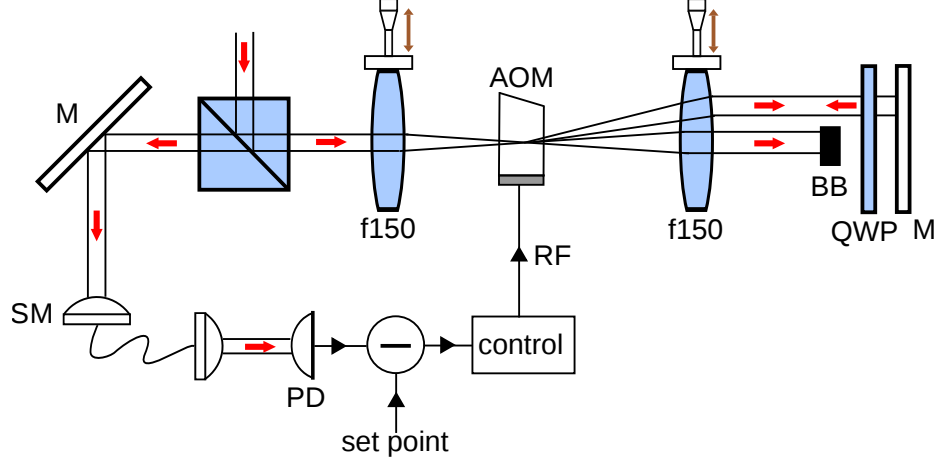


Figure 6-2: Schematic drawing of a double-pass AOM setup for large detuning of laser frequencies. The optical power after the single-mode fiber is detected and compared to a set point. A control program adjusts the RF power to the AOM to minimize their difference. Lenses have a focus of 150 mm, and their positions orthogonal to the laser beam can be adjusted to compensate for the beam deflections. Red arrows indicate laser beams; black triangles indicate the flow of electronic signals. BB: beam blocks.

with this atomic transition ($\omega_c \approx \omega_a$). To detune ω_p , we employ two AOMs in a double-pass configuration with +1 and -1 order outputs. The optical layout of one AOM setup is shown in Fig. 6-2. After the AOM setups, the probe laser frequency is $\omega_p = \omega_a + \omega_{RF1} - \omega_{RF2} \approx \omega_c + \omega_{RF1} - \omega_{RF2}$. The probe-cavity detuning is controlled by setting the difference of the AOM frequencies ($\omega_{RF1} - \omega_{RF2}$). A single-mode optical fiber separates the two AOM setups to decouple their optical alignments. An algorithm adjust the RF power applied to the AOM to minimize the difference between measured values and a setpoint. We choose the setpoint low enough such that the RF power does not exceed the saturation power to prevent thermal damages of the AOMs. The ratio of the standard deviation and the average of the diffracted optical power shows a value of $\sigma_P \approx 2\%$ for one double-pass AOM setup (see Fig. 6-3). Also shown in the figure is the measured optical power without the compensation algorithm. Using two double-pass AOMs with the compensation algorithm, the probe laser frequency can be detuned in a range of ± 100 MHz with $\sigma_P \approx 2\%$. A disadvantage of this setup is that the overall diffraction efficiency is 6% after two double-pass AOMs.

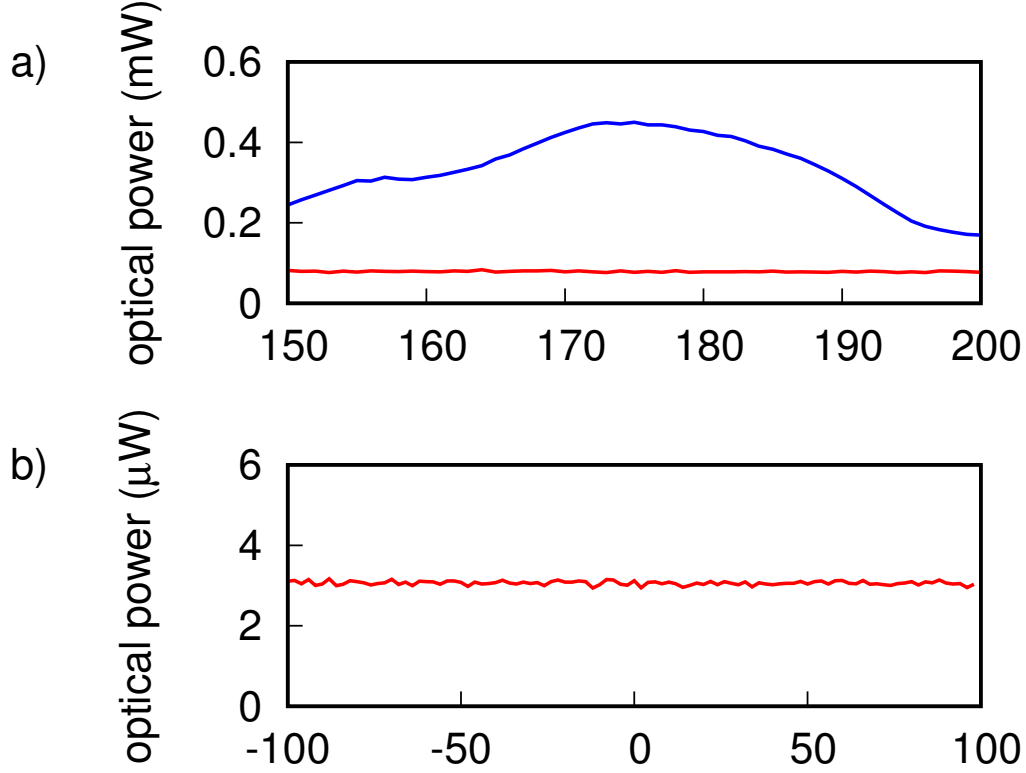


Figure 6-3: Detuning laser frequency by AOMs. The optical power of the first order diffracted beams coupled to a single mode fiber is monitored as the RF driving frequency is detuned. (a) The case of one AOM in the double-pass configuration. The deviation of the diffracted optical power is about 25% without the compensation algorithm (blue trace), and reduced to about 2% with the compensation algorithm (red trace). (b) Optical output after two double-pass AOM. A deviation of about 2% in the diffracted optical power is observed for a detuning range of ± 100 MHz.

6.2.2 EOM sideband locking

The sideband-locking technique presented in section 4.1.1 can be applied to detune the probe laser frequency. The optical setup of the probe laser is similar to the lock laser setup, except that we lock the first order sideband to the atomic transition instead to the transfer cavity ($\omega_p + \omega_{sb} = \omega_a$). We choose the sideband frequency to be centered at 400 MHz ($\omega_{sb} = 400 + \delta\omega$), and shift up the frequency of the unmodulated beam of the probe laser by 400 MHz using a double pass AOM. Consequently, the frequency of the unmodulated beam that couples to the near-concentric cavity can be set as $\omega_p = \omega_a + \delta\omega$. Using this technique, we can obtain the detuning range of more than

200 MHz. Figure 6-4 shows the cavity reflection and transmission spectrum obtained by detuning the probe frequency. The good agreement between the measured cavity spectra and the fits to Lorentzian lineshapes suggests that the optical power of the probe beam is constant across the detuning range of 240 MHz.

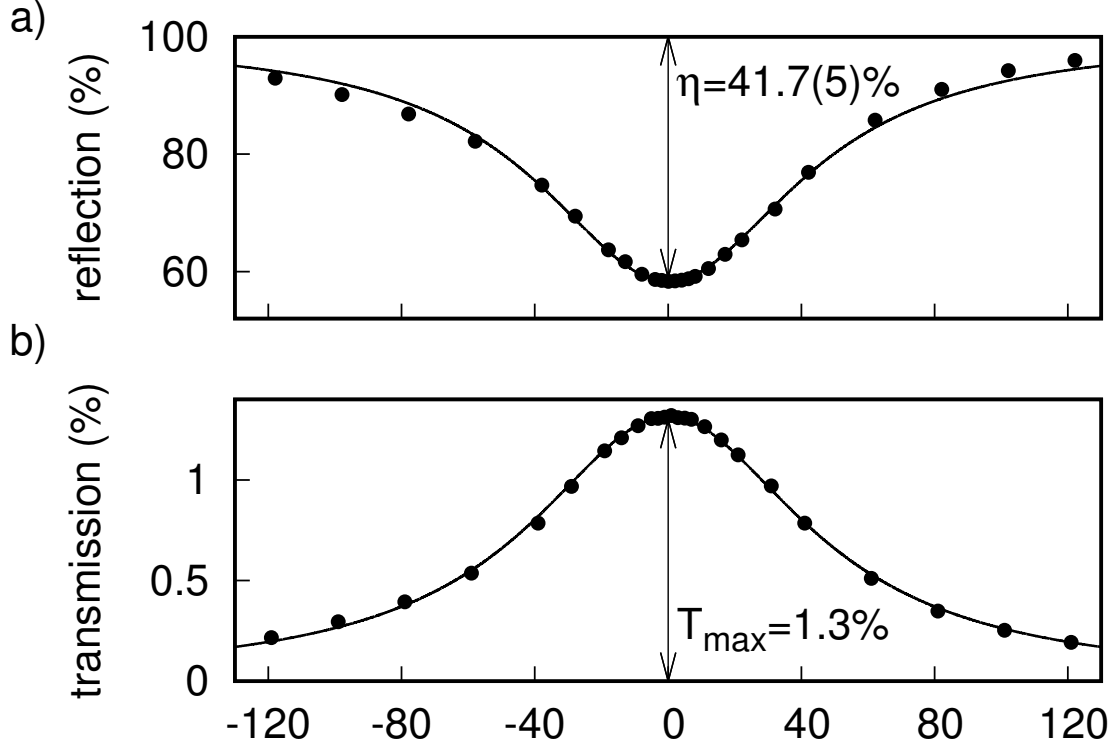


Figure 6-4: Normalized cavity reflection (a) and transmission (b) spectrum. The cavity length is stabilized while the probe beam frequency is detuned using the EOM sideband locking technique. Solid lines are fits based on Lorentzian lineshapes. η is the cavity coupling efficiency, and T_{\max} is the cavity resonant transmission.

6.3 Atom-light interaction setup

6.3.1 Optical setup

We operate the near-concentric cavity at the critical distance of $1.7 \mu\text{m}$ ($d = 2R_c - l_{\text{cav}} = 1.7 \mu\text{m}$). The cavity length is set to be resonant with the shifted atomic transition ($\Delta_{ca} = \omega_c - \omega_a = 0$). The probe beam is linearly polarized and coupled

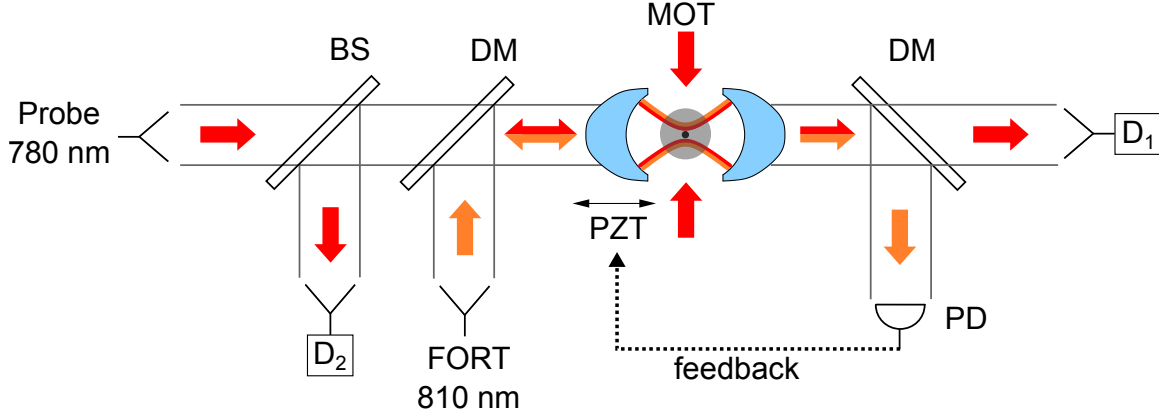


Figure 6-5: Optical setup. A near-resonant 780 nm probe laser couples to the cavity to characterize the light-atom interaction. The transmitted and reflected light is coupled into single-mode fibers connected to avalanche photodetectors. The cavity length is stabilized close to the concentric length. The intracavity field at 810 nm provides also a far-off-resonant standing-wave dipole trap for the atoms. BS: beam splitter with 70% reflectivity; DM: dichroic mirror; PZT: 3D-piezo actuator stack; PD: photodiode; MOT: magneto-optical trap; D1(2): avalanche photodetectors.

to a fundamental mode of the cavity. We detune the probe frequency to obtain the cavity reflection and transmission spectra (see Fig. 6-5). The probe laser power is set low so that the intra-cavity photon number is less than one. Hence, the excitation of the atom-cavity system can be limited to the first excitation manifold of $|n = 1, \pm\rangle$ (see Fig. 2-1).

The transmission and reflection of the probe field are coupled into single-mode fibers connected to avalanche photodetectors (APDs) with a detection efficiency of 48.7(1)% for D1 and 45.2(1)% for D2. The atomic fluorescence from the MOT cooling beams into the cavity mode is also collected into the same fibers and detected at these two APDs. The probe and trap lasers are combined at the input and separated at the cavity transmission by dichroic mirrors. Several interference filters at 780 nm are used to block 810 nm light from reaching the detectors.

6.3.2 Measurement sequence

As outlined in chapter 4, the near-concentric cavity is sensitive to the transverse misalignment which can lead to several undesired effects in a spectroscopy experiment, such as reduction of cavity transmission, excitation of transverse modes, and shifting

of positions of trapped atoms. To measure g_0 accurately, the cavity alignment and cavity length must be stabilized throughout the measurement of the atom-cavity spectrum.

Thus, preceding to the experimental stage of loading and probing single atoms, we introduce an automatic control scheme to stabilize the resonant transmission and the resonant frequency of the cavity. The scheme consists of two verification stages (see Fig. 6-6): one for the resonance lock and one for the transverse lock. Each verification stage measures a cavity parameter and compares it against a predefined threshold. Depending on the result of the comparison, compensation actions can take place to minimize the difference between the parameter and the threshold. There are three possible outcomes for each verification stage:

- **Pass:** The comparison output is True and no adjustment is required.
- **Adjust:** The comparison output is False. An algorithm is activated to adjust the cavity.
- **Fail:** The adjustment can fail for two reasons: (1) the updated comparison output remains to be False even after the adjustment, and (2) there is no improvement on the cavity parameter after a certain number of adjustment steps.

In the following, we describe each experimental stage shown in Fig. 6-6 with more details.

Transverse lock

In this stage, the transverse stabilization of the cavity is carried out (see Sec. 4.2). The stabilization algorithm triggers if the resonant cavity transmission is below the transmission of the optimally aligned cavity. To avoid the “infite looping” of the mirror’s position, we limit the number of adjustments steps to be around 50, which is 5 times of the average steps taken to optimize the transmission. The algorithm will stop if it exceeds the allowable number of steps. In addition, we set the frequency of the transverse lock stage high enough that the cavity transmission rarely drops below 90%.

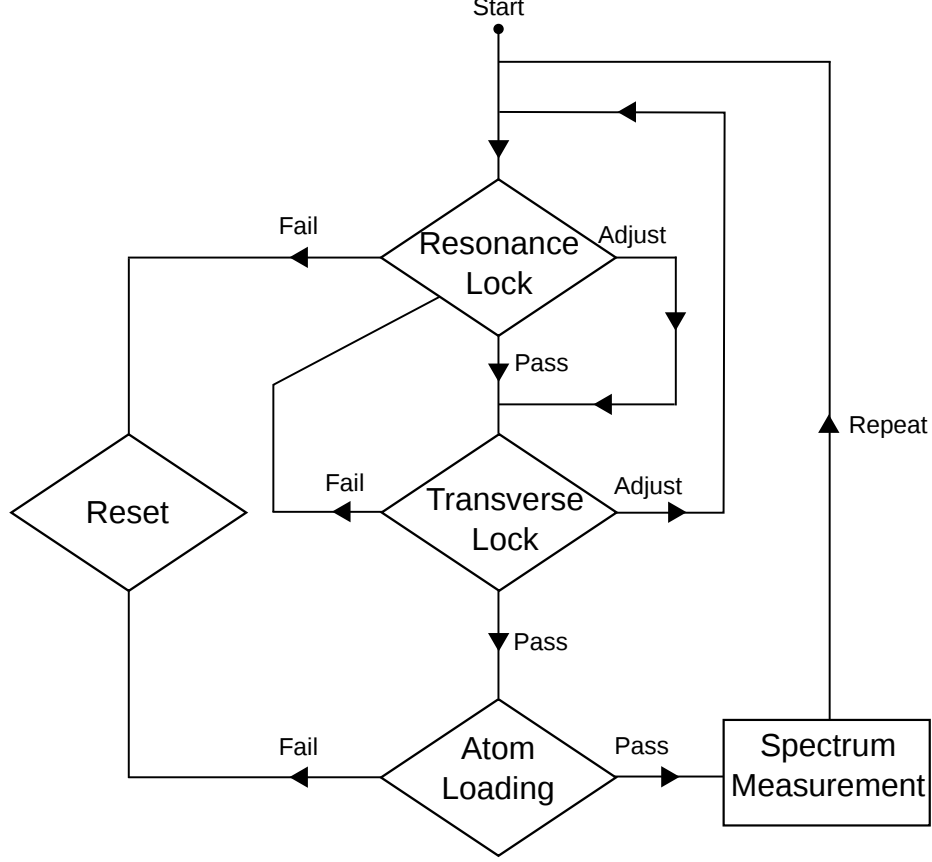


Figure 6-6: Experimental control scheme. The transverse alignment and resonance of the near-concentric cavity are verified at two stages: the resonance lock and the transverse lock. The main experiment proceeds only when both stages pass without adjustment.

Resonance lock

We observe that the resonant frequency of the near-concentric cavity slightly changes as we adjust the transverse position of the cavity mirror. We attribute this coupling between the radial and longitudinal movement of the cavity to the misalignment between the optical cavity axis and the z-axis of the piezo movement. We address this problem with an algorithm that detects an offset of the cavity resonance and corrects for that offset accordingly. First, the cavity spectrum is obtained by detuning the probe frequency. Next, we determine the cavity frequency ω_{c2} from a fit of the cavity spectrum to the Lorentzian function, and compare it against the atomic transition ω_a . If $\omega_{c2} = \omega_a$, the control scheme terminates the resonance lock and proceeds to the

next stage. Otherwise, the cavity frequency need to be shifted by $\Delta_c = \omega_{c2} - \omega_a$. As the cavity length is stabilized to the lock laser, the cavity frequency can be changed by adjusting the lock laser frequency. Therefore, to set the cavity back on resonance, the control scheme detunes the lock laser frequency by $-\Delta_c$ via the sideband's frequency (see section 4.1).

Atom loading and spectrum measurement

In these stages, we implement an experimental sequence that traps and probes single atoms (see section 6.3.3 for more details). The process of loading atoms and probing the cavity at one frequency detuning takes about 10 minutes for about 200 single-atom events; whereas a typical transverse drift of the near-concentric cavity is on the order of 30 minutes (see Fig. 4-7). This leads to a need to stabilize the cavity in the same amount of time. Therefore, we repeat the probing for three different probe frequency detuning before repeating the verification stages all over again.

Reset

In the event that any of the verification stages fails to proceed, the reset stage sets all experimental parameters to initial values. This setting is to prevent the control system from driving the piezo actuator to extreme positions.

6.3.3 Experimental sequence of trapping and probing

After the verification stages, the experiment enters the stage of loading and probing single atoms. The probing is implemented with a measurement sequence shown in Fig. 6-7. The photoevents detected at the APD D1 caused by the fluorescence of the atoms trigger the experimental sequence. Subsequently, the cooling beams and the magnetic field are switched off to disperse the MOT. This is followed by a sequence of alternating 1 ms pulses of probing and 1 ms pulses of laser cooling. The cooling pulses are employed to mitigate the heating of the atoms caused by the probing pulses. In addition, the detected photoevents during the cooling cycle are used to check presence of the atoms in the trap. The optical power of the dipole trap remains constant through out the experiment.

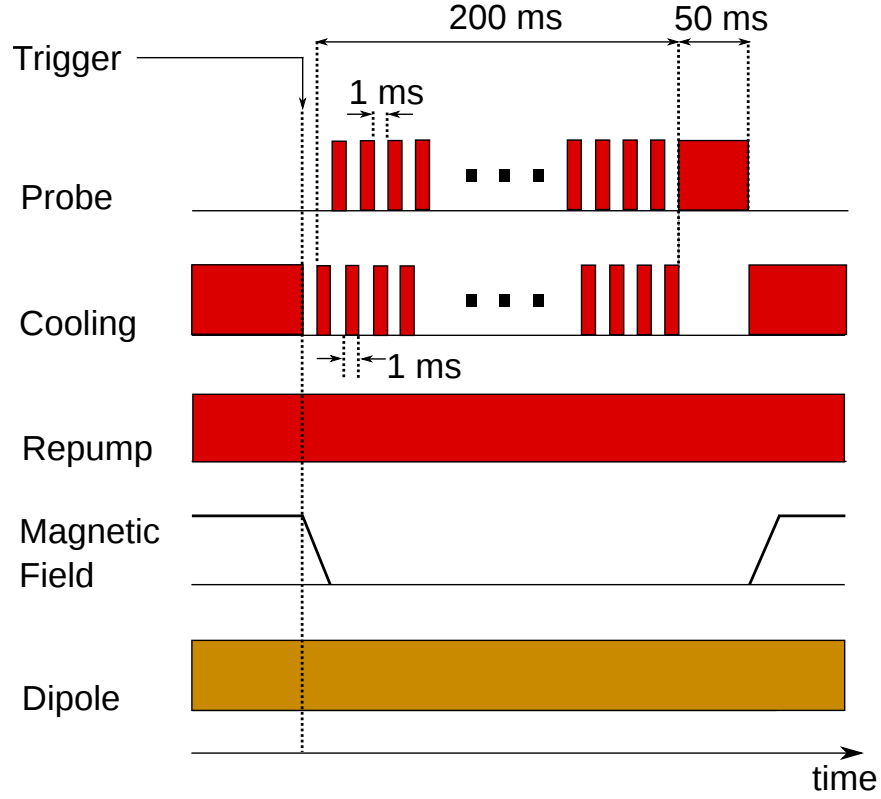


Figure 6-7: Timing sequence of trapping and probing single atoms. After the detection of single atoms, the quadrupole magnetic field and repumping beam are switched off to disperse the MOT. This is followed by an experimental cycle that alternates between 1 ms of probing the cavity transmission, and 1 ms of laser cooling. A probe pulse with 50 ms duration is used to measure the empty-cavity transmission and reflection.

6.4 Resonant probing

One of the most prominent effects of atom-light interaction is the extinction of resonant optical fields by a single atom [Gerhardt et al., 2007, Tey et al., 2008]. This effect can be observed in the atom-cavity system if the detunings are less than the normal-mode splitting ($\Delta_{c,(a)} \leq g_0$). In the context of cavity QED, the extinction ratio can be defined to be the ratio between the atom-cavity transmission and the resonant transmission of the empty cavity. Figure 6-8 shows detected photo-events at the APD D1 at resonance ($\Delta_{c,(a)} = 0$). An individual atom is loaded into the cavity mode and triggers the measurement sequence at $t = 0$. In the presence of the

trapped single atom, the fluorescence signal increases while the cavity transmission of the probe field reduces. At $t \approx 100$ ms, the atom escapes from the trap, and the signals simultaneously revert to the values of the empty cavity.

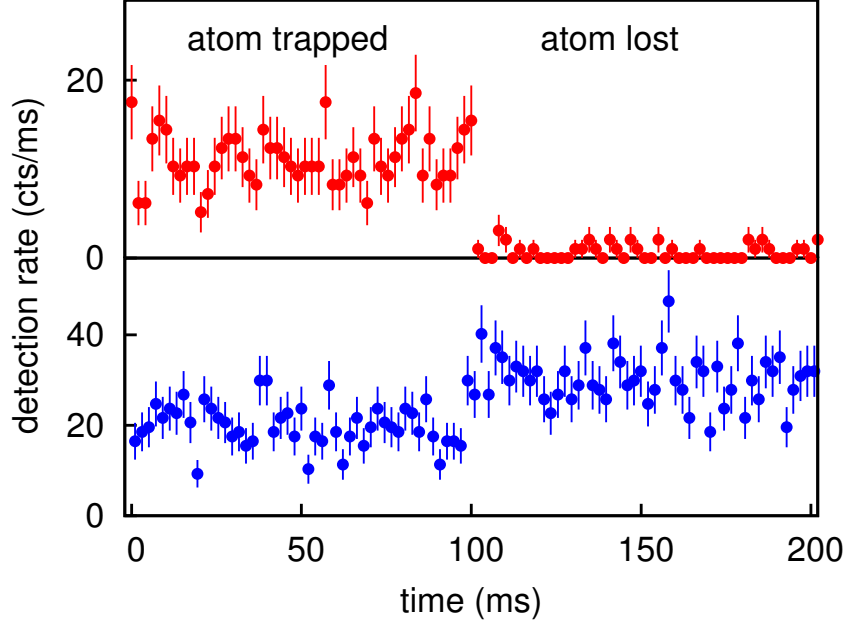


Figure 6-8: Effect of single atoms on cavity transmission. An experimental sequence with a duration of 200 ms consists of interleaving 1 ms pulses of cooling (red/upper) and probing (blue/bottom). Error bars represent one standard deviation determined from the measured count rates, assuming Poissonian counting statistics.

We obtain the measurement for the transmission from many loading events of which we post-selected those where a single atom is observed (see section 5.3 for the post-selection mechanism). We observe a maximum extinction ratio of 39%. We normalize the data to the steady-state cavity transmission after the atoms escape from the cavity mode. The average of cavity transmission can be modelled as

$$T_{avg} = 1 - T_0 \exp(-t/\tau_p), \quad (6.4.1)$$

where τ_p is the lifetime of atoms and T_0 denotes the reduction of the transmission immediately after the triggering. From a fit of the cavity transmission to Eq. 6.4.1, we determine τ_p to be 9.2(7) ms.

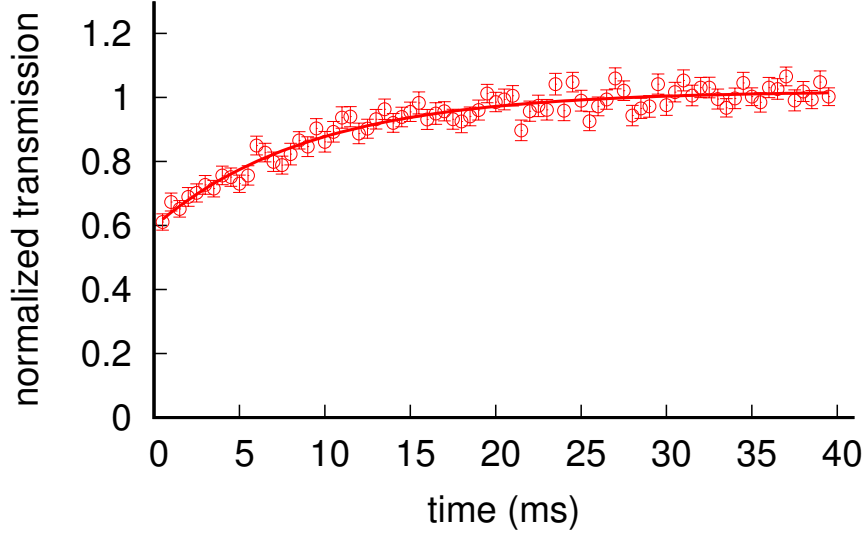


Figure 6-9: Average of the cavity transmission when single atoms are loaded into the cavity mode. The probe frequency is tuned to the atom-cavity resonance to observe the highest extinction of the transmission. The average of the resonant extinction ratio is determined to be 39% from a fit indicated by the solid line.

6.5 Normal mode splitting

The single atom-cavity coupling strength g_0 can be determined from the cavity transmission and reflection. Since our objective is to probe the linear response of the composite atom-cavity system, we restrict the intra-cavity intensity of the probe field to be much lesser than the critical photon number n_0 . In this condition, the atom is not saturated by the cavity field and hence the dynamical evolution is restricted to the excitation of the first manifold (see Eq. 2.2.6). For a weak coherent beam, the coefficients for intensity transmission $T(\omega)$ and reflection $R(\omega)$ are given by

$$T(\omega) = \left| \frac{\kappa_T (i\Delta_a + \gamma)}{(i\Delta_c + \kappa)(i\Delta_a + \gamma) + g_0^2} \right|^2, \quad (6.5.1a)$$

$$R(\omega) = \left| 1 - \frac{2\kappa_T (i\Delta_a + \gamma)}{(i\Delta_c + \kappa)(i\Delta_a + \gamma) + g_0^2} \right|^2, \quad (6.5.1b)$$

with a cavity field decay rate through each mirror $\kappa_T = T\pi c/l_{\text{cav}}$ [Reiserer and Rempe, 2015].

The atom-light interaction is revealed in the reflection and transmission spectrum

obtained by tuning the frequency of the probe laser. When an atom is present, the spectra show the onset of the normal-mode splitting (Fig. 6-10, red circles). For each probe detuning, approximately 250 single-atom events are collected. From a fit of the transmission spectrum to Eq. 6.5.1a, we obtain an interaction strength $g_0 = 2\pi \times 5.0(2)$ MHz, and a frequency offset $\omega_{\text{off}} = \omega_c - \omega_a = 2\pi \times 3.4(3)$ MHz between cavity and atomic resonance. We attribute this frequency offset, which is equal to 3.4% of the cavity linewidth, to the drifting of the lock laser frequency. The amplitude of the fit function $T(\omega)$ is set to the independently determined maximum transmission of the empty cavity. From g_0 , the cavity linewidth $2\kappa = 2\pi \times 99(1)$ MHz, and the natural transition linewidth $2\gamma = 2\pi \times 6.07$ MHz, we obtain the single atom cooperativity $C_0 = g_0^2/(2\kappa\gamma) = 0.084(4)$.

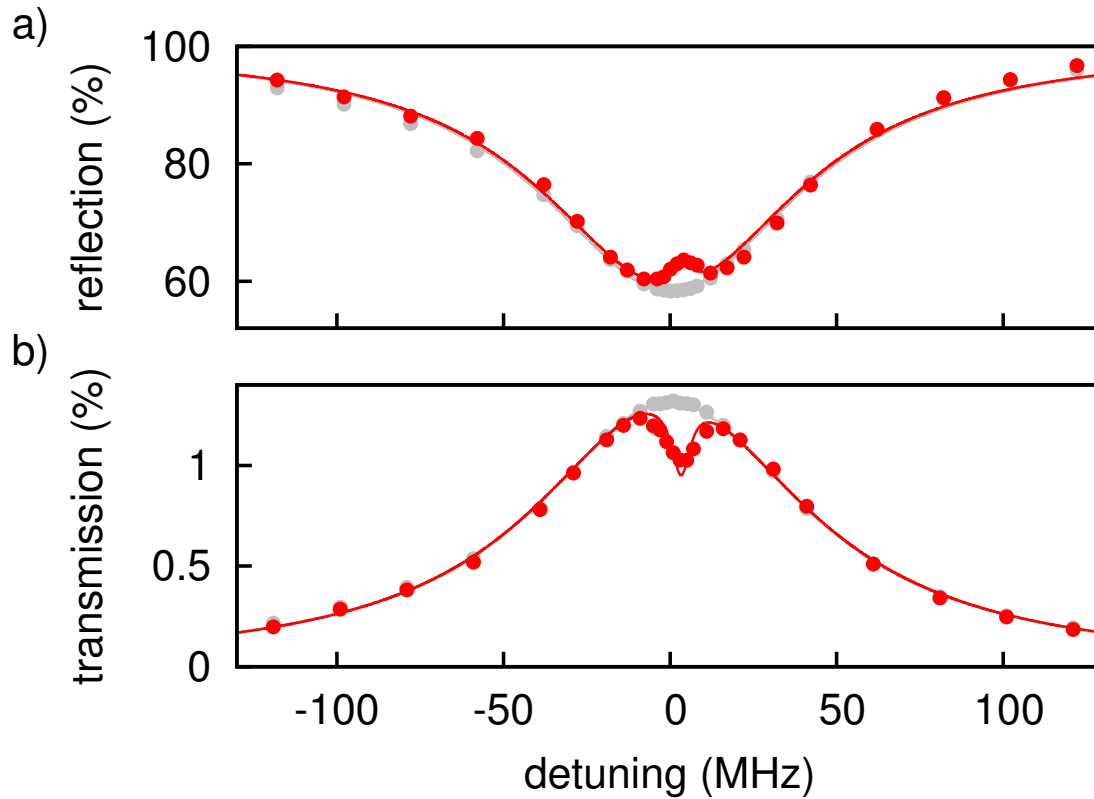


Figure 6-10: Onset of the normal-mode splitting in the a) reflection and b) transmission spectrum when an atom is trapped in the FORT. Red solid lines are fits based on Eq. 6.5.1a. For comparison the empty cavity reflection/transmission is shown in gray.

The reflection spectrum is analyzed in a similar way by fitting to Eq. 6.5.1b. For

this, we obtain $g_0 = 2\pi \times 4.6(4)$ MHz, the frequency offset $\omega_{\text{off}} = 2\pi \times 4.4(7)$ MHz, and the reflected power far away from the atom/cavity resonance. The fits of Eq. 6.5.1a-6.5.1b to the transmission and reflection reproduce the observed values well (Fig. 6-10, solid lines), and lead to similar values for the atom-cavity coupling constant g_0 and the frequency offset ω_{off} .

The experimentally obtained value for g_0 is lower than expected for a clean two-level atom from the cavity geometry $g_0 = \sqrt{3\lambda^2 c \gamma / (4\pi V)} = 2\pi \times 12.1$ MHz. We attribute this partly to the fact that in this experiment, the atom is prepared by the MOT beams in a random spin state m_F of the $5S_{1/2}$, $F=2$ manifold before the transmission is probed with a linearly polarized probe field. Averaging over the corresponding Clebsch-Gordan coefficients, we estimate that the atom-cavity coupling should be a factor $\sqrt{2}$ larger for a circularly polarized probe field driving an atom prepared in the $5S_{1/2}$, $F=2$, $m_F=2$ on a transition to the $5P_{3/2}$, $F=3$, $m_F=3$ state.

Another factor that may affect the coupling strength is the location of the single atoms in the cavity mode. The single atoms are loaded to random antinodes of the standing-wave dipole trap. At these different loading sites, the atoms have different interaction strength with the resonant cavity mode (see Fig. 6-11). This aspect can be taken into account by including a position-dependent factor to coupling strength $g(\vec{r}) \equiv g_0 |\psi(\vec{r})|$, where $\psi(\vec{r}) = \sin kz \exp[-(x^2 + y^2)/w_0^2]$ is the cavity-mode function. Hence, averaging over many loading events results in an effective coupling strength of $\bar{g} = g_0 \sum \psi(\vec{r}_i) / N \leq g_0$, where N is the number of loading events.

To assess the theoretical dependence of \bar{g} on the atomic positions, we perform a Monte-Carlo simulation that assigns the atoms to random trapping sites. To simplify the model, we treat the atoms as point-like particles. In addition, we restrict the potential loading site to be inside a range of $2z_R$ about the cavity center. Outside of the Rayleigh range, the dipole trap intensity reduces by more than four times; trap depth is consequently less than 300 μ K. Therefore, the probability of loading atoms outside of the the Rayleigh range is minimal and can be excluded from our model. The antinodes of trap and probe cavity modes are assumed to be coincident at the cavity center. A simulation of $N = 2000$ trials shows that the majority of the atoms strongly couple to the cavity (see Fig. 6-12). This can be intuitively explained based on the observation that the cavity-mode function along the cavity axis varies little

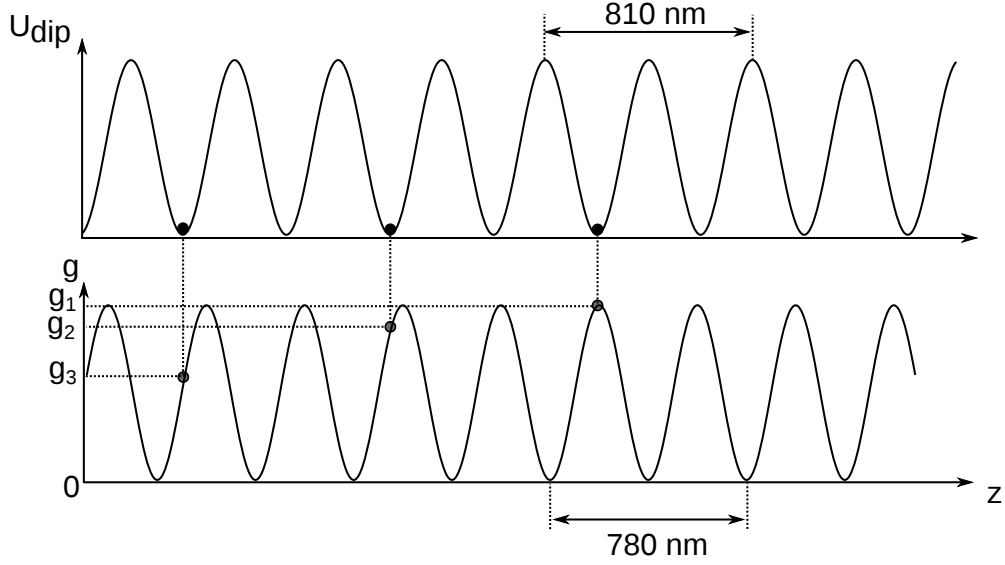


Figure 6-11: Demonstration of variation of the atom-cavity coupling strength. Single atoms are loaded into the bottom of the intracavity dipole trap formed by a 810-nm standing wave (Top). At the bottom is the corresponding atomic positions in the lattice of the resonant cavity mode at 780 nm.

around its maximum. An analogy is observed in the probability distribution of classical harmonic oscillator; this system spends more time near its classical turning points, where it moves more slowly. We run the simulation with 200 sets with each set contains $N = 200$ loading events. We find the average of the simulated coupling strength to be $\bar{g} = 0.64g_0 = 2\pi \times 5.4 \text{ MHz}$, which is in good agreement with the experimentally determined $g_0 = 2\pi \times 5.0 \text{ MHz}$.

To experimentally verify this hypothesis in our experiment, we turn to the analysis of the fluorescence of the atoms. The fluorescence of the atoms collected by the cavity depends on the atom positions and hence atom-cavity coupling strength [Kuhn et al., 2002]; the faster the atoms scatter the cooling light into the cavity the stronger their coupling to the cavity is. In support of this assertion, we post-selected the atoms into three types based on their detected fluorescence P_{fl} in an unit of counts/ms: $P_{\text{fl1}} \geq 20$, $17 \leq P_{\text{fl2}} \leq 20$, and $13 \leq P_{\text{fl3}} \leq 17$. The post-selected transmission spectra are shown in Fig. 6-13. We determine the atom-cavity coupling strength of each type by fitting the spectra to Eq. 6.5.1a: $g_1 = 2\pi \times 5.6(2) \text{ MHz}$, $g_2 = 2\pi \times 5.2(2) \text{ MHz}$, and

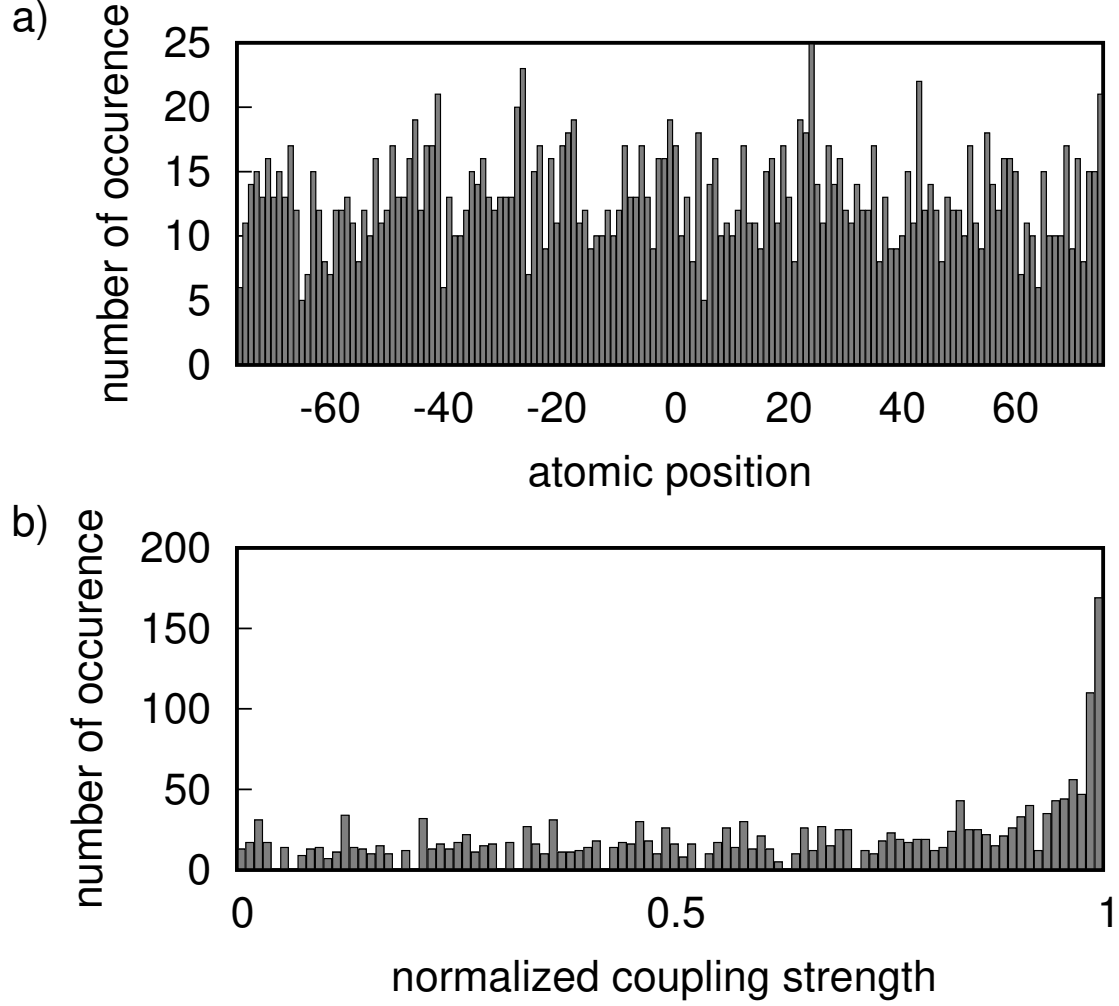


Figure 6-12: Simulation of variation of the atom-cavity coupling strength for $N=2000$ atom loading events. (a) Atoms are randomly assigned to different trapping sites. This results in the distribution of the normalized coupling strength \bar{g}/g_0 shown in (b).

$g_3 = 2\pi \times 4.9(2)$ MHz. The post-selected atoms of the band 1 show an increase in g_0 of 12%. However, it is still below the theoretical limit of $g_0 = 2\pi \times 8.5$ MHz for a linearly probe field driving an unpolarized atom. We attribute this discrepancy to other factors that potentially reduce the coupling strength such as the temperature of the atoms and the overlapping between the trap and the resonant cavity mode, which can be addressed in near future experiments.

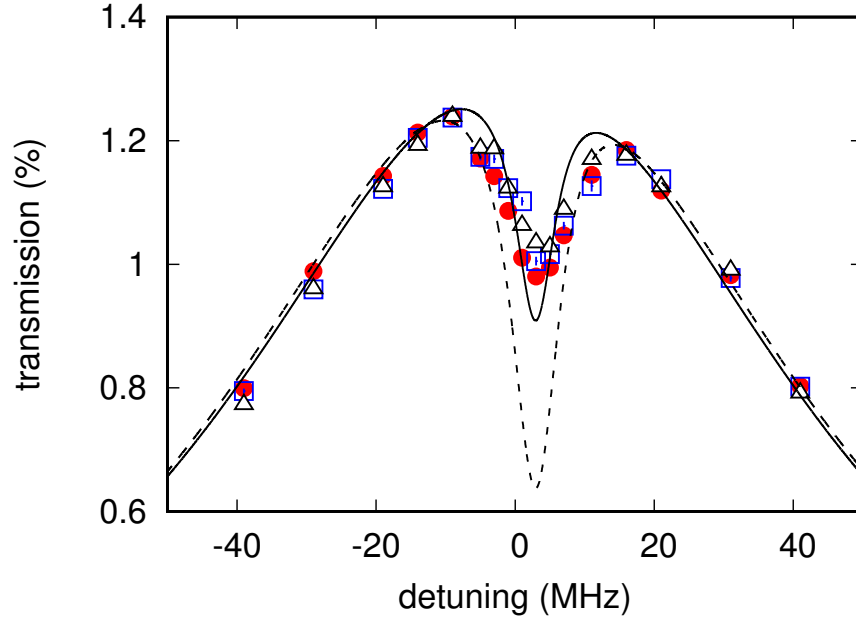


Figure 6-13: Cavity transmission spectra for three types of single-atoms indicated by red dots: $P_{\text{fl}} \geq 20$ counts/ms, blue squares: $17 \leq P_{\text{fl}} \leq 20$ counts/ms, black triangles: $13 \leq P_{\text{fl}} \leq 17$ counts/ms. The solid line is predicted spectrum for the effective coupling strength \bar{g} . The dash line is a theoretically predicted spectrum for the maximum coupling strength.

Chapter 7

Conclusion and outlook

7.1 Conclusion

High finesse cavities with sub-mm length provided a testbed to investigate atom-light interactions in a regime that classical models and perturbation theories are no longer valid. Apart from fundamental studies, simple quantum information tasks were demonstrated using these cavities as individual building blocks [Weber et al., 2009, Ritter et al., 2012, Reiserer, 2014]. The demonstrated systems have a typical size of one to few atoms interacting with one cavity mode. To fully harness the power of quantum technologies, the system size must be scaled up by either increasing the number of qubits per block or by connecting individual blocks into a coherent network [Kimble, 2008]. As a result, there is an ongoing research quest to explore other cavity designs which are easier to scale, or allow to integrate cavity QED with other physical platforms [Hunger et al., 2010, Nguyen et al., 2017, Cox et al., 2018]. This thesis contributes to this quest through the experimental demonstration of sizable atom-cavity coupling in near-concentric cavities. To conclude, let me briefly assess what has been achieved, what technical improvement can be made, and what research directions can be taken in the near future.

A great deal of effort of our research team was dedicated to developing techniques of stabilizing and positioning cavity mirrors in the near-concentric regime. As shown in chapter 3, we observe that the transverse positions of two cavity mirrors need to be aligned to an accuracy of less than 10 nm. This requirement of alignment makes

traditional methods of cavity construction and stabilization unsuitable. Through a combination of cavity mirror design and the technique of stabilizing the cavity in three dimensions, we demonstrate that the near-concentric cavity can be operated reliably at the last resonance length with a 780 nm laser, which corresponds to a stability parameter $g = -0.999962(2)$. Furthermore, the cavity linewidth ($\delta\nu = 22$ MHz) and the coupling efficiency ($\eta = 38\%$) of the fundamental mode are similar to the design values.

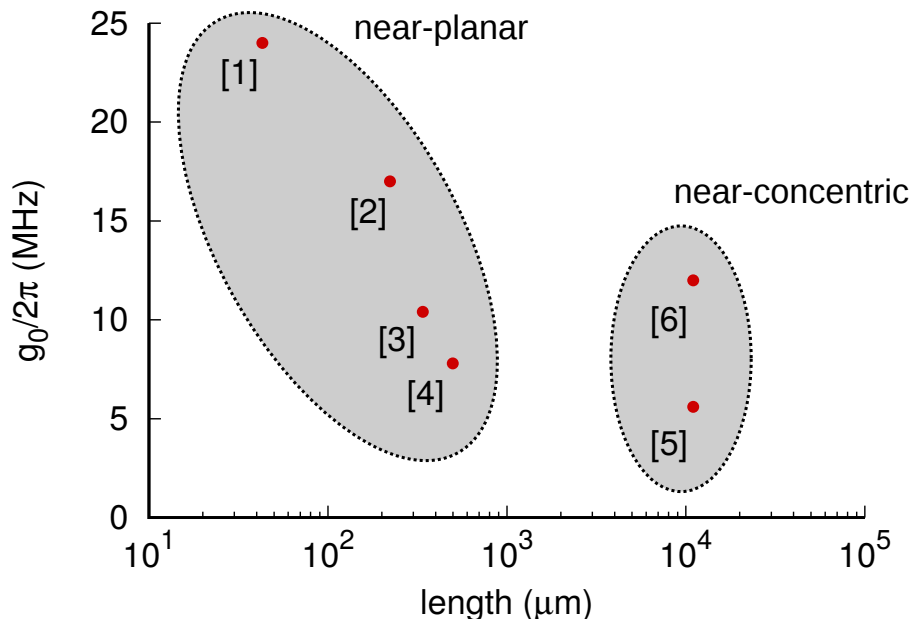


Figure 7-1: Atom-cavity coupling strength obtained in some existing experiments with Fabry-Perot optical resonators. The respective theoretical predictions for coupling strength in other experiments are represented by red dots; [1] Kimble’s group [McKeever et al., 2003], [2] Chapman’s group [Fortier et al., 2007], [3] Axel Kuhn’s group [Barrett et al., 2018], [4] Rempe’s group [Neuzner et al., 2016]. Coupling strength obtained in the near-concentric cavity presented in this thesis: [5] experimental observation, [6] theoretical prediction.

The second part of the thesis focuses on trapping single atoms in the cavity. To date, trapping single neutral atoms in the cavity has required a sophisticated optical setup to trap and deliver an atom to the cavity [Maunz et al., 2005, Fortier et al., 2007]. In our work, making use of a large spacing between the cavity mirrors, we can prepare a MOT cloud at the center of the cavity. By utilizing the lock laser as

an intra-cavity dipole trap, we observe the fluorescence of trapped single atoms in the cavity and determine the probability of loading single atoms from the MOT to the cavity to be 30%. Without any additional cooling methods, we observe a trap lifetime of 230 ms.

It may be surprising that any sizable atom-cavity coupling can be achieved with a cavity length of millimeters. In this thesis, the cavity has a length of 11 mm, and by operating the cavity in the near-concentric regime, we observe a doublet of the atom-cavity transmission spectrum, from which we determine a coupling strength $g_0 = 5.0(2)$ MHz. This coupling strength is comparable to what can be obtained with sub-mm length optical cavities (see Fig. 7-1). However, the unexpected contamination of the mirrors increased the cavity linewidth to 99(1) MHz over time. This reduced the single-atom cooperativity from an ideal value of 0.96 to a measured value of 0.084(4) for unpolarized atoms. Though the strong coupling regime has not been reached in this experiment, we expect that a single-atom cooperativity above unity can be reached by modestly increasing the finesse to $F = 1000$ and performing the probing on a cyclic transition.

7.2 Outlook

7.2.1 Rapid deterministic loading of single atoms

With the advances in laser-cooling techniques, there has been considerable progress in trapping individual atoms in the optical cavities. Starting with a MOT cloud, experiments in cavity QED often rely on a probabilistic process of loading single atoms into the cavity from either free-falling atoms or an atomic fountain. By reducing the atom loading rate, the mean number of atoms inside the cavity can be limited to less than one. However, Poissonian statistics of the loading process indicates that the probability of having more than one atom does not vanish. Deterministic loading of single atoms is necessary for some applications of cavity QED system such as single photon sources.

The single-atom conveyor belt is a method that transports a desired number of atoms into an optical cavity [Fortier et al., 2007]. In this technique, a few atoms trapped from a high-gradient MOT are transferred to and stored in an optical trap

outside the cavity. The number of the atoms is monitored based on atomic fluorescence. The atoms gradually evaporate until one atom remains in the trap, which triggers the process of delivering the single atom to the cavity. As the certainty in the number of atoms was ensured by adopting a strategy of “waiting” and monitoring, this may hinder the atom loading rate, which is necessary to employ the cavity QED for practical applications.

Near-concentric cavities permit another approach. By setting the cavity length closer to the critical length, the cavity beam waist can be reduced to a value that makes the collisional blockade possible for individual lattice sites [Schlosser et al., 2002]. In the collisional blockade regime, the number of trapped atoms is sub-Poissonian; either zero or only one atom is trapped. Together with heralding this one atom, the deterministic loading of single atoms in the cavity can be achieved. In addition, operating the MOT inside the cavity accelerates the loading process by eliminating the need to transport single atoms to the cavity.

7.2.2 Deep optical dipole traps

Deep optical traps allow precise localization of atoms and a long atom lifetime in the trap [Neuzner et al., 2015]. In the presence of heating processes induced by scattering photons, the atoms are evaporated out of the trap after $N \approx 2mU_0/p^2$ scattering events on average, where m is the atomic mass, U_0 is the trap depth, and p is the photon momentum. In experiments that employ intra-cavity dipole traps, laser-induced damaging and heating of the mirrors set a limit for the maximum trap depth. In near-concentric cavities, the quick divergence of the cavity mode leads to a large beam waist on the cavity mirrors. This reduces the laser intensity incident on the mirrors for a given intra-cavity optical power. In addition, small cavity beam waists of few micrometers can be employed to implement a microscopic intra-cavity dipole trap with high transverse confinement.

7.2.3 Single atoms coupled to multiple cavity modes

Most experiments in cavity QED so far have focused mainly on single mode cavities. On the theoretical side, inclusion of more than one cavity mode is predicted to lead

to stronger atom-light interactions and a few intriguing effects. Examples include an increase in the capture range of cavity cooling and an enhancement of resolution of atom-cavity microscopes [Hood et al., 2000, Vuletić et al., 2001]. Recently, cavity QED with more than one mode was realized with different polarization modes induced by birefringence of mirror coatings [Puppe et al., 2004]. In this case, the number of modes is inherently limited to two. Atom-cavity coupling with more than two modes has been demonstrated with an atomic ensemble in confocal cavities [Wickenbrock et al., 2013]. However, in the experiments with confocal cavities, the single-atom coupling strength is sub-MHz, and only transverse modes with the same parity are degenerate. On the other hand, near-concentric cavities with frequency-degenerate transverse modes can be employed to investigate the interaction of single atoms with several electromagnetic field modes in the strong coupling regime.

7.2.4 Ion traps in near-concentric cavities

The Nobel prize in physics in 2012 was shared by Serge Haroche and David J. Wineland for their development of cavity QED and trapped ions, respectively. The two new experimental platforms allow precise manipulation of individual quantum systems with different advantages. Trapped atomic ions have long coherence times, and their electronic states can be detected with almost 100% quantum efficiency, using quantum shelving methods. Entanglement of multiple ions in the same trap is achieved via coupling the internal states of ion and collective motional modes. On the other hand, cavity QED provides an efficient light-matter interface. To combine these two platforms for future applications such as quantum network nodes and quantum simulation with larger number of qubits, a single ion must be trapped inside the cavity and strongly coupled to a single cavity mode. Despite the potential applications, the strong coupling regime with ions has not been achieved yet. This is mainly because trapping an ion in an optical cavity is technically challenging. The dielectric mirror surfaces can accumulate charge and hence affect the trapping potential. In addition, excess space in the vicinity of the cavity is required to set up electrodes. Therefore, optical cavities with sub-mm lengths are not considered and other types of cavities must be explored for this application. Fiber cavities reduce the amount of dielectric material in the vicinity of the ions and offer small mode volumes to obtain the strong

coupling regime [[Steiner et al., 2013](#)]. Here, near-concentric cavities provide both strong coupling strength and large ion-dielectric separation, which is about 5.5 mm for the cavity presented in this thesis.

Bibliography

- [Allen et al., 1992] Allen, L., Beijersbergen, M. W., Spreeuw, R. J., and Woerdman, J. P. (1992). Orbital angular momentum of light and the transformation of Laguerre-Gaussian laser modes. *Physical Review A*, 45(11):8185–8189.
- [Barenco et al., 1995] Barenco, A., Bennett, C. H., Cleve, R., DiVincenzo, D. P., Margolus, N., Shor, P., Sleator, T., Smolin, J. A., and Weinfurter, H. (1995). Elementary gates for quantum computation. *Physical Review A*, 52(5):3457–3467.
- [Barrett et al., 2018] Barrett, T. D., Stuart, D., Barter, O., and Kuhn, A. (2018). Nonlinear Zeeman Effects in the Cavity-Enhanced Emission of Polarised Photons.
- [Baur et al., 2014] Baur, S., Tiarks, D., Rempe, G., and Dür, S. (2014). Single-Photon Switch Based on Rydberg Blockade. *Physical Review Letters*, 112(7):073901.
- [Birnbaum et al., 2005] Birnbaum, K. M., Boca, A., Miller, R., Boozer, A. D., Northup, T. E., and Kimble, H. J. (2005). Photon blockade in an optical cavity with one trapped atom. *Nature*, 436(7047):87–90.
- [Bjorklund, 1980] Bjorklund, G. C. (1980). Frequency-modulation spectroscopy: a new method for measuring weak absorptions and dispersions. *Optics Letters*, 5(1):15.
- [Black, 2001] Black, E. D. (2001). An introduction to PoundDreverHall laser frequency stabilization. *American Journal of Physics*, 69(1):79–87.
- [Blatt and Wineland, 2008] Blatt, R. and Wineland, D. (2008). Entangled states of trapped atomic ions. *Nature*, 453(7198):1008–1015.
- [Bloch, 2005] Bloch, I. (2005). Ultracold quantum gases in optical lattices. *Nature Physics*, 1(1):23–30.
- [Boca et al., 2004] Boca, A., Miller, R., Birnbaum, K. M., Boozer, A. D., McKeever, J., and Kimble, H. J. (2004). Observation of the vacuum Rabi spectrum for one trapped atom. *Physical Review Letters*, 93(23).

- [Boschi et al., 1998] Boschi, D., Branca, S., De Martini, F., Hardy, L., and Popescu, S. (1998). Experimental realization of teleporting an unknown pure quantum state via dual classical and einstein-podolsky-rosen channels. *Physical Review Letters*, 80(6):1121–1125.
- [Byer, 1997] Byer, R. L. (1997). Quasi-Phasematched Nonlinear Interactions and Devices. *Journal of Nonlinear Optical Physics & Materials*, 06(04):549–592.
- [Carmichael, 1998] Carmichael, H. P. (1998). *Statistical Methods in Quantum Optics: Master equations and Fokker-Planck equations*. Physics and Astronomy Online Library. Springer.
- [Chang et al., 2014] Chang, D. E., Vuletić, V., and Lukin, M. D. (2014). Quantum nonlinear optics - Photon by photon. *Nature Photonics*, 8(9):685–694.
- [Cirac et al., 1997] Cirac, J. I., Zoller, P., Kimble, H. J., and Mabuchi, H. (1997). Quantum State Transfer and Entanglement Distribution among Distant Nodes in a Quantum Network. *Physical Review Letters*, 78(16):3221–3224.
- [Cohen-tannoudji and Dupont-roc, 1997] Cohen-tannoudji, C. and Dupont-roc, J. (1997). *Photons and Atoms*.
- [Cox et al., 2018] Cox, K. C., Meyer, D. H., Schine, N. A., Fatemi, F. K., and Kunz, P. D. (2018). 30-Fold Increase in Atom-Cavity Coupling Using a Parabolic Ring Cavity.
- [Devoret and Schoelkopf, 2013] Devoret, M. H. and Schoelkopf, R. J. (2013). Superconducting circuits for quantum information: An outlook. *Science*, 339(6124):1169–1174.
- [Drever et al., 1983] Drever, R. W. P., Hall, J. L., Kowalski, F. V., Hough, J., Ford, G. M., Munley, A. J., and Ward, H. (1983). Laser phase and frequency stabilization using an optical resonator. *Applied Physics B Photophysics and Laser Chemistry*, 31(2):97–105.
- [Durak et al., 2014] Durak, K., Nguyen, C. H., Leong, V., Straupe, S., and Kurtsiefer, C. (2014). Diffraction-limited Fabry-Perot cavity in the near concentric regime. *New Journal of Physics*, 16(10):103002.
- [Ekert, 1991] Ekert, A. K. (1991). Quantum cryptography based on Bell’s theorem. *Physical Review Letters*, 67(6):661–663.
- [Fleischhauer et al., 2005] Fleischhauer, M., Imamoglu, A., and Marangos, J. P. (2005). Electromagnetically induced transparency: Optics in coherent media. *Reviews of Modern Physics*, 77(2):633–673.

- [Fortier et al., 2007] Fortier, K. M., Kim, S. Y., Gibbons, M. J., Ahmadi, P., and Chapman, M. S. (2007). Deterministic loading of individual atoms to a high-finesse optical cavity. *Physical Review Letters*, 98(23).
- [Gattobigio et al., 2010] Gattobigio, G. L., Pohl, T., Labeyrie, G., and Kaiser, R. (2010). Scaling laws for large magneto-optical traps. *Physica Scripta*, 81(2):025301.
- [Gerhardt et al., 2007] Gerhardt, I., Wrigge, G., Bushev, P., Zumofen, G., Agio, M., Pfab, R., and Sandoghdar, V. (2007). Strong Extinction of a Laser Beam by a Single Molecule. *Physical Review Letters*, 98(3):033601.
- [Goy et al., 1983] Goy, P., Raimond, J. M., Gross, M., and Haroche, S. (1983). Observation of cavity-enhanced single-atom spontaneous emission. *Physical Review Letters*, 50(24):1903–1906.
- [Grimm et al., 2000] Grimm, R., Weidemüller, M., and Ovchinnikov, Y. B. (2000). Optical Dipole Traps for Neutral Atoms. *Advances in Atomic, Molecular and Optical Physics*, 42(C):95–170.
- [Haase et al., 2006] Haase, A., Hessmo, B., and Schmiedmayer, J. (2006). Detecting magnetically guided atoms with an optical cavity. *Optics Letters*, 31(2):268.
- [Hanson et al., 2008] Hanson, R., Dobrovitski, V. V., Feiguin, A. E., Gywat, O., and Awschalom, D. D. (2008). Coherent dynamics of a single spin interacting with an adjustable spin bath. *Science*, 320(5874):352–355.
- [Harlander et al., 2010] Harlander, M., Brownnutt, M., Hänsel, W., and Blatt, R. (2010). Trapped-ion probing of light-induced charging effects on dielectrics. *New Journal of Physics*, 12(9):093035.
- [Hauck et al., 1980] Hauck, R., Kortz, H. P., and Weber, H. (1980). Misalignment sensitivity of optical resonators. *Applied Optics*, 19(4):598.
- [Heinzen et al., 1987] Heinzen, D. J., Childs, J. J., Thomas, J. E., and Feld, M. S. (1987). Enhanced and inhibited visible spontaneous emission by atoms in a confocal resonator. *Physical Review Letters*, 58(13):1320–1323.
- [Hood et al., 2001] Hood, C. J., Kimble, H. J., and Ye, J. (2001). Characterization of high-finesse mirrors: Loss, phase shifts, and mode structure in an optical cavity. *Physical Review A - Atomic, Molecular, and Optical Physics*, 64(3):7.
- [Hood et al., 2000] Hood, C. J., Lynn, T. W., Doherty, A. C., Parkins, A. S., and Kimble, H. J. (2000). The atom-cavity microscope: Single atoms bound in orbit by single photons. *Science*, 287(5457):1447–1453.

- [Hunger et al., 2010] Hunger, D., Steinmetz, T., Colombe, Y., Deutsch, C., Hänsch, T. W., and Reichel, J. (2010). A fiber Fabry-Perot cavity with high finesse. *New Journal of Physics*, 12(12).
- [Jaynes and Cummings, 1963] Jaynes, E. T. and Cummings, F. W. (1963). Comparison of Quantum and Semiclassical Radiation Theories with Application to the Beam Maser. *Proceedings of the IEEE*, 51(1):89–109.
- [Kimble, 1998] Kimble, H. J. (1998). Strong Interactions of Single Atoms and Photons in Cavity QED. In *Physica Scripta*, volume T76, page 127.
- [Kimble, 2008] Kimble, H. J. (2008). The quantum internet. *Nature*, 453(7198):1023–1030.
- [Kleppner, 1981] Kleppner, D. (1981). Inhibited spontaneous emission. *Physical Review Letters*, 47(4):233–236.
- [Kuhn et al., 2002] Kuhn, A., Hennrich, M., and Rempe, G. (2002). Deterministic Single-Photon Source for Distributed Quantum Networking. *Physical Review Letters*, 89(6).
- [Lett et al., 1989] Lett, P. D., Phillips, W. D., Rolston, S. L., Tanner, C. E., Watts, R. N., and Westbrook, C. I. (1989). Optical molasses. *Journal of the Optical Society of America B*, 6(11):2084.
- [Li et al., 2013] Li, L., Dudin, Y. O., and Kuzmich, A. (2013). Entanglement between light and an optical atomic excitation. *Nature*, 498(7455):466–469.
- [Lien et al., 2016] Lien, Y. H., Barontini, G., Scheucher, M., Mergenthaler, M., Goldwin, J., and Hinds, E. A. (2016). Observing coherence effects in an overdamped quantum system. *Nature Communications*, 7(May):1–7.
- [Lindquist et al., 1992] Lindquist, K., Stephens, M., and Wieman, C. (1992). Experimental and theoretical study of the vapor-cell Zeeman optical trap. *Physical Review A*, 46(7):4082–4090.
- [Lukin et al., 2001] Lukin, M. D., Fleischhauer, M., Cote, R., Duan, L. M., Jaksch, D., Cirac, J. I., and Zoller, P. (2001). Dipole blockade and quantum information processing in mesoscopic atomic ensembles. *Physical Review Letters*, 87(3):37901–1–37901–4.
- [Maunz et al., 2005] Maunz, P., Puppe, T., Schuster, I., Syassen, N., Pinkse, P. W., and Rempe, G. (2005). Normal-mode spectroscopy of a single-bound-atom-cavity system. *Physical Review Letters*, 94(3).

- [Maxwell et al., 2013] Maxwell, D., Szwer, D. J., Paredes-Barato, D., Busche, H., Pritchard, J. D., Gauguier, A., Weatherill, K. J., Jones, M. P. A., and Adams, C. S. (2013). Storage and control of optical photons using Rydberg polaritons. *Physical Review Letters*, 110(10).
- [McCarron et al., 2008] McCarron, D. J., King, S. A., and Cornish, S. L. (2008). Modulation transfer spectroscopy in atomic rubidium. *Measurement Science and Technology*, 19(10):105601.
- [McKeever et al., 2003] McKeever, J., Buck, J. R., Boozer, A. D., Kuzmich, A., Nägerl, H. C., Stamper-Kurn, D. M., and Kimble, H. J. (2003). State-Insensitive Cooling and Trapping of Single Atoms in an Optical Cavity. *Physical Review Letters*, 90(13):4.
- [Meschede, 2013] Meschede, D. (2013). Single atoms on demand for cavity QED experiments. *Thesis*.
- [Metcalf and van der Straten, 2007] Metcalf, H. C. and van der Straten, P. (2007). Laser Cooling and Trapping of Neutral Atoms. In *The Optics Encyclopedia*, volume 244, pages 975–1014. Wiley-VCH Verlag GmbH & Co. KGaA, Weinheim, Germany.
- [Morin et al., 1994] Morin, S. E., Yu, C. C., and Mossberg, T. W. (1994). Strong atom-cavity coupling over large volumes and the observation of subnatural intra-cavity atomic linewidths. *Physical Review Letters*, 73(11):1489–1492.
- [Neuzner et al., 2015] Neuzner, A., Körber, M., Dürr, S., Rempe, G., and Ritter, S. (2015). Breakdown of atomic hyperfine coupling in a deep optical-dipole trap. *Physical Review A - Atomic, Molecular, and Optical Physics*, 92(5):053842.
- [Neuzner et al., 2016] Neuzner, A., Körber, M., Morin, O., Ritter, S., and Rempe, G. (2016). Interference and dynamics of light from a distance-controlled atom pair in an optical cavity. *Nature Photonics*, 10(5):303–306.
- [Nguyen et al., 2017] Nguyen, C. H., Utama, A. N., Lewty, N., Durak, K., Maslennikov, G., Straupe, S., Steiner, M., and Kurtsiefer, C. (2017). Single atoms coupled to a near-concentric cavity. *Physical Review A*, 96(3):031802.
- [Nguyen et al., 2018] Nguyen, C. H., Utama, A. N., Lewty, N., and Kurtsiefer, C. (2018). Operating a near-concentric cavity at the last stable resonance.
- [Pound, 1947] Pound, R. V. (1947). Frequency stabilization of microwave oscillators. *Proceedings of the IRE*, 35(12):1405–1415.
- [Puppe et al., 2004] Puppe, T., Maunz, P., Fischer, T., Pinkse, P., and Rempe, G. (2004). Single-Atom Trajectories in Higher-Order Transverse Modes of a High-Finesse Optical Cavity. In *Physica Scripta*, volume T112, page 7.

- [Purcell et al., 1946] Purcell, E. M., Torrey, H. C., and Pound, R. V. (1946). Resonance absorption by nuclear magnetic moments in a solid [7]. *Physical Review*, 69(1-2):37–38.
- [Raab et al., 1987] Raab, E. L., Prentiss, M., Cable, A., Chu, S., and Pritchard, D. E. (1987). Trapping of Neutral Sodium Atoms with Radiation Pressure. *Physical Review Letters*, 59(23):2631–2634.
- [Raimond et al., 2001] Raimond, J. M., Brune, M., and Haroche, S. (2001). Colloquium: Manipulating quantum entanglement with atoms and photons in a cavity. *Reviews of Modern Physics*, 73(3):565–582.
- [Raizen et al., 1989] Raizen, M. G., Thompson, R. J., Brecha, R. J., Kimble, H. J., and Carmichael, H. J. (1989). Normal-mode splitting and linewidth averaging for two-state atoms in an optical cavity. *Physical Review Letters*, 63(3):240–243.
- [Reiserer, 2014] Reiserer, A. (2014). No Title. *A Controlled Phase Gate between A Single Atom and An Optical Photon*.
- [Reiserer and Rempe, 2015] Reiserer, A. and Rempe, G. (2015). Cavity-based quantum networks with single atoms and optical photons. *Reviews of Modern Physics*, 87(4):1379–1418.
- [Ritter et al., 2012] Ritter, S., Nölleke, C., Hahn, C., Reiserer, A., Neuzner, A., Uphoff, M., Mücke, M., Figueroa, E., Bochmann, J., and Rempe, G. (2012). An elementary quantum network of single atoms in optical cavities. *Nature*, 484(7393):195–200.
- [Rosenfeld, 2003] Rosenfeld, W. (2003). A high finesse optical resonator for cavity QED experiments. (August):62.
- [Saleh and Teich, 2001] Saleh, B. E. A. and Teich, M. C. (2001). *Resonator Optics*, pages 310–341. John Wiley & Sons, Inc.
- [Sangouard et al., 2011] Sangouard, N., Simon, C., De Riedmatten, H., and Gisin, N. (2011). Quantum repeaters based on atomic ensembles and linear optics. *Reviews of Modern Physics*, 83(1):33–80.
- [Schlosser et al., 2002] Schlosser, N., Reymond, G., and Grangier, P. (2002). Collisional Blockade in Microscopic Optical Dipole Traps. *Physical Review Letters*, 89(2):023005.
- [Schlosser et al., 2001] Schlosser, N., Reymond, G., Protsenko, I., and Grangier, P. (2001). Sub-poissonian loading of single atoms in a microscopic dipole trap. *Nature*, 411(6841):1024–1027.

- [Shor, 1995] Shor, P. W. (1995). Polynomial-Time Algorithms for Prime Factorization and Discrete Logarithms on a Quantum Computer. *SIAM Journal on Computing*, 26(5):1484–1509.
- [Siegman, 1986] Siegman, A. E. (1986). *Lasers*. University Science Books.
- [Steiner et al., 2013] Steiner, M., Meyer, H. M., Deutsch, C., Reichel, J., and Köhl, M. (2013). Single ion coupled to an optical fiber cavity. *Physical Review Letters*, 110(4).
- [Stute et al., 2012] Stute, A., Casabone, B., Schindler, P., Monz, T., Schmidt, P. O., Brandstätter, B., Northup, T. E., and Blatt, R. (2012). Tunable ionphoton entanglement in an optical cavity. *Nature*, 485(7399):482–485.
- [Tey et al., 2008] Tey, M. K., Chen, Z., Aljunid, S. A., Chng, B., Huber, F., Maslennikov, G., and Kurtsiefer, C. (2008). Strong interaction between light and a single trapped atom without the need for a cavity. *Nature Physics*, 4(12):924–927.
- [Thompson et al., 1992] Thompson, R. J., Rempe, G., and Kimble, H. J. (1992). Observation of normal-mode splitting for an atom in an optical cavity. *Physical Review Letters*, 68(8):1132–1135.
- [Torrallbo-Campo et al., 2015] Torralbo-Campo, L., Bruce, G. D., Smirne, G., and Cassettari, D. (2015). Light-induced atomic desorption in a compact system for ultracold atoms. *Scientific Reports*, 5:14729.
- [Vahala, 2003] Vahala, K. J. (2003). Optical microcavities. *Nature*, 424(6950):839–846.
- [Vandersypen and Chuang, 2004] Vandersypen, L. M. and Chuang, I. L. (2004). NMR techniques for quantum control and computation. *Reviews of Modern Physics*, 76(4):1037–1069.
- [Vuletić et al., 2001] Vuletić, V., Chan, H. W., and Black, A. T. (2001). Three-dimensional cavity Doppler cooling and cavity sideband cooling by coherent scattering. *Physical Review A. Atomic, Molecular, and Optical Physics*, 64(3):1–7.
- [Walther et al., 2006] Walther, H., Varcoe, B. T. H., Englert, B.-G., and Becker, T. (2006). Cavity quantum electrodynamics. *Reports on Progress in Physics*, 69(5):1325–1382.
- [Wang et al., 2018] Wang, H., Dovalé-Álvarez, M., Collins, C., Brown, D. D., Wang, M., Mow-Lowry, C. M., Han, S., and Freise, A. (2018). Feasibility of near-unstable cavities for future gravitational wave detectors. *Physical Review D*, 97(2):022001.
- [Warburton, 2013] Warburton, R. J. (2013). Single spins in self-assembled quantum dots. *Nature Materials*, 12(6):483–493.

- [Weber et al., 2009] Weber, B., Specht, H. P., Müller, T., Bochmann, J., Mücke, M., Moehring, D. L., and Rempe, G. (2009). Photon-photon entanglement with a single trapped atom. *Physical Review Letters*, 102(3).
- [Wickenbrock et al., 2013] Wickenbrock, A., Hemmerling, M., Robb, G. R. M., Emary, C., and Renzoni, F. (2013). Collective strong coupling in multimode cavity QED. *Physical Review A - Atomic, Molecular, and Optical Physics*, 87(4):43817.
- [Yariv, 2010] Yariv, A. (2010). *Optical Resonators*. Number 4. Springer-Verlag London.
- [Ye et al., 1999] Ye, J., Vernooy, D. W., and Kimble, H. J. (1999). Trapping of single atoms in cavity QED. *Physical Review Letters*, 83(24):4987–4990.